

University of Louisville

## ThinkIR: The University of Louisville's Institutional Repository

---

Electronic Theses and Dissertations

---

5-2013

### Near infrared photon-assisted polymerization of advanced polymer composites.

Peng Xu

*University of Louisville*

Follow this and additional works at: <https://ir.library.louisville.edu/etd>

---

#### Recommended Citation

Xu, Peng, "Near infrared photon-assisted polymerization of advanced polymer composites." (2013). *Electronic Theses and Dissertations*. Paper 1605. <https://doi.org/10.18297/etd/1605>

This Doctoral Dissertation is brought to you for free and open access by ThinkIR: The University of Louisville's Institutional Repository. It has been accepted for inclusion in Electronic Theses and Dissertations by an authorized administrator of ThinkIR: The University of Louisville's Institutional Repository. This title appears here courtesy of the author, who has retained all other copyrights. For more information, please contact [thinkir@louisville.edu](mailto:thinkir@louisville.edu).

**NEAR INFRARED PHOTON-ASSISTED POLYMERIZATION OF  
ADVANCED POLYMER COMPOSITES**

By

Peng Xu

B.S., Hefei University of Technology, China 2009

M.S., University of Louisville, USA 2011

A Thesis

Submitted to the Faculty of the  
J.B. Speed School of Engineering of the University of Louisville  
in Partial Fulfillment of the Requirements  
for the Degree of

Doctor of Philosophy

Department of Mechanical Engineering  
University of Louisville  
Louisville, Kentucky

May 2013

Copyright 2013 by Peng Xu

All rights reserved



**NEAR INFRARED PHOTON-ASSISTED POLYMERIZATION OF  
ADVANCED POLYMER COMPOSITES**

By

Peng Xu

B.S., Hefei University of Technology, China 2009

M.S., University of Louisville, USA 2011

A Thesis Approved On

April 10 2013

By the following Thesis Committee:

---

Dr. Balaji Panchapakesan (Thesis Director)

---

Dr. Roger D. Bradshaw

---

Dr. Stuart J. Williams

---

Dr. Gamini U. Sumanasekera

## **DEDICATION**

This thesis is dedicated to my parents

Mr. Qingguo Xu, Mrs. Lunying Lu

and my wife

Mrs. Yan Chen

You have been my greatest source of strength and inspiration.

## ACKNOWLEDGEMENTS

It is my honor to study in the department of mechanical engineering at University of Louisville. I am indebted to many people who have encouraged, supported and helped me with my research and life through these four years. Without their help, these works cannot be done. I would like to acknowledge my advisor Dr. Balaji Panchapakesan for giving me this opportunity to work in the field of nanotechnology and all his support. I would also like to thank Dr. Roger Bradshaw for his help and guidance in mechanical test. I also thank other committee members, Dr. Stuart Williams and Dr. Gamini Sumanasekera for their time and valuable suggestions in this work. Thank Dr. Jacek Jasinski for the help of X-ray photoelectron spectrum (XPS) measurement.

Some of this work was done at the University of Louisville's cleanroom facility and I thank the cleanroom managers and staffs: Julia Aebersold, Mark Crain, Donald Yeager, Curt Mckenna, Michael Martin, Joseph Williams and Joseph Lake. Thanks for their assistance, training and suggestions.

I thank the group members of the Small Systems Laboratory who worked with me before: James Loomis, Hanwen Yuan, Vanessa Velasco, Ben King, Farhad Khosravi, Tom Burkhead, Xiaoming Fan, and Joseph Duff.

Finally, I would like to thank my close friends Dr. Xiaoping Tang, Dr. Shengli Lu and their three years son Ethan Tang for their best friendship and support, and also thank them for proof reading of my dissertation.

Last but not least, I would like to thank my parents and wife for their love and support.

## ABSTRACT

### NEAR INFRARED PHOTON-ASSISTED POLYMERIZATION OF ADVANCED POLYMER COMPOSITES

Peng Xu

March 27, 2013

Advanced composites play important roles in the materials sciences, military, space and commercial applications. The desirable load transfer and mechanical strength of reinforced polymers are crucial for developing advanced composites. Owing to their excellent mechanical properties derived from the  $sp^2$  bonding structure and the nanoscale size, nano-carbons are attractive materials used for nanoscale reinforcement of polymer composites.

This dissertation describes a novel method to develop polymer composites using near infrared (NIR) photon-assisted polymerization and nanoscale reinforcement. We used multi-walled carbon nanotubes (MWNTs), reduced graphene oxide (RGO), and graphene nanoplatelets (GNPs) to make polymer composites, and explored *in-situ* NIR photon assisted heating of these nano carbons to enhance polymerization of the nano-carbon/polymer interface, thus achieving significant load transfer and improved

mechanical properties. To specify, nano-carbon was dispersed into the polymer matrix by shear or evaporation mixing method to attain a uniform distribution in the prepared thin film composite. The thin film was exposed to NIR light during polymerization instead of conventional oven based heating. NIR was effectively absorbed by nano-carbons and also atoms from polymer molecule; the induced photo-thermal heat was transferred into the polymer matrix to induce polymerization of the composite and the covalent bonding between nano-carbons and polymer matrix at the interface. Scanning electron microscope (SEM), Raman spectroscopy, and RSA were used to evaluate the load transfer and mechanical strength of the polymerized composite samples. Investigating first the nanotube/polymer composites synergized by NIR photon-assisted polymerization, large Raman shifts ( $20\text{ cm}^{-1}$  wavenumber for up to 80% strains) of the 2D band were recorded for the NIR light polymerized samples and an increase in Young's modulus by ~130% was measured for the 1 wt. MWNT/poly(dimethylsiloxane) (PDMS) composites. While at first it was thought that NIR radiation during polymerization heated the nano-carbons inside resulting in strengthening of the nano-carbon/polymer interface, it was seen after further experimentation with graphene reinforcements that other light induced bonding effects apart from heat were also responsible.

Raman spectroscopy revealed that mixing graphene in polymer has a profound effect on the G, D and 2D bands. Investigating G bands for pure RGO and GNPs and comparing them with their polymer counterparts showed large shifts in the G band indicating lattice compression. The comparison of the NIR polymerization with the conventional oven based polymerization for both RGO and GNPs revealed large changes in wavenumbers and indicated increased load transfers for the NIR photon-assisted

polymerization method. The Full Width Half Maximum (FWHM) data of the NIR treated samples exhibited smaller change at large strains compared to conventionally polymerized samples indicating the minimum slippage in the former. Finally, the stress-strain curves showed more than three times improvement in the Young's modulus of the composites fabricated using the NIR treatment in comparison to the conventional baking for both types of graphene. These results are compared to the carbon nanotube (CNT) counterparts in PDMS. The study provided insights on how to use stress-sensitive shifts in Raman spectroscopy for the development of advanced polymer composites.

While NIR light induced polymerization showed increased load transfer and mechanical strength of nanotube and graphene polymer composites, investigation into two types of nano-carbon of different dimensionalities yielded extraordinary synergy between nano-carbons. Synergistic effects in binary mixtures of nano-carbon/polymer composites polymerized by NIR photon-assisted polymerization are observed. Small amounts of MWNT<sub>0.1</sub> dispersed in RGO<sub>0.9</sub>/PDMS samples (subscripts represent weight percentage) reversed the sign of the Raman stress-sensitive wavenumbers from positive to negative values demonstrating the reversal of the lattice stress itself on applied uniaxial strain. A wavenumber change from 10 cm<sup>-1</sup> in compression to 10 cm<sup>-1</sup> in tension, and an increase in the Young's modulus of ~103% was observed for the MWNT<sub>0.1</sub>RGO<sub>0.9</sub>/PDMS with applied uniaxial tension. Extensive scanning electron microscopy measurement revealed the bridging of MWNT between two graphene plates in polymer composites. Mixing small amounts of MWNTs in RGO/PDMS eliminated the previously reported compressive deformation of RGO and significantly enhanced the load transfer and the mechanical strength of composites in tension. This is a direct

indication of the cooperative effects of binary nano-carbons that produces an overall dramatic increase in load transfer (100% change). The orientation order of MWNTs with the application of uniaxial tensile strain directly affected the shift in the Raman wavenumbers (2D-band and G-band) and the load transfer. It is observed that the cooperative behavior of binary nano-carbons in polymer composites resulted in enhanced load transfer and mechanical strength. Such binary compositions could be fundamentally interesting for developing advanced composites such as nano-carbon based mixed dimensional systems. The NIR polymerization could be used to control aspects such as polymer chain entanglement between nano-carbons of different dimensional states, polymer chain lengths, mobility and eventual mechanical and electrical properties.

At first it was thought that NIR light based polymerization only heated the nano-carbons and strengthened the interface, further studies using X-ray photoelectron spectroscopy (XPS) suggested other light induced bond formation was also responsible mechanism for improved interfacial strength, load transfer and mechanical properties. XPS data on RGO/polymer composites suggested activation of hydroxyl and carbonyl groups on the RGO that opens the carbon-carbon double bond of the PDMS oligomer thereby assisting in the formation of the C-O bonds between the PDMS matrix and the graphene filler. High absorption of NIR photons causes the free radical reaction between SiH group on PDMS crosslinker and hydroxyl/carbonyl groups on the RGO. The increase in the number of C-O and Si-O bonds at the graphene/polymer interface assists in the improved load transfer and eventual mechanical properties of the composites. This is the first such study which shows direct correlation between bond formation, load transfer and mechanical properties without degrading the interface. While surface chemical

functionalization is attractive, past reports have shown that improvement in interfacial adhesion due to surface functionalization of nanotubes does not always promote improvement in mechanical properties. This is due to the surface degradation of nanotubes/graphene during functionalization process. Compared to these techniques, the NIR light induced technique is benign, environmentally friendly and also results in high interfacial shear strength, load transfer and excellent mechanical properties.

As a demonstration of applications, PDMS/RGO/PDMS sandwiched structure strain sensor, a demo application of the NIR photon-assisted polymerization was investigated. High sensitivity and high Gauge Factor (GF) are addressed. These results shown in this dissertation suggest that the NIR photon-assisted polymerization can be practically developed as a scalable nanomanufacturing technique to create large panels of advanced composites with strong interface and better mechanical properties compared to conventional oven based heating methods. It also suggests that it is possible to fabricate large-scale flexible smart device like high sensitivity strain sensors.

## TABLE OF CONTENTS

DEDICATION .....	iii
ACKNOWLEDGEMENTS .....	iv
ABSTRACT .....	vi
CHAPTER 1 INTRODUCTION .....	1
CHAPTER 2 BACKGROUND REVIEW .....	9
2.1 Nano-carbon materials .....	9
2.1.1 Structure of nano-carbon materials.....	9
2.1.1.1 Carbon nanotubes .....	9
2.1.1.2 Graphene.....	13
2.1.1.3 Reduced graphene oxide (RGO).....	15
2.1.1.4 Graphene nanoplatelet (GNP) .....	18
2.1.2 Properties of nano-carbon materials .....	20
2.1.2.1 Carbon nanotube.....	20
2.1.2.2 Graphene.....	22
2.1.2.3 Reduced graphene oxide.....	23

2.1.2.4 Graphene nanoplatelet .....	24
2.2 Polymer .....	25
2.3 The synthesize methods of nano-carbon/polymer composites.....	29
2.3.1 The solution-based method.....	29
2.3.2 The melt compounding method.....	30
2.3.3 The in-situ polymerization method.....	31
2.3.4 The chemical functionalization method .....	32
2.4 The polymer composites based on carbon nanotubes and graphene.....	34
2.4.1 Nanotube/polymer composites .....	34
2.4.2 Graphene/polymer composites .....	36
2.5 Methods of characterization nano-carbon/polymer composites.....	37
2.5.1 Introduction to Raman Spectroscopy .....	38
2.5.2 Introduction to X-ray Photoelectron Spectroscopy .....	46
2.6 Stress sensitivity of polymer nanocomposites using Raman spectroscopy.....	48
 CHAPTER 3 NIR PHOTON-ASSISTED POLYMERIZATION OF CARBON NANOTUBE/POLYMER COMPOSITES .....	  52
3.1 Introduction .....	52
3.2 Results and discussions .....	53
3.2.1 Characterization of MWNT/PDMS composites.....	54
3.2.2 Raman-strain sensitivity study of MWNT/PDMS composites.....	55

3.2.3 Mechanical properties of MWNT/PDMS composites.....	58
3.3 Conclusion.....	60
CHAPTER 4 NIR PHOTON-ASSISTED POLYMERIZATION OF GRAPHENE/POLYMER COMPOSITES.....	63
4.1 Introduction.....	63
4.2 Results and discussion:.....	69
4.2.1 Characterization of graphene and graphene/PDMS composites .....	70
4.2.2 Raman-strain sensitivity of graphene/PDMS composites .....	76
4.2.3 Mechanical properties of graphene/PDMS composites.....	81
4.3 Conclusion.....	85
CHAPTER 5 SYNERGY EFFECT OF BINARY (1D MWNT, 2D RGO) NANO- CARBONS/POLYMER COMPOSITES.....	87
5.1 Introduction.....	87
5.1.1 Synergy in binary nano-carbons in polymer composites.....	88
5.1.2 Raman spectroscopy of binary nano-carbons in polymer composites .....	89
5.2 Results and Discussion.....	91
5.2.1 Characterization of binary mixture nano-carbons/PDMS composites .....	92
5.2.2 Raman-strain sensitivity of MWNT/PDMS and RGO/PDMS composites .....	96
5.2.3 Synergy effect of binary mixture nano-carbon/PDMS composites.....	99
5.2.4 Orientational ordering: A 2D model.....	103

5.2.5 Mechanical properties of binary nano-carbon/PDMS composites .....	108
5.2.6 Halpin-Tsai model for predicting Young's modulus of composites .....	109
5.2.7 Photomechanical responses of binary mixture nano-carbons/PDMS composites .....	113
5.3 Conclusion.....	117
<b>CHAPTER 6 THE MECHANISM OF NEAR INFRARED PHOTON-ASSISTED POLYMERIZATION.....</b>	
6.1 Introduction .....	119
6.2 Results and discussions .....	120
6.2.1 XPS characterization of nano-carbons (1D MWNT, 2D RGO, 3D GNP).....	122
6.2.2 Mechanism of synthesizing MWNT/PDMS by NIR photon-assisted method .....	124
6.2.3 Mechanism of synthesizing graphene/PDMS by NIR photon-assisted method .....	127
6.2.4 Mechanism of NIR light induced polymerization of nano-carbon/polymer composites .....	130
6.3 Conclusion.....	131
<b>CHAPTER 7 FLEXIBLE SANDWICHED-STRUCTURE STRAIN SENSOR FABRICATED BY NEAR INFRARED PHOTON-ASSISTED POLYMERIZATION.....</b>	
7.1 Introduction .....	133

7.2 Experimental section .....	136
7.2.1 The fabrication process of the strain sensor .....	136
7.2.2 The experimental setup for the strain-resistance relationship of the sandwiched- structure strain sensor .....	139
7.3 Results and discussion.....	140
7.4 Conclusion.....	147
CHAPTER 8 CONCLUSIONS AND FUTURE RESEARCH .....	149
8.1 Conclusions .....	149
8.2 Future research .....	153
REFERENCES .....	155
APPENDICES .....	171
CURRICULUM VITAE.....	179

## LIST OF TABLES

Table 4.1 Raman wavenumbers of D, G and 2D bands and their FWHM .....	75
Table 4.2 Young's modulus and Young's modulus change of different graphene/PDMS composites with different polymerization methods .....	84
Table 5.1 Synergistic effects in Young's modulus of MWNT <sub>x</sub> RGO <sub>1-x</sub> /PDMS composites .....	108
Table 6.1 The fitted ratio and the binding energy of all the carbon bonding groups in the MWNT, RGO and GNP fillers.....	123
Table 6.2 The ratios between the two different oxygen bonds, the ratios between the two different carbon bonds, and the ratios between different silicon bonds atoms are listed for MWNT/PDMS composites prepared by oven baking and by NIR heating. ....	127
Table 6.3 The ratios between the two different oxygen bonds, the ratios between the two different carbon bonds, and the ratios between different silicon bonds atoms are listed for RGO/PDMS, and GNP/PDMS composites prepared by oven baking and by NIR heating.....	129
Table 7.1 Comparison with different types strain sensors .....	134

## LIST OF FIGURES

Figure 2.1 The TEM image of carbon nanotubes [63]. Scale bar: 20 nm.....	10
Figure 2.2 A geometrical view of the relationship between carbon nanotube and graphene [68].....	11
Figure 2.3 The three types of Single-wall Carbon nanotubes: (a)armchair; (b)zigzag; (c) chiral [48].....	12
Figure 2.4 Mother of all graphitic forms. Graphene is a 2D building material of all other dimensionalities. It can be wrapped up into 0D fullerene, 1D carbon nanotube, and 3D graphite [58] .....	13
Figure 2.5 The SEM images of single layer RGO [79]. .....	16
Figure 2.6 The TEM image of a single layer RGO membrane. (a) Original image and (b) with color added to highlight the different features. The defect free crystalline graphene area is displayed in the original light gray color. Contaminated regions are shaded in dark gray. Blue regions are the disordered single-layer carbon networks, or extended topological defects, that we identify as remnants of the oxidation-reduction process. Red areas highlight individual ad-atoms or substitutions. Green areas indicate isolated topological defects, that is, single bond rotations or dislocation cores. Holes and their edge reconstructions are colored in yellow. Scale bar 1 nm. [80] .....	17
Figure 2.7 The SEM images of graphene nanoplatelet [79]. .....	19

Figure 2.8 The crystal structure of (a) Bernal stacked and (b) Rhombohedra stacked few layer graphene with the complete set of tight binding parameters [81].	20
Figure 2.9 The Stress-strain behavior of various polymers [108]	26
Figure 2.10 Schematics of PDMS polymerization based on oligomers and crosslinker [111].	28
Figure 2.11 The Raman spectra of PDMS. The peaks labeled 1-9 are the different vibrational peaks of Si-O-Si and CH <sub>3</sub> groups.	29
Figure 2.12 The schematic of a Raman spectrometer	38
Figure 2.13 The energy levels of a diatomic molecule	39
Figure 2.14 The transverse phonons in a 1D solid [150].	42
Figure 2.15 The calculated phonon dispersion relation of graphene showing the iLO, iTO, oTO, iLA and oTA phonon branches [151].	42
Figure 2.16 (a) The shadowed area is a real-space unit cell of graphene showing the inequivalent atoms A and B and unit the vectors $a_1$ and $a_2$ ; (b) the shadowed area is a reciprocal-space unit cell showing the 1 <sup>st</sup> Brillouin zone [151].	43
Figure 2.17 (a) First order G band; (b) one phonon second order D band; (c) two phonon second order G' band [151]	44
Figure 2.18 A schematic process image of the X-ray photoelectron spectroscopy	46
Figure 2.19 The schematic diagram of the photoelectric process (purple) and the Auger process (yellow).	47
Figure 2.20 A comparison of the “realistic” and the harmonic bond potentials [150]	50
Figure 3.1 Schematic of the two different polymerization techniques: (a) oven based heating; (b) NIR light treatment.	54

Figure 3.2 SEM images of the MWNT/PDMS samples, scale bar 500 nm; (a) 0.01 wt. %; (b) 0.1 wt. %; (c) 1 wt. % of MWNT.....	54
Figure 3.3 Raman spectra of the pure PDMS and the 1 wt. % MWNT/PDMS sample. ..	55
Figure 3.4 Load transfer in the conventional (a-1) and NIR light polymerized samples (b-1); the change in the wavenumber is displayed as a function of the percentage strain for the conventional (a-2) and NIR light polymerized samples (b-2)...	56
Figure 3.5 (a) Young's modulus versus NIR light dose for MWNT/PDMS fractions; (b) change in Young's modulus versus weight percentage of MWNT for light treated and oven baked methods. ....	58
Figure 4.1 Schematic of the two different polymerization techniques: (a) oven based heating; (b) NIR light treatment method.....	69
Figure 4.2 SEM images of (a-1) GNP; (a-2) GNP/PDMS; (b-1) RGO; (b-2) RGO/PDMS .....	71
Figure 4.3 SEM images of the cracks (a-1) collapsed GNPs on the crater of the micro-crack; (a-2) GNPs aiding load transfer; (b-1) RGO between the crack openings; (b-2) cracking of RGO filler after peeling of PDMS. Scale bar: 500 nm in all the images. ....	72
Figure 4.4 Raman spectra of (a) D band, (b) G band, (c) 2D band of GNP, RGO, GNP/PDMS, and RGO/PDMS, (d) and (e) ratio of $I_G/I_D$ and $I_G/I_{2D}$ versus shear mixing time respectively .....	73
Figure 4.5 Load transfer: G band shift in (a-1) GNP/PDMS and (b-1) G band shift; change in wavenumbers with strains of (a-2) GNP/PDMS and (b-2) RGO/PDMS.....	77

Figure 4.6 G-band FWHM value of GNP/PDMS (a) and RGO/PDMS (b) polymerized by conventional baking (blue) and NIR photon-assisted method (red) versus strain.....	80
Figure 4.7 Cyclic stress-strain curves (a-1) and stress-strain curves (a-2) until failure of pure PDMS, RGO/PDMS, and GNP/PDMS polymerized by conventional baking method; Cyclic stress-strain curves (b-1) and stress-strain curves (b-2) until failure of pure PDMS, RGO/PDMS, and GNP/PDMS polymerized by NIR photon-assisted method.....	82
Figure 4.8 (a) Young's modulus versus NIR light dose for RGO/PDMS (red line) and GNP/PDMS (blue line) fractions; (b) change in Young's modulus versus weight percentage of RGO (red line) and GNP (blue line) for NIR light treated. ....	84
Figure 5.1 The SEM images of (a) MWNT <sub>1</sub> RGO <sub>0</sub> /PDMS, (b) MWNT <sub>0</sub> RGO <sub>1</sub> /PDMS, (c) MWNT <sub>0.5</sub> RGO <sub>0.5</sub> /PDMS, each with a scale bar of 500 nm. (d) The Raman spectra of (a-c) samples. (e) The comparison of 2D peaks between pure RGO and a series of MWNT- RGO/PDMS composites. ....	92
Figure 5.2 (a-c) The SEM images of MWNT <sub>x</sub> RGO <sub>1-x</sub> /PDMS matrix, and (d) the schematic representation of the RGO-MWNT/polymer system based on the above SEM images. ....	96
Figure 5.3 (a-1) & (b-1) plot the Raman intensity versus the shift in wavenumber under uniaxial tension and under uniaxial compression for MWNT <sub>1</sub> RGO <sub>0</sub> and MWNT <sub>0</sub> RGO <sub>1</sub> , respectively; (a-2) & (b-2) plot the change of the shift in	

wavenumber versus the strain under uniaxial tension and under uniaxial compression for MWNT <sub>1</sub> RGO <sub>0</sub> and MWNT <sub>0</sub> RGO <sub>1</sub> , respectively.....	98
Figure 5.4 Load transfer (G-band) in RGO <sub>0.9</sub> MWNT <sub>0.1</sub> /PDMS: (a) the Raman intensity versus wavenumber; (b) the change of the Raman peak in wavenumber as a function of the strain; and (c) the Raman peak shift in wavenumber versus the relative weight fraction of nano-carbons under 50% uniaxial tension. ....	101
Figure 5.5 (a) Model describing the change in orientation of the nanotube in polymer on application of a uniaxial tensile strain, (b) the change in Raman wavenumbers for G and 2D band (measured) versus change in orientation angle (calculated) for different uniaxial tensile strains applied to the sample. ....	104
Figure 5.6 The Full Width Half Maximum (FWHM) data for the different compositions of MWNT <sub>x</sub> RGO <sub>1-x</sub> /PDMS: (a) the FWHM versus weight fraction of the nano- carbon; (b) the FWHM change versus percentage strain for MWNT <sub>1</sub> RGO <sub>0</sub> /PDMS; (c) the FWHM change versus strain for MWNT <sub>0</sub> RGO <sub>1</sub> /PDMS; and (d) the FWHM change versus strain for MWNT <sub>0.1</sub> RGO <sub>0.9</sub> /PDMS.....	106
Figure 5.7 The Young's modulus versus weight percentage of nano-carbon filler for MWNT <sub>x</sub> RGO <sub>1-x</sub> /PDMS composite calculated using the rule of mixtures and compared to the experimental data. ....	111
Figure 5.8 The photo-mechanical responses and the actuation stress response of binary mixture nano-carbons polymer composites actuator for 15% pre-strain.....	113
Figure 5.9 (a) Actuation and (b) relaxation of the binary mixutre nano-carbons polymer composites actuator.....	114

Figure 5.10 The comparison of increasing photomechanically induced stress change in binary mixture nano-carbons polymer composites actuator as a result of NIR illumination: (a) plain PDMS; (b) MWNT <sub>1</sub> RGO <sub>0</sub> /PDMS; (c) MWNT <sub>0</sub> RGO <sub>1</sub> /PDMS; (d) MWNT <sub>0.1</sub> RGO <sub>0.9</sub> /PDMS. ....	115
Figure 5.11 The average photomechanically response versus the pre-strain of binary mixture nano-carbons polymer composites actuator with different weight ratio .....	116
Figure 6.1 The spectrum profile of halogen lamp with UV filter .....	121
Figure 6.2 The XPS spectra of (a-1) GNP, (b-1) RGO, and (c-1) MWNT; C 1s binding energy of (a-2) GNP, (b-2) RGO, and (c-2) MWNT; O 1s binding energy of (a-3) GNP, (b-3) RGO, and (c-3) MWNT. ....	122
Figure 6.3 The XPS peaks of O1s, C1s, and Si2p measured for the MWNT/PDMS composites synthesized by (a) the conventional baking method and (b) NIR photon-assisted polymerization. ....	126
Figure 6.4 The XPS peaks of O1s, C1s, and Si2p measured for the RGO/PDMS composites synthesized by (a) the conventional baking method and (b) NIR photon-assisted polymerization. ....	128
Figure 6.5 (a-1) The chemical structures of the PDMS oligomer and the PDMS cross-linker; (a-2) the reaction model of the conventional baking polymerization; (a-3) the reaction model of the NIR photon-assisted polymerization. ....	131
Figure 7.1 The schematic of the RGO film transfer process .....	137
Figure 7.2 The demo structure of strain sensor.....	138

Figure 7.3 The test setup to measure the strain-resistance relationship of the strain sensor:  
(a) a schematic diagram of the test setup, strain is applied to the both ends of the sensor, and two-probe electrode connections are made at both ends of RGO film using copper wires; (b) the strain sensor free of strain; (c) strain sensor under 100% strain..... 139

Figure 7.4 (a) The SEM images of the RGO film under different magnifications; (b-1) the XPS spectrum of the RGO film; (b-2) the C1s and (b-3) the O1s peaks with multiple-component simulation. .... 140

Figure 7.5 (a) The clear pattern of the ~ 80µm RGO stripes with ~20 µm spacing; (b) the sharp pattern edge formed by etching. .... 141

Figure 7.6 (a) The SEM cross-section image of the sandwich-structured strain sensor; (b) the large diameter ~ 10 cm sandwiched structure laminar composites; (c) the sheet resistance and the transmittance at 600 nm of different thickness. .... 142

Figure 7.7 (a) The resistance of the strain sensor over time under 100 times cyclic loading of 5% tension strain, the inset is five times cyclic loading in detail; (b) resistance change versus strain of strain sensor; (c) the cyclic stress-strain curves of strain sensor; (d) the resistance change of the strain sensor under cyclic loadings of different maximum strain. .... 144

Figure 7.8 The mechanism of PDMS/RGO/PDMS sandwiched structure strain sensor: (a) the strain sensor free of strain; (b) the strain sensor under the tensile strain. .... 147

## **CHAPTER 1 INTRODUCTION**

Natural and synthetic polymers are widely used in industry to produce paper, rubber, plastic, fabric, fiber, and more. Polymers consist of long molecular chains, each more or less with base units (monomers) repeated along the chain periodically or randomly. Synthetic polymers are formed by polymerization of monomers, generally via two schemes: chain growth polymerization and step-wise polymerization. The properties of a polymer depend strongly on the polymer chain length which may be determined by controlling the conditions of polymerization. The physical properties of a polymer can also be markedly changed by modification of the bonding between the chains and between the monomers. For example, adding reinforcement materials into a polymer matrix may drastically improve its properties. Some conventional fiber reinforcements, which include natural wood fiber [1], carbon fiber [2], glass fiber [3], steel [4] and alumina fiber [5], are mixed as additions into the polymers to enhance the mechanical/electrical properties. In comparison to those conventional reinforcement materials, nano-scale reinforcements are much more effective in terms of increasing the area of the reinforcement/polymer interface [6, 7]. Further, nanoscale reinforcements such as nanotubes and graphene have demonstrated some of the highest mechanical strength, thermal conductivity of any man made material. Further, unique electrical properties of these reinforcements can impart electrical properties such as conductivity,

photoconductivity in these polymer composites. Thus, adding even a small amount of nano-scale reinforcements may significantly improve the properties of the polymer [8, 9].

Of the nano-scale reinforcement materials discussed in this dissertation, carbon nanotube (CNT) was first discovered in 1991 [10] and graphene was first successfully isolated in 2004 through micro-mechanical alleviation of graphite [11]. Both CNTs and reduced graphene oxide (RGO) which is chemically or thermally derived form of graphene oxide were consequently shown to have excellent electrical, mechanical, and thermal properties. Therefore, they are potential candidates as nano-scale reinforcements for developing advanced polymer composites. Due to the superior properties of nano-scale reinforcements such as low density, high elastic moduli, high electrical and thermal conductivity, polymer nano-composites are excellent systems to study for their applications in aerospace [12], automotive [13], structures [14], packaging [15], tribological [16] and biomedical applications [17]. However, the determining factor that improves the mechanical properties such as load transfer, interfacial stress and Young's modulus is the nan-carbon/polymer interface.

In the past, the nanocarbon/polymer interface has been demonstrated to play the most important role in the efficient stress transfer to the nanotube and determination of the overall mechanical properties of the nanotube-polymeric composite [18]. Ajayan *et al.*, first demonstrated the load transfer in MWNT/epoxy system using Raman spectroscopy [19]. The enhanced shift in Raman G' mode during compression demonstrated higher interfacial shear stress and load transfer to the nanotube [19]. Since then, numerous reports have demonstrated enhanced load transfer to the nanotubes through strategies including surface functionalization of nanotubes [20-22], refluxing

CNTs with nitric acid to create carboxyl, carbonyl and hydroxyl groups [23, 24], side wall functionalization for better dispersion of nanotubes in the matrix [25], and alignment of nanotubes in the matrix [26], in-situ melting and polymerization [27, 28], melt compounding [29] and more recently using flexible spacers at the nanotube-polymer interface [30]. The work by Zhang *et al.*, is notable that achieved an impressive increase in Young's modulus values of ~214% for just 2 wt % of MWNT in polymer matrix [29]. Similarly, there is wide variety of interesting studies on graphene polymer composites.

Defect free sheets of single layer graphene (SLG) exfoliated mechanically from graphite flakes was measured to have second order elastic stiffness of 340 N/m, breaking strength of 42 N/m and Young's modulus of 1.0 TPa [31]. Such excellent mechanical properties of exfoliated SLG warrant their investigation as fillers in advanced polymer composites. Recently, interfacial stress transfer of exfoliated SLG transferred on top of polymer substrate was demonstrated using Raman spectroscopy [32, 33]. Significant shift in the Raman G' or 2D bands ( $> -50 \text{ cm}^{-1}/\%$  strain) were observed, demonstrating load transfer to the carbon layer [32, 33]. Since then interfacial load transfer was reported for few layer graphene comprising of graphene nanoplatelets (GNPs) that were mixed with polymer such as poly(dimethylsiloxane) (PDMS) in bulk [34]. Un-zipping multiwall nanotubes into graphene nano-ribbons have yielded 22% improvement in mechanical strength in epoxy based composites [35]. Several studies on exfoliated graphite based polymer composites have shown enhanced mechanical strength, toughness, glass transition temperature, increase in electrical conductivity and gas barrier properties [36-43]. The work by Coleman *et al.*, is notable as it yielded a ~100 times increase in Young's modulus at 3% strains for 50 wt. % exfoliated graphene drop casted in

polyurethane [43] (The term ‘wt. %’ used throughout the dissertation refers to the ratio of carbon additive to PDMS base compound.). While these studies are impressive reiterating the importance of graphene as filler materials in polymer composites, current methods of fabrication of advanced polymer composites using mechanically exfoliated graphene are quite limited. This is due to the fact that yield of mechanically exfoliated graphene at present is limited to 1 wt. % which could be increased to 7-12% [44]. In this context, the use of chemically reduced graphene as fillers in polymer composites becomes quite interesting and warrants investigation for development of low cost and high strength advanced composites. Graphene sheets chemically derived from graphene oxide (GO) using Hummer’s method and subsequent reduction by hydrogen plasma has been heralded as one of the methods for large scale production of graphene suitable for industrial use [45]. Microscopic characterization of such graphene sheets has shown large unoxidized graphitic regions in between defective clusters and therefore could witness interesting mechanical properties [46]. Recent studies have shown that despite the defects in their lattice, such sheets have shown extraordinary stiffness with Young’s modulus  $E=0.25$  TPa, approaching that of pristine graphene, with high flexibility and lower built-in tension compared to exfoliated graphene sheets [45]. Therefore, studying the interfacial load transfer and mechanical properties of reduced graphene sheets in polymers can make progress in the area of low cost, high strength and scalable composites based on graphene.

Single walled carbon nanotubes, multi-walled carbon nanotubes [47], and graphene [48] were shown with high absorbance of near-infrared (NIR) light, giving rise to effective photo-thermal heating. Applications of such nanoscale photo-thermal heating

include the bio-nanotechnology study to kill cancer cells [47, 49], targeted drug delivery [50], photo-mechanical actuators [51], and laser-assisted photo-thermal imprinting in polymeric materials [52].

In this dissertation, we explored a novel method to polymerize nanocarbon-polymeric composites, where nano-carbon materials act as energy transducers as well as reinforcement materials, in order to strengthen the interfacial load transfer and improve the mechanical properties of composites. Single walled carbon nanotubes, multi-walled carbon nanotubes [47], and graphene [48] were shown with high absorbance of NIR light, giving rise to effective photo-thermal heating. Applications of such nanoscale photo-thermal heating include the bio-nanotechnology study to kill cancer cells [47, 49], targeted drug delivery [50], photo-mechanical actuators [51], and laser-assisted photo-thermal imprinting in polymeric materials [52]. Using NIR light to irradiate the nanocarbons (CNTs, RGOs, and GNPs) dispersed in the polymeric matrix could create significant heating of nano-carbons which can enhance the cross-linking process, also excite the electron to create the covalent bonding between nanocarbons and polymer molecule, thereby strengthening the nanotube-polymer interface. This is a new paradigm in polymerization of the samples by enabling the crosslinking to start at the nanotube-polymer interface using photo-thermal heating of nano-carbons. This type of polymerization and strengthening cannot be achieved by the oven based convective heating where heat flows through the sample from the outside to the inside. Raman spectroscopy and RSA are used to study the interfacial load transfer and the Young's modulus of the composites.

In this dissertation we have explored this novel NIR light induced polymerization technique and have created applications in the area of strain sensing. The organization of the thesis is as follows: Chapter 2 gives a brief description of the structure and the properties of different nano-carbons, polymers and the polymer composites reinforced with the nano-carbons. The important role of the interface of the composites is emphasized. It also gives an introduction and fundamentals of Raman spectroscopy and X-ray photoelectron spectrum (XPS).

Chapter 3 discusses the novel NIR photon-assisted polymerization of nanotube/polymer composites. Using rheometric system analyzer (RSA, TA instruments-Waters LLC) and Raman spectroscopy, these composites were shown to demonstrate higher stiffness and enhanced load transfer to the reinforcements than the corresponding composites prepared by convention baking. Large Raman shifts ( $20\text{ cm}^{-1}$  wavenumbers) of the 2D bands were measured for NIR light polymerized samples, signifying increased load transfer to the nanotubes for up to ~80% strains. An increase in Young's modulus of ~130% for 1 wt. % composites is measured for photon assisted crosslinking.

Chapter 4 discusses the NIR photo-assisted polymerization of polymer composites reinforced with graphene (2.5D GNP and 2D RGO). The comparison of the NIR polymerization with conventional vacuum oven based polymerization for both RGO and GNPs revealed larger change in the wavenumbers of the G band and increased load transfer for the former. When compared with the conventionally polymerized samples, the measured Full Width Half Maximum (FWHM) data of the NIR treated samples revealed smaller change at large strains indicating minimum slippage. The obtained

stress-strain curve also shows higher Young's modulus for the NIR treated samples than those polymerized by the conventional baking.

Chapter 5 investigates the synergistic effect in the binary nano-carbons/polymer composites synthesized by the NIR photon-assisted polymerization. By using Raman spectroscopy, it reveals that the enhanced load transfer and mechanical strength is due to the synergy in the binary mixtures of nano-carbon/polymer composites. For example, small amounts of MWNT<sub>0.1</sub> dispersed in RGO<sub>0.9</sub>/PDMS samples (subscripts represent weight percentage) reversed the sign of the Raman wavenumbers from positive to negative with application to uniaxial strain. This also led to improvement in mechanical properties such as load transfer and Young's modulus. Synergistic samples of MWNT<sub>0.1</sub> RGO<sub>0.9</sub>/PDMS exhibited an improvement in Young's modulus of ~103% much larger than their pure polymer counterparts. Chapter 6 presents the mechanism of the NIR photon-assisted polymerization by using XPS. XPS is widely used to identify chemical bonds. In this dissertation and in general, XPS is for the first time used to study the difference between the NIR photon-assisted polymerization and the conventional baking polymerization. Higher C-O and Si-O bonds were measured for the NIR treated composites. It suggests that the covalent bonds are formed between nano-carbons and polymer matrix during the NIR photon-treated process.

Chapter 7 explores the potential of the application of the NIR photon-assisted polymerization for large scale polymerization of flexible electronics, and flexible strain sensor. A new RGO film transfer process and the patterned RGO film by using photolithography are also described in Chapter 7.

Chapter 8 summarizes the PhD work and discusses some future works related to the NIR photon-assisted polymerization.

A list of the original contributions from this dissertation is as follows:

(1) Development of novel NIR photon-assisted polymerization method to fabricate multi walled carbon nanotube/polymer composites.

(2) Investigated the NIR photon-assisted polymerization of graphene/polymer composites. Load transfer and mechanical properties of composites are also studied.

(3) Demonstrated the enhanced load transfer and mechanical strength due to the synergistic effects in binary nano-carbons, first explain the phenomenon by using Raman spectrum.

(4) Investigated X-ray photoelectron spectroscopy to study the nano-carbon/polymer composites interface polymerized by conventional method and NIR photon-assisted polymerization method.

(5) Development of the mechanism of NIR photon-assisted polymerization

(6) Development of new transfer method for reduced graphene oxide film.

(7) Design and demonstrate strain sensors based on RGO in polymer composites.

## CHAPTER 2 BACKGROUND REVIEW

### 2.1 Nano-carbon materials

The recent advancements in nanotechnology have led to materials on the nanometer length scales. Silicon nanowires, CNTs, gold nanoparticles and graphene have made tremendous impacts in the area of electronics, photonics, sensors, actuators and biomedical applications [53-62]. In this dissertation we have investigated three different nano-carbon forms namely CNTs, RGO and GNP as reinforcements in advanced polymer composites. The following sections briefly describe their structure and properties of these nano-carbon forms.

#### 2.1.1 Structure of nano-carbon materials

##### 2.1.1.1 Carbon nanotubes

Since its discovery by Ijima *et al.*, CNTs have fascinated researchers from all walks of science and engineering [10]. The interest in CNTs stems from its excellent physical properties such as high mechanical strength, thermal conductivity, electrical conductivity and quantum Hall effect at room temperature. Figure 2.1 shows the

transmission electron microscopy (TEM) image of CNT made by chemical vapor deposition, highly entangled cylinder structure is observed.



**Figure 2.1** The TEM image of carbon nanotubes [63]. Scale bar: 20 nm.

An SWNT may be geometrically viewed as rolling up a graphene sheet seamlessly into a cylinder along a specific tube axis. An MWNT consists of multiple concentric SWNTs. The spacing between the neighboring tubes in MWNTs is about 0.339 nm, close to the interlayer distance of graphite. MWNT was first discovered by Ijima in 1991 [10], and SWNT was discovered later independently by Ijima and Bethune [48, 64]. CNTs have been produced in arc-discharge method [10] and by laser ablation of graphite [65], high-pressure carbon monoxide conversion [66], and chemical vapor deposition [67].

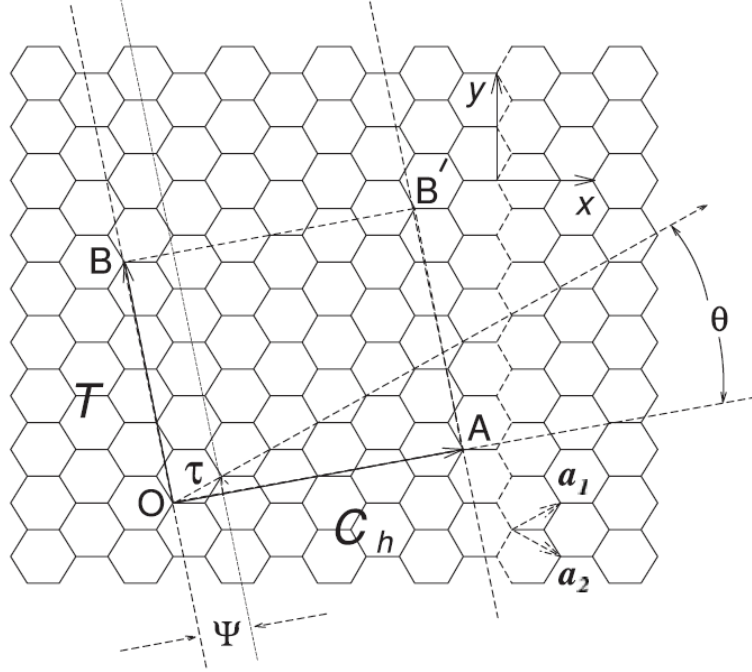


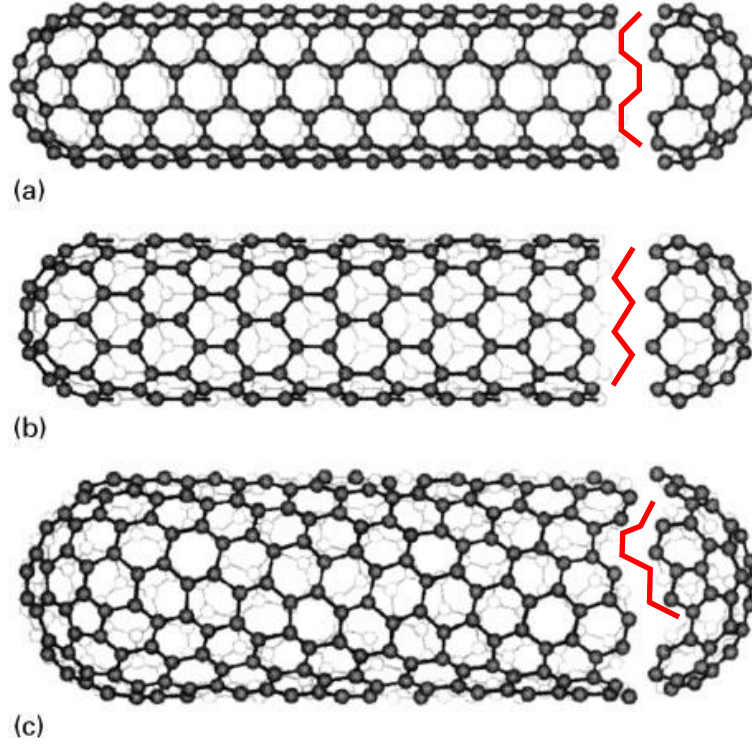
Figure 2.2 A geometrical view of the relationship between carbon nanotube and graphene [68].

Figure 2.2 gives a geometrical view of an SWNT, which can be considered as a seamless roll of a section of graphene, between the two parallel dashed lines, along a certain direction  $\overline{OA}$ . It can be described by its circumference and chirality which are defined by the circumferential vector

$$\overline{C}_h = n\overline{a}_1 + m\overline{a}_2$$

, where  $\overline{a}_1$  and  $\overline{a}_2$  are two appropriate lattice vectors in graphene; n and m are the corresponding integer indices of the two lattice vectors. An SWNT can be specified by the indices (m, n). The chiral angle of an SWNT can be described as

$$\theta = \tan^{-1} \left[ \frac{\sqrt{3}n}{2m+n} \right]$$



**Figure 2.3** The three types of Single-wall Carbon nanotubes: (a)armchair; (b)zigzag; (c) chiral [48].

As shown in Figure 2.3, depending on the chiral angle, SWNTs are defined into three types: armchair ( $\theta = 0$ ), zigzag ( $\theta = 30^\circ$ ), and chiral ( $0 < \theta < 30^\circ$ ) [69]. Also, the armchair, zigzag or chiral SWNTs correspond to  $m = n$ ,  $m = 0$  and  $m \neq n \neq 0$  respectively. MWNTs show a small number of helicities, inferring that some tubes in a MWNT have the same helicity.

Another important parameter of SWNTs, namely the diameter, is given by:

$$d_t = \sqrt{3}a_{c-c}\sqrt{(n^2 + mn + m^2)} / \pi ,$$

where  $a_{c-c} = 1.42 \text{ \AA}$ , is the C-C bond length in graphene.

### 2.1.1.2 Graphene

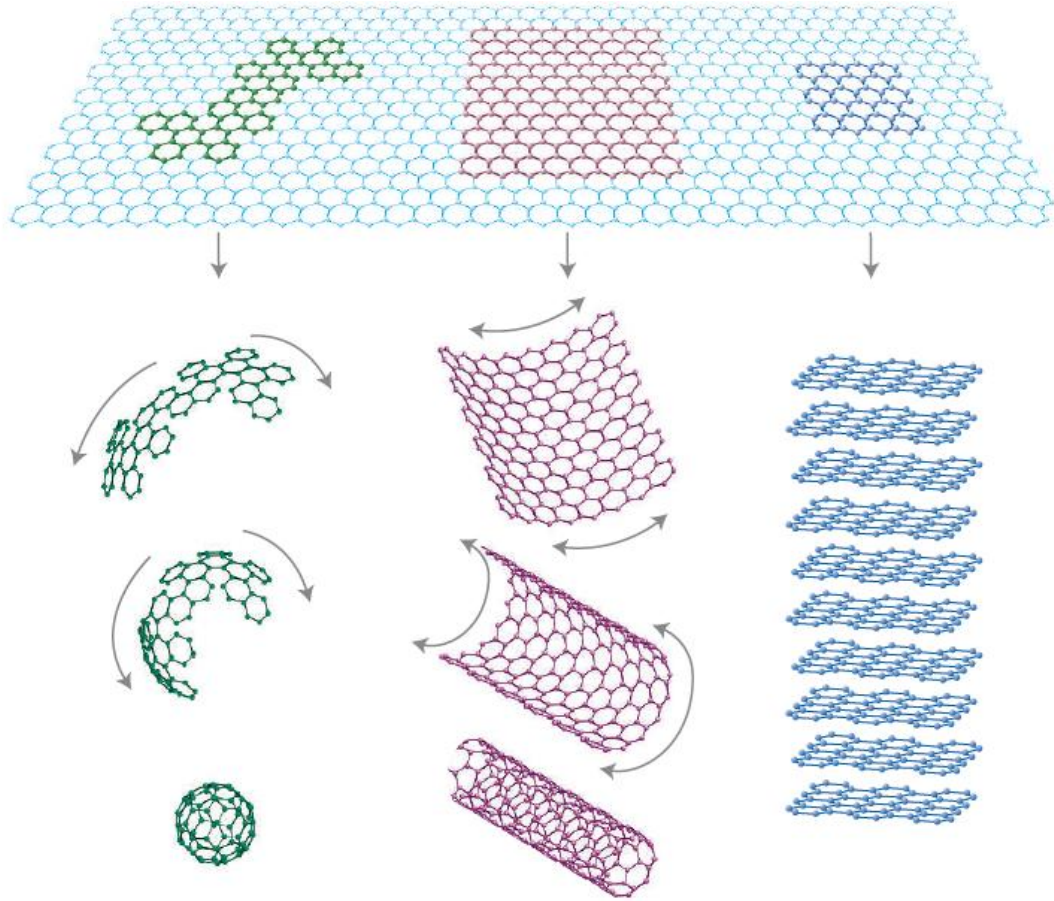


**Figure 2.4** Mother of all graphitic forms. Graphene is a 2D building material of all other dimensionalities. It can be wrapped up into 0D fullerene, 1D carbon nanotube, and 3D graphite [58].

Graphene is the name given to a flat monolayer of carbon atoms tightly packed into a two-dimensional (2D) honeycomb lattice. Each carbon atom is connected with other three carbon atoms through  $sp^2$  bonds (one  $s$  orbital and two  $p$  orbitals) and is a basic building block for graphitic materials of all other dimensionalities (Figure 2.4). It can be wrapped up into 0D fullerenes, rolled into 1D nanotubes or stacked into 3D graphite. Three of the valence electrons are used to form these bonds, which are the same bonds as in diamond, giving graphene high mechanical strength and extraordinary

thermal properties. And the fourth valence electron forms a  $\pi$ -bond, offering excellent electronic properties to the graphene.

The graphene can be described using two lattice vectors shown in Figure 2.2.

$$\mathbf{a}_1 = \frac{a}{2}(3, \sqrt{3}), \quad \mathbf{a}_2 = \frac{a}{2}(3, -\sqrt{3}),$$

where  $a=0.142$  nm is the distance of carbon-carbon bond [59]. Each unit cell contains two atoms. So in each cell there should be two  $\pi$ -bonds, called  $\pi$ -bond and  $\pi^*$ -bond, and  $\pi$ -bond corresponding to valence band and  $\pi^*$ -band corresponding to conduction band. By changing the direction of extending the graphene layer, two types of graphene structure, including zigzag and armchair graphene, are addressed [70].

In the Brillouin zone, graphene consists of two Dirac points at the corners of the zone which are  $K'$  and  $K$  respectively:

$$K = \left( \frac{2\pi}{3a}, \frac{2\pi}{3\sqrt{3}a} \right), K' = \left( \frac{2\pi}{3a}, -\frac{2\pi}{3\sqrt{3}a} \right)$$

Graphene is the basic structure element of carbon allotropes which includes fullerenes, CNTs and graphite shown in Figure 2.4 [58]. And the band structure of graphene was first investigated by Wallace *et al.*, by tight binding method [71]. The linear relationship between the energy of the  $\pi$  electron and their wavevectors in crystal lattice is shown in this study.

More than 70 years ago, Landau and Peierls argued that 2D crystals were thermodynamically unstable and could not exist freely. Their theory pointed out that a divergent contribution of thermal fluctuations in low-dimensional crystal lattices should lead to displacements of atoms that they become comparable to interatomic distances at any finite temperature. Experimental observations strongly support this theory. For

example, the melting temperature of thin films rapidly decreases with decreasing thickness, and the films become unstable (segregate into islands or decompose) at a thickness of, typically, dozens of atomic layers. For this reason, atomic monolayers have so far been known only as an integral part of larger 3D structures, usually grown epitaxially on top of monocrystals with matching crystal lattices. Without such a 3D base, 2D materials were presumed not to exist, until 2004. In 2004, Geim *et al.* first isolated single layer pristine graphene from graphite by a mechanical exfoliation method using scotch tape [11]. The scotch tape was used to peel flakes of graphite off the mesas attached to layer of photoresist. Then the graphite flakes in photoresist were released in acetone. Following isolation, AFM was used to identify the single layer flakes... Epitaxial growth on SiC [72], molecular beam deposition [73], unzipping CNTs [74], sodium-ethanol pyrolysis [75], and chemical vapor deposition [76] have been reported to produce relatively perfect structure of graphene.

#### 2.1.1.3 Reduced graphene oxide (RGO)

Related to the low yield and complicated process of producing pristine graphene mentioned above, another approach method by reduction of graphene oxide (GO) is widely used, and this type of graphene is also called RGO [77]. The graphite is first oxidized, and then chemically exfoliated in the solvents using ultrasonication. Harsh thermal and chemical methods are used to RGO [77]. However, the oxygen is difficult to be removed completely during reduction process and some oxygen groups such as epoxy, carboxylic, carbonyl, ester and alcohol groups are left behind [78]. The SEM image of

RGO is shown in Figure 2.5. While the presence of such defects affect the electronic properties, RGO is highly useful for creating polymer composites due to the chemical groups mentioned above available for functionalization.

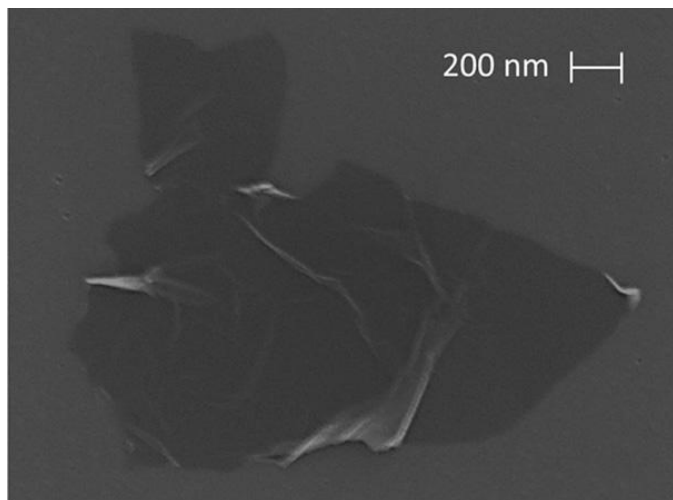


**Figure 2.5** The SEM images of single layer RGO [79].

The structure of RGO was investigated in detail by Gomez-Navarro *et al.* using high resolution TEM and compared with exfoliated graphene in Figure 2.6 [80]. The clean well-crystallized graphene areas are the largest portion in the structure of the RGO layer and cover 60% of the surface. Closed to these areas, carbonaceous absorbates and heavier atoms areas also are significant on the layer. The hexagonal lattice can be clearly observed in the clean well-crystallized graphene areas. Both of them will form larger holes under electron irradiation. However, there is significant amount of topological defects within the clean areas which can be categorized into isolated topological defects and extended topological defects. The extended topological defects appear as quasi-amorphous single layer carbon structures covering 5% of the surface with typical sizes of 1 - 2 nm in diameter. 30% of the total area below the absorbed contamination is unable to

determine the membrane structure. Since the contaminations are preferably stick on defects, the area of defective regions is most likely underestimated. However, the long-range orientational order is still maintained in the presence of such as a significant amount of topological defects.

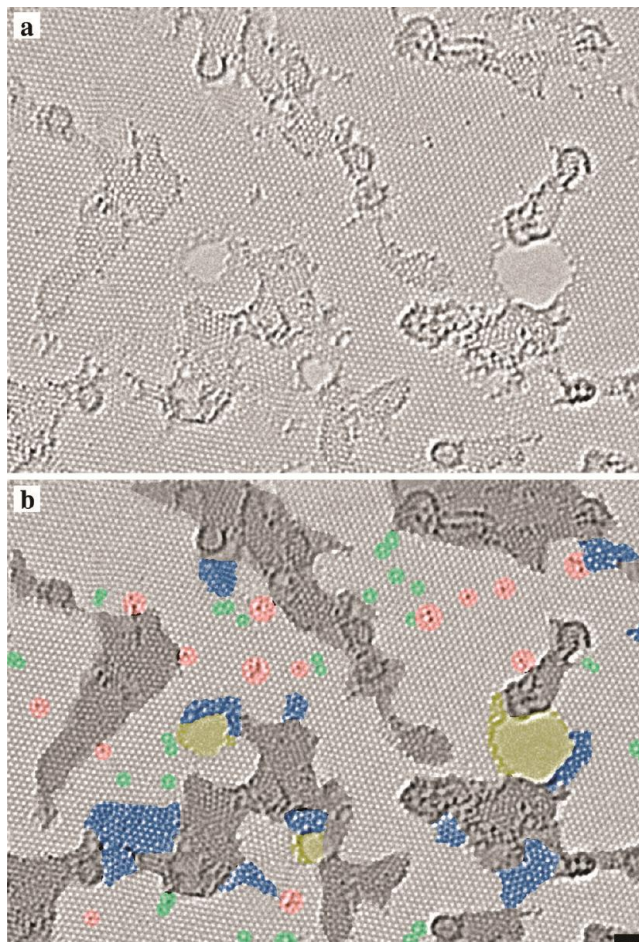


**Figure 2.6** The TEM image of a single layer RGO membrane. (a) Original image and (b) with color added to highlight the different features. The defect free crystalline graphene area is displayed in the original light gray color. Contaminated regions are shaded in dark gray. Blue regions are the disordered single-layer carbon networks, or extended topological defects, that we identify as remnants of the oxidation-reduction process. Red areas highlight individual ad-atoms or substitutions. Green areas indicate isolated topological defects, that is, single bond rotations or dislocation cores. Holes and their edge reconstructions are colored in yellow. Scale bar 1 nm. [80]

All carbon atoms in the extended defects area are bonded to three neighbors in a planar  $sp^2$  configuration. These clustered defects are identified as a remnant of oxidation-reduction process which evolved from the strongly oxidized areas originally. Since these clusters haven't been fully restored, a planar geometry is exhibiting with a strong  $sp^2$ -character. As a result, the single-layer is disordered including pentagons, hexagons, and heptagons within the membrane. It was also suggested by Lerf *et al.*, model that the majority of the carbons with hydroxyl and epoxide groups are arranged within the highly oxidized areas along with undisturbed graphitic regions [46]. Though the exact atomic configurations remain unclear in the oxidized state, the disordered carbon is left after oxidation-reduction process in the vicinity to the crystalline areas. It is observed that the graphene region in vicinity to these defects is distorted. The shifts happen in the direction of lattice and the reduction of lattice spacing occurs. The distortions are typically limited to areas adjacent to the defect cluster and no distortion is observed in large defect-free graphene areas.

#### 2.1.1.4 Graphene nanoplatelet

GNP (Figure 2.7) is average 5-10 nm thickness, containing few layer graphene films with an interplanar spacing of 0.335 nm and held together by van der Waals forces.

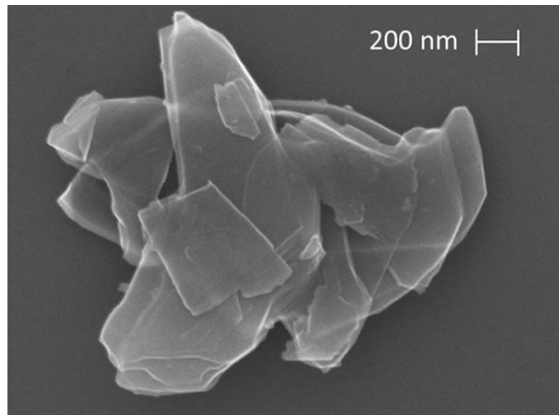


**Figure 2.7** The SEM images of graphene nanoplatelet [79].

There are two structure models, called ABA (Bernal) and ABC (rhombohedral) for few layer graphene with more than two layers (Figure 2.8). For ABA type few layer graphene, which is electrical conductive material, the Hamiltonian can be approximately decomposed into a superposition of the monolayer-like and bilayer-like subsystems [81]. For ABC type few layer graphene, the electronic structure is different with ABA structure. The spectrum of low-energy just contains a pair of conduction and valence band leading to non-conductivity.

Generally, graphite and GNP has an ABA Bernal stacked structure. In this type structure, the separation between the  $\pi$ -bond and  $\sigma$ -bond near the Fermi energy is very large, thus  $\pi$ -bond will play the dominant role in the electronic properties of graphite [82].

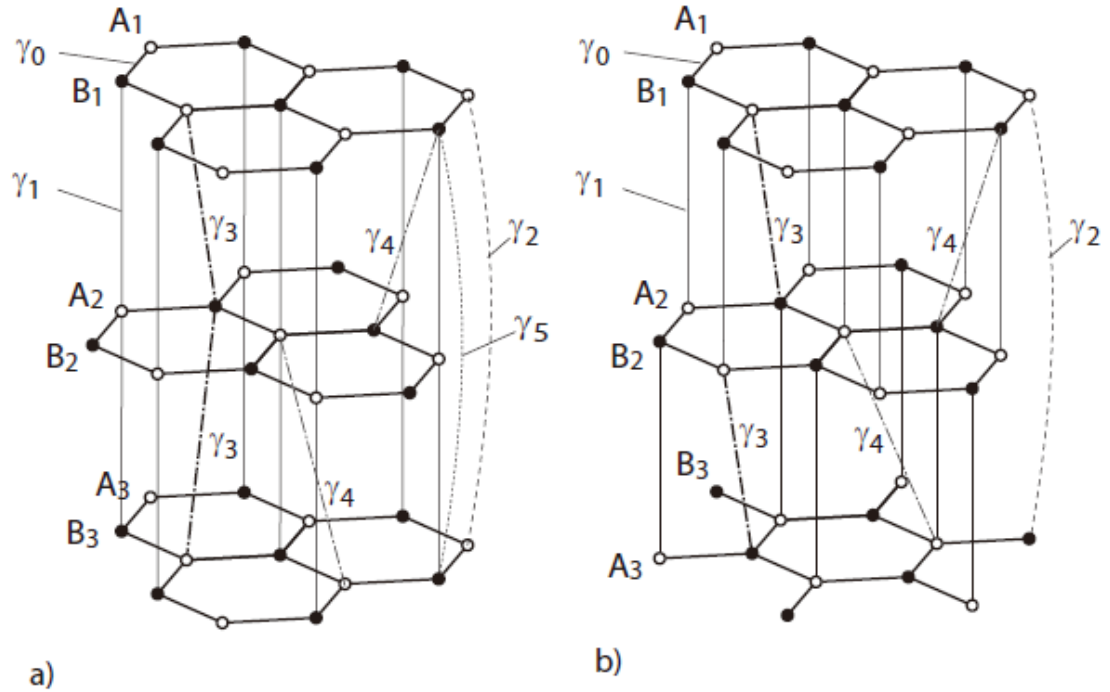


**Figure 2.8** The crystal structure of (a) Bernal stacked and (b) Rhombohedra stacked few layer graphene with the complete set of tight binding parameters [81].

It is first produced by deflagration of graphitic oxide on heating or by reduction of graphitic oxide in alkaline suspension by Boehm *et al.* in 1962 [83]. Other groups like Kim *et al.*, first used e-beam patterning and oxygen plasma etching of mechanically exfoliated graphite to produce sub-50 nm GNPs [84].

## 2.1.2 Properties of nano-carbon materials

### 2.1.2.1 Carbon nanotubes

The strength of CNTs is largely due to fact that the strong  $sp^2$  covalent bonds between carbon atoms form a network except near the tube ends. The theoretical calculations on SWNTs, often considering them defect-free, predicted Young's moduli of

SWNTs between 0.5 TPa and 5.5 TPa [85, 86]. Treacy *et al.* used TEM to expose the individual CNT with high energy electrons, and CCD camera record the vibration of CNT to calculate the Young's modulus of ~0.9 TPa to 2.7 TPa for CNTs was observed [87]. Krishnan *et al.* used the same method to measure the individual SWNT. The results of Young's moduli, inevitably affected by the presence of defects, were measured between 0.9-1.7 TPa [88]. Atomic force microscopy (AFM) was also used to measure the mechanical properties. Yu *et al.* used AFM to supply tensile load to an individual SWNT until failure, and the displacement of AFM tip was recorded to calculate the Young's modulus and tensile strength of SWNT. The high tensile strengths between 13 to 52 GPa and high Young's modulus between 0.32 TPa and 1.47 TPa were reported for SWNT [89, 90].

CNTs not only have excellent mechanical properties, but also outstanding electrical properties. CNTs are quasi-one-dimensional material forming well separated energy bands. Ebbesen *et al.* investigated the electrical conductivity of carbon arc produced CNT. Four 80-nm-wide tungsten leads were patterned by ion-induced deposition on the individual CNT, and four-probe resistance were measured to calculate the electrical conductivity. For metallic tubes, high current density  $\sim 6 \times 10^6 \text{ A/cm}^2$  was observed [91]. Based on the previous work, electrical conductivity of conducting CNTs was in a range of  $10^6$ - $10^7$  S/m [92].

The strong  $sp^2$  bonds in nanotubes suggest high intrinsic thermal conduction. High thermal conductivity 1700 - 5800  $\text{W m}^{-1}\text{K}^{-1}$  of SWNT was observed by Fujii *et al.*. They use a heat rod attached one side of SWNT film and measured the temperature drop

across different thermocouples on the film. The calculation was based on the temperature difference between heat rod and different locations of the film [93].

#### 2.1.2.2 Graphene

Graphene also has the hexagonal lattice of  $sp^2$  bond suggesting that it has similar mechanical, electrical and thermal properties as CNTs. AFM nanoindentation was used by Lee *et al.* to measure the mechanical properties of monolayer graphene. The graphite flakes were mechanically deposited onto the substrate full of circular wells. Suspended monolayer graphene over open holes were studied. Then a constant force was applied through the AFM cantilever at a constant displacement rate, and the force feedback measured by AFM was used to calculate the Young's modulus and strength. High Young's modulus  $\sim 1$  TPa and intrinsic strength  $\sim 0.13$  TPa was reported. [94, 95]. Frank *et al.*, measured the Young's modulus of graphene using the same method and arrived at a value of  $\sim 0.5$  TPa for the Young's modulus [96].

The electrical conductivity of single-layer graphenes  $4.3 \times 10^6$  S/m was reported by Lee *et al.* [97]. In their experiment, the single layer graphene was deposited on a Cu and a Co thin film by chemical vapor deposition. Polymethyl methacrylate (PMMA) was deposited on the as-grown substrate that was etched. After transferring the graphene to a  $SiO_2$  substrate, PMMA was removed by acetone. Oxygen plasma was used to pattern and etch the graphene. Microwave and DC source was used to measure the electrical properties of single layer graphene.

The superior thermal conductivity of single layer graphene in the range of  $4800 \text{ Wm}^{-1}\text{K}^{-1} - 5300 \text{ Wm}^{-1}\text{K}^{-1}$  were reported by Balandin *et al.*. In this experiment, the Raman spectroscopy was used to measure the thermal conductivity. The trenches with 300 nm in depth and 2-5  $\mu\text{m}$  in width were first patterned on  $\text{SiO}_2/\text{Si}$  wafer. The graphite flakes were placed on top of those trenches and exfoliated to obtain single layer of graphene. Then laser light with 488 nm wavelength was focused on the middle of the suspended graphene over the trench, and the G-band shift of the graphene was recorded to calculate the thermal conductivity [98].

### 2.1.2.3 Reduced graphene oxide

Compared to pristine graphene, RGO can be described as a quasi-2D plane of carbon with distorted  $\text{sp}^3$  carbon-carbon bond.

Young's modulus of chemically treated RGO film was reported around 185 GPa by Robinson *et al.*. GO was reduced chemically and patterned lithographically to produce a mechanical resonator. Resonance frequency of the device was used to calculate the Young's modulus of the RGO [99].

Gómez-Navarro *et al.* reported the electrical conductivity in a range of 0.05 - 2 S/cm for the chemical RGO [100]. GO sheets were first deposited on  $\text{SiO}_2/\text{Si}$  substrate and then were chemically reduced. Following Au/Pd electrodes were patterned by e-beam lithography to measure the electrical properties. The conductivity of RGO was measured to be 3 orders higher than GO. Also a significant conductivity decrease by more than 3 orders of magnitude upon changing the temperature from 298 K to 4 K was measured.

Electrical conductivity in the range of 6.2 – 62 S/cm was reported by using four-point measurement [101]. High electrical conductivity of individual RGO sheet was reported between 350 S/cm and 1314 S/cm by other groups [102, 103], around just two order higher than pristine graphene [78].

Thermal conductivities in the range of 0.14 – 2.87 Wm<sup>-1</sup>K<sup>-1</sup> was addressed for thermally RGO [101]. GO flakes were deposited on top of the two isolated electrodes and one of the electrodes was heated at a constant rate while the temperature was measured on the other electrode in vacuum environment. Another study by Shamsa *et al.*, pointed the thermal conductivity of RGO was comparable to that of sp<sup>3</sup> diamond-like carbon material, indicating quasi-2D amorphous carbon structure of RGO [104].

Since the oxygen group and the defects on RGO film strongly affects the properties of RGO film, the mechanical, electrical and thermal properties' value are in a wide range for different process. And these properties are usually used to evaluate the reduction process.

#### 2.1.2.4 Graphene nanoplatelet

Numerical results of high tensile modulus ~ 1TPa, similar to pristine graphene, was reported for few layer graphene [105]. Poot *et al.* also reported the in-plane Young's modulus was around 0.92 TPa which was in good agreement to the numerical results. In their experiment, GNPs were mechanically exfoliated, and AFM was used to apply force to the GNP flake. The force-distance relationship was recorded by using AFM to calculate the mechanical properties [106].

Thermal conductivity of few layer graphene was reported  $\sim 1300 \text{ Wm}^{-1}\text{K}^{-1}$  by Ghosh *et al.*. An 800 nm laser was used to heat the suspended GNP and temperature was measured on the other side. It was seen that the thermal conductivity decreased with increasing the number of graphitic layers [107].

Lee *et al.* measured the GNPs synthesized on a Cu and a Co thin film by chemical vapor deposition. In this experiment, PMMA was deposited on the Cu substrate after the growth of few layer graphene and the substrate was etched. After transferred the GNP to a  $\text{SiO}_2$  substrate, PMMA was removed by acetone. Oxygen plasma was then used to pattern and etch the graphene. The electrical conductivity of GNP was measured to be  $\sim 1.2 \times 10^6 \text{ S/m}$  [97].

In this dissertation, we have explored these three additives (1D MWNT, 2D RGO, and 2.5D GNP) as reinforcements to fabricate and study polymer composites.

## **2.2 Polymer**

Polymers consist of long-chain molecules with repeating structural units. Herman Staudinger first reported this structure of polymer [108]. Polymers are common materials, such as nylon, rubber, and proteins. The man-made polymers are of particular interest because of their specifically designed properties. The properties of polymers, such as viscosity and glass transition temperature, depend on the structure unit, the crosslink between chains, the polymer network, and the molar mass.

Polymerization can be divided into two main schemes: chain growth polymerization and step-wise polymerization. Chain growth polymerization is by linking

the molecules which have double or triple carbon-carbon bonds. Some of these bonds can be broken and replaced by new C-C bonds between monomers, thus producing long chain molecules. The methods of chain growth polymerization include free radical addition polymerization, ionic and catalytic polymerization [108]. Step growth polymerization is through stepwise reaction among monomers with heteroatoms groups like oxygen.

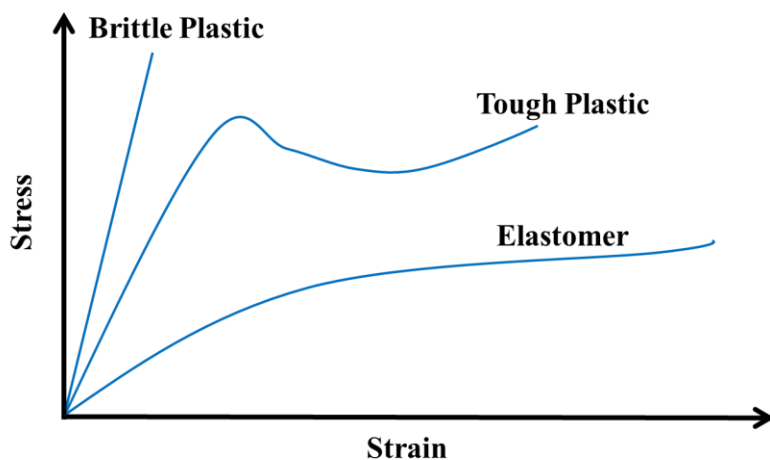


Figure 2.9 The Stress-strain behavior of various polymers [108]

Tensile strength and Young's modulus were measured to evaluate the mechanical properties of the polymers. Tensile strength depends on the crystalline nature of the entanglement of the polymer chains. Allen *et al.* reported that a larger than 90% tensile strength can be attained with eight entanglements in length [109]. Tensile strength also depends on polymer molecular weights. The tensile strength increases rapidly when the molecular weight increases, and then decreases slightly after reaching a certain molecular weight.

The viscosity of polymers increases when the molecular weight increases. The long chain length allows for entanglement which can hold all long chains together.

Depending on the region of viscoelastic behavior, polymers may exhibit quite different mechanical properties. Three basic types of polymer are shown in the Figure 2.9.

Polymers can be divided into two categories based on the physical property related to heating: 1) Thermoplastics which can soften when heated and become hard again when cooled; 2) Thermosets that soften when heated and can be molded but harden permanently.

In this dissertation, PDMS is used as matrix material to synthesize nano-carbon/polymer composites. The elastomer PDMS is a kind of widely silicon-based organic polymer, known for its viscoelasticity properties, which exhibit both viscous and elastic characteristics during deformation, and exhibit elastic recovery from deformations that occur during flow. Compared to the plastic material, viscoelastic material can return to its original shape after removing the load, even though it will take some time. The phenomenon called stress relaxation will be seen by holding at constant strain, which is due to a rearrangement of the long chain molecular in micro scale.

The PDMS is widely used as biomedical device and micro-fluid device due to its low density and great bio-compatible properties. The Young's modulus and shear modulus can be tuned by changing the mixture ratio of PDMS base and crosslinker. The Young's modulus is reported in a range between 360 KPa to 1 MPa.

PDMS is a non-conductive polymer with breakdown voltage  $\sim 2 \times 10^7$  V/m [110]. The PDMS is optically transparent between 240 nm to 1100 nm [110]. Besides, PDMS is a kind of high bio-compatible materials: non-toxic and permeable to oxygen, carbon dioxide and nonpolar organic solvents.

The schematics of their synthesis using a platinum catalyst are shown in Figure 2.10. The cross-linking process occurs when vinyl and silicon-hydride groups undergo a hydro-silation reaction, then forming -CH<sub>2</sub>-CH<sub>2</sub>- linkages between PDMS chains [111].

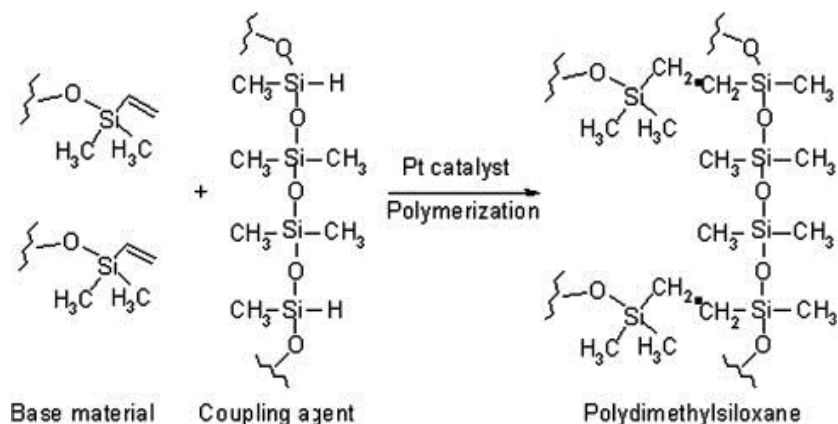


**Figure 2.10 Schematics of PDMS polymerization based on PDMS oligomers and crosslinker [111]**

In the Raman spectra of PDMS shown in Figure 2.11, all the nine peaks related to different vibration modes with Si-O-Si and CH<sub>3</sub> groups in PDMS is addressed. In detail, these nine peaks indicates (1) Si-O-Si symmetric stretching (491 cm<sup>-1</sup>), (2) Si-CH<sub>3</sub> symmetric rocking (687 cm<sup>-1</sup>), (3) Si-C symmetric stretching (701 cm<sup>-1</sup>), (4) CH<sub>3</sub> asymmetric rocking + Si-C asymmetric stretching (787 cm<sup>-1</sup>), (5) CH<sub>3</sub> symmetric rocking (862 cm<sup>-1</sup>), (6) CH<sub>3</sub> symmetric bending (1262 cm<sup>-1</sup>), (7) CH<sub>3</sub> asymmetric bending (1410 cm<sup>-1</sup>), (8) CH<sub>3</sub> symmetric stretching (2904 cm<sup>-1</sup>), and (9) CH<sub>3</sub> asymmetric stretching (2970 cm<sup>-1</sup>).

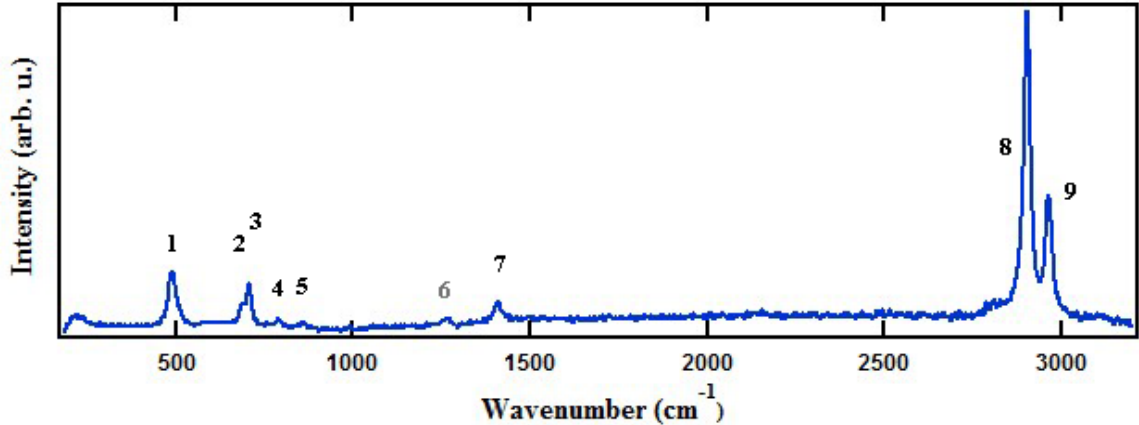


Figure 2.11 The Raman spectra of PDMS. The peaks labeled 1-9 are the different vibrational peaks of Si-O-Si and CH<sub>3</sub> groups.

## 2.3 The methods of fabricating nano-carbon/polymer composites

### 2.3.1 The solution-based method

The solution-based method is the most common method to prepare nano-carbon polymer composites. First, the nano-carbon suspensions and polymer were mixed by magnetic stirring or shear mixing. Then the precipitated composites were extracted or dried to synthesize. Also the mixture solution was directly cast into a mold to dry.

Xu *et al.* reported to use this method to synthesize GO/poly(vinyl alcohol) (PVA) composites. The powdery GO was ultrasonicated in deionized water to make a uniform suspension with the concentration of 1 mg/mL. 5 g PVA was dissolved into 95 g suspension to give 5 wt. % GO/PVA in solution, and then ultrasonicated for 1 h. The composites were collected by vacuum filtration of the mixture solution. The composites film was further dried under vacuum in the oven with 60 °C [112]. Ramanathan *et al.* also synthesized the GNP/PMMA composites by using solution-based method. GNP particles and PMMA were first separately dispersed in tetrahydrofuran (THF) via bath

ultrasonication. Shear mixing at 6000 rpm was supplied to the mixture solution in the ice bath. The ice bath was used here in order to reduce the frictional heat coming from the shear mixing. Then the mixture suspension was dropped into stirred methanol to remove THF. Finally the composites were extracted by vacuum filtration and dried at 80 °C in vacuum oven [113]. Although the solution method was an easy method to synthesize nano-carbon composites, lots of chemical solutions are used which is not environmentally benign and this process need to find the common solvent for the nano-carbon and polymer matrix.

### 2.3.2 The melt compounding method

Melt compounding utilizes high shear forces and high temperature to mix the reinforcement into the thermoplastic polymer matrix without any solvent added.

Kim *et al.* reported the use of melt compounding method to synthesize graphite/Poly lactide (PLA) composites. Graphite was directly mixed with PLA in a mechanical mixer and then melt-compounded using screw extruder with the temperature of 175 - 200 °C. The composites were extruded into a strand and quenched into water. The strands were then dried in vacuum oven for 24 h [114]. Zhang *et al.* used similar techniques to synthesize GO/polyethylene terephthalate (PET) composites. They mixed the graphite into PET and melt compounded the mixture using a shear mixer at 275 °C under 15 MPa [115]. Compared with solution-based method, the advantage of this method is that it does not require use of solvent. The disadvantage is that melt

compounding must be done at high temperature, limiting its use only to thermally stable polymers, also high shear mixing rate will induce the defects to nano-carbons.

### 2.3.3 The in-situ polymerization method

In situ polymerization method [27, 28] is to employ shear mixing to mix reinforcements and monomers together and then add a curing agent to initiate polymerization.

Cochet *et al.* first used this method to prepare MWNT/polyaniline (PANi) composites. Nanotubes were first ultrasonicated in HCl solution to reach a uniform suspension. Then the aniline monomer was added into the suspension, and then a solution of an oxidant was slowly added and ultrasonicated for 2 h in ice bath. Finally the composites was filtered and dried. By using this method, high MWNT loadings (> 50 wt. %) was realized [116]. GNP/epoxy was also fabricated by this method. Yu *et al.*, reported the use of high shear mixing to mix GNP suspension and epoxy resin, and then cure the mixture at 100 °C for 2 h and additional 150 °C for 2 h to completely polymerize the mixture [117]. Wang *et al.*, used *in-situ* anodic electro-polymerization of PANi film on graphene paper to fabricate flexible electrode [118]. In this work, graphene suspension was passed through the cellulose membrane to fabricate a film of graphene, and this film was used as an electrode in a solution of 200 ml 0.05 M aniline monomer and 0.5 M H<sub>2</sub>SO<sub>4</sub>. The potential of graphene r electrode was set to shift from open circuit potential to 0.75 V at a rate of 10 mV/s and then kept constant to synthesize graphene/PANi composites [119].

### 2.3.4 The chemical functionalization method

Chemical functionalization of nanotube and graphene to improve interfacial bond strength has been demonstrated by several groups. This method can be mainly divided into three categories: defect functionalization, covalent functionalization, and non-covalent exhedral functionalization with polymer or surfactant. In details, 1) defect functionalization: strong acids, oxidants, ozone are used to damage the nano-carbons and attach oxygen group on the defects. Zhu *et al.* reported the functionalized CNT to improve the dispersion in epoxy matrix. First HCl was added to the suspension to open ends of the SWNTs with carboxylic acid group, and then SWNTs-COOH were fluorinated in the oven at 150 °C for 12 h, the gas flow ratio of fluorine, hydrogen and helium were set as 2:1:30 respectively to form F-SWNT-COOH. Solution-based method was used to synthesize SWNT/epoxy. Higher modulus and tensile strength was observed [20]. Hill *et al.* reported that acid-treated MWNTs and SWNTs can reach better dispersion in polystyrene copolymer and have better properties than those without acid-treatment [120]; 2) covalent functionalization [20-22]: this method is based on the covalent bond of functional groups onto carbon form of CNTs, It can be performed at the end caps of nanotubes or at their sidewalls which have many defects. The fluorine atom on fluorinated CNT can be replaced by amino or hydroxyl groups without further damage the structure of nano-carbons [121]; 3) non-covalent exhedral functionalization with polymer or surfactant: this method is achieved by wrapping nano-carbons with polymers or surfactants [122]. Gong *et al.* report to use C<sub>12</sub>EO<sub>8</sub> surfactant, which contain an oxyethylenated hydrophilic segment and a hydrocarbon hydrophobic segment, to help

disperse CNT in epoxy. After stirring for 15 m, the mixture solution was put into mold, cured in room temperature overnight and then cured at 80 °C for 2 h and 120 °C for 2 h to fully synthesize the composites [123]. It is of note, however, that although surface chemical functionalization of nano-carbons can be used to increase interfacial shear stress transfer, it induces defects and changes the structure of nano-carbons.

In this dissertation, we use evaporative method and shear mixing method to the nano-carbons inside the polymer, and then the conventional polymerization and NIR photon-assisted polymerization are used to fabricate nano-carbon composites.

a. Evaporative method

An ultrasonication-evaporative mixing fabrication process was used to prepare homogenous dispersion of nano-carbons in the polymer matrix. To specify, nano-carbons were ultrasonicated in isopropyl alcohol (IPA) solution for 4-10 hrs, with the length of the duration depending on the type of nano-carbons. During ultrasonication, cavitation occurs and the cavitation bubbles collapse causing very high strain in the solution. Afterwards, evaporative mixing of polymer is applied with the nanocarbon-IPA suspension by using magnetic stir bar (300 RPM) for 24 hrs at 65 °C. During the period, IPA slowly evaporated, leaving a nano-carbon/polymer mixture. The temperature was monitored constantly to ensure that the solution was warm but not boiling. The nano-carbon/polymer changed consistency when IPA was evaporated. The complete removal of IPA was verified through monitoring both the consistency and the container markings of the initial polymer compound level. After removal of IPA, the nano-carbon was dispersed homogeneously into the polymer matrix.

b. Shear mixing

For this method, a stepping motor was used to rotate the blade to induce shear stress in the nano-carbon/polymer mixture. During mixing, the energy delivered into the mixture solution is equal to the attained shear stress. The shear stress can be expressed as

$$\sigma_s = \eta \cdot \gamma$$

, where  $\eta$  is fluid viscosity and  $\gamma$  is fluid strain rate.

The fluid strain

$$\gamma = R \cdot \omega / h$$

, depending on the rotational speed ( $\omega$ ) of the mixer blade, the radius ( $R$ ) of the mixer, and the spacing ( $h$ ) between the edge of the blade and the container. The shear stress can induce a pulling effect on the nanocarbons to achieve homogenous dispersion of the nanocarbons. Our study employed a laboratory shear mixer with a stepping motor operated at 300-1000 rpm. For each type of nanocarbons, the rotator speed and the time duration were optimized.

## **2.4 The polymer composites based on carbon nanotubes and graphene**

### **2.4.1 Nanotube/polymer composites**

The research on the CNT/polymer composites has been driven by the excellent mechanical, thermal, and electrical properties of CNTs. Shaffer and Windle conducted the first systematic study of the mechanical properties for such systems was conducted on the MWNT/PVA composites [124]. Later, Cadek *et al.* reported better results on the MWNT/PVA composite showing an 80% increase of Young's modulus and a 60%

increase of hardness with addition of 1 wt. % of nanotubes [125]. Qian *et al.* studied the mechanical properties of CNT/polystyrene composites. They reported a 42% increase in the stiffness with 1 wt. % nanotubes [126, 127]. Xu *et al.* achieved a 20% increase in Young's modulus of the CNT/epoxy composite with 0.1 wt. % MWNT added [128].

CNTs are excellent heat conductors, exhibiting high thermal conductivity particularly along the tube axis. The thermal conductivities of SWNT/epoxy composites have been evaluated by Biercuk *et al.*, showing a 70% increase at 40 K and a 125% increase at room temperature with addition of 1 wt. % SWNT. They reported the percolation threshold as between 0.1 and 0.2 wt. % of SWNTs admixed in the SWNT/epoxy composite [129].

In comparison to polymers, nano-carbon/polymer composites were also shown with improved electrical and optical properties. Sandler *et al.* reported a 100  $\Omega$ -m electrical resistivity with as low as 0.1 vol. % of CNTs added [130]. Lozano *et al.* reported the percolation threshold as between 9 and 18 wt. % of CNTs in nanotube/polypropylene composites [131]. Adding MWNTs into polyaniline, which is a conducting polymer, was also shown to lower the electric resistivity by an order of magnitude at room temperature. Because of such a drastic improvement, MWNT/Polyaniline composites were used as printable conductors by DuPont [132].

CNT/polymer composites can also be used to fabricate light-emitting diodes (LED) and photovoltaic device, taking advantage of their excellent optoelectronic properties. Adding CNTs in poly(p-phenylene vinylene) (PPV) was shown with up to eight orders of magnitude of increase in the electrical conductivity with no degradation of the optical properties [133]. Romero *et al.* fabricated a nanotube/PPV photovoltaic device

and successfully demonstrated the diode behavior [134]. Ago *et al.* also proved that for the nanotubes embedded in the polymer the recombination process is remarkably reduced and, as such, the excited electron-hole separation is accordingly improved [135]. The nanotube/poly(3-octylthiophene) composites were shown with considerable enhancement of the photovoltaic effect by Kymakis and Amaratunga [136]. Chen *et al.* measured the third-order nonlinearity on the SWNT/polyimide composites [137].

#### 2.4.2 Graphene/polymer composites

Pristine single layer graphene is one of the stiffest materials with Young's modulus of ~1 TPa. This makes graphene an ideal candidate as fillers for developing advanced polymer composites. Compared to CNTs, graphene has many advantages. Its large surface-to-volume ratio enables graphene to more effectively change the polymer matrix than nanotube [138]; its flat structure make grapheme more susceptible to uniform dispersion into the polymer matrix without aggregation; its plane-to-plane contact can drastically increase the electrical and thermal conductivities [139]; Its wrinkled nature leads to strong interface bonding with the polymer matrix; the cost is low for GO and RGO and the yields are high. However, the experimental results showed that these advantages might be outweighed by the advantages of CNTs such as easy orientation and better mechanical properties [140].

Using graphene as the reinforcement has been shown to improve mechanical properties of polymers. Adding 2 wt. % of graphene, by the method of directly sonicating and exfoliating graphite into PVC matrix, was shown as achieving 130% increase of the

tensile strength [141]. Bao *et al.* reported that the tensile strength and the Young's modulus increased 66.3% and 66.7% respectively after adding 0.8 wt. % of chemical reduced graphene oxidized (CRGO) in PVA [142]. The CRGO/PMMA composite with 1 wt. % of CRGO was shown to yield 60.7% increase of the tensile strength by Wang *et al.* [143].

In addition to the improvement in the mechanical strength, graphene/polymer composites can also attain improved electrical properties. A theoretical study by Xie *et al.* suggested that graphene can increase the electrical conductivity for the composites more than CNTs [144]. Studies were carried out by adding graphene into polymers such as polyolefin, polyester, polyamide, polyurethane, and epoxy. Stankovich *et al.* found that the lowest electrical percolation threshold was 0.1 vol. % CRGO in PS and the conductivity can reach  $0.1 \text{ S}\cdot\text{m}^{-1}$  for 1 vol. % CRGO/PS [138]. With graphene foam (GF) added at 0.5 wt. %, the GF/PDMS composites were shown with very high electrical conductivity of  $1000 \text{ S}\cdot\text{m}^{-1}$  [145]. The thermal stability and the thermal conductivity were also shown to improve. More The 25 vol. % thermal reduced graphene oxidized (TRGO)/epoxy composite was shown with the thermal conductivity increased by a factor of over 30 [139]. The 2 wt. % CRGO/PS composite was shown by Fang *et al.* [146] with a 260% increase of thermal conductivity.

Additionally, adding a small amount of graphene in polymer was shown as capable of modifying the catalytical properties [147].

## **2.5 Methods of characterization nano-carbon/polymer composites**

## 2.5.1 Introduction to Raman Spectroscopy

Raman spectroscopy is the inelastic scattering of light by matter, from molecules to crystals. This effect is highly sensitive to the physics and chemical properties of the scattering material and to any environmental effect on these materials. That is the reason the Raman spectroscopy is seen as one of the most useful tools for developing in nano-/micro- materials science.

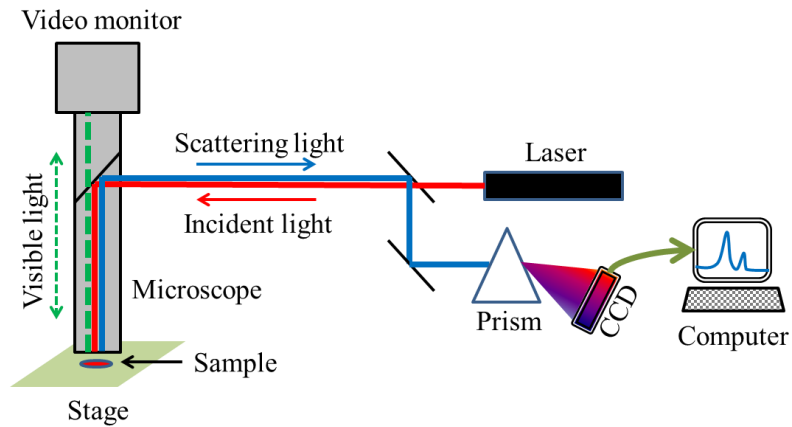


**Figure 2.12 The schematic of a Raman spectrometer**

Many advantages of using Raman spectroscopy are shown in material characterization: the measurement is simple without special sample preparation; can be used to study material properties at room temperature and under ambient pressure [148]. The schematic of a Raman spectrometer is shown in Figure 2.12.

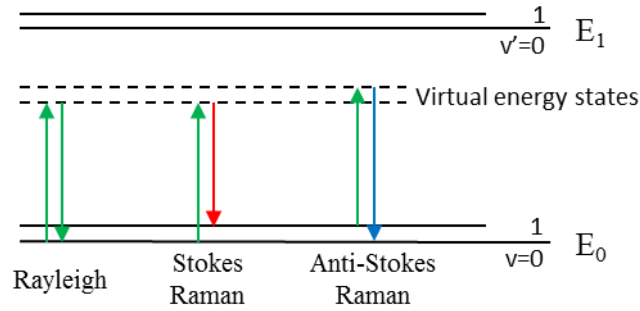


**Figure 2.13 The energy levels of a diatomic molecule**

To illustrate, Figure 2.13 schematically shows the energy levels of a diatomic molecule and the normal Raman spectra which include Rayleigh scattering, Stokes Raman scattering, and anti-Stokes Raman scattering. When a monochromatic laser beam ( $\nu_0$ ) enters the sample, it is absorbed or scattered by the sample. Most scattering is Rayleigh scattering, which is elastic with the frequency of the scattered light as the same as frequency of the incident light ( $\nu_0$ ). A small fraction of the incident light is inelastically scattered by the molecules and is thus subject to energy transfer. Stokes Raman scattering takes place when the photon excites the molecule to a higher level and the energy of the scattered photon is red-shifted ( $\nu_0 - \nu_m$ ). When the photon excites the molecule to lower level and the energy of photon is blue-shifted ( $\nu_0 + \nu_m$ ), Anti-Stokes Raman scattering occurs. Raman spectrum measures the intensity of the inelastically scattered light versus the vibrational frequency ( $\nu_m$ ) shifted from the incident light frequency ( $\nu_0$ ) after scattering.

In the classical theory, to describe Raman scattering process [149], one writes the electric field strength ( $E$ ) of the incident laser beam as:

$$E = E_0 \cos 2\pi\nu_0 t,$$

where  $E_0$  is the amplitude of electric field and  $t$  is time.

The electric dipole moment  $P$  of a diatomic molecule is written as

$$P = \alpha E = \alpha E_0 \cos 2\pi\nu_0 t,$$

where  $\alpha$  is the polarizability. When the amplitude of vibration is small,

$$\alpha = \alpha_0 + \left(\frac{\partial\alpha}{\partial q}\right)_0 q_0,$$

where  $q_0$  is the vibrational amplitude

The nuclear displacement can be shown as:

$$q = q_0 \cos 2\pi\nu_m t$$

By combining those equations, we can see

$$P = \alpha E_0 \cos 2\pi\nu_0 t$$

$$P = \alpha_0 E_0 \cos 2\pi\nu_0 t + \left(\frac{\partial\alpha}{\partial q}\right)_0 q_0 E_0 \cos 2\pi\nu_0 t$$

$$P = \alpha_0 E_0 \cos 2\pi\nu_0 t + \left(\frac{\partial\alpha}{\partial q}\right)_0 q_0 E_0 \cos 2\pi\nu_0 t \cdot \cos 2\pi\nu_m t$$

$$P = \alpha_0 E_0 \cos 2\pi\nu_0 t + \frac{1}{2} \left(\frac{\partial\alpha}{\partial q}\right)_0 q_0 E_0 \{ \cos[2\pi(\nu_0 + \nu_m)t] \cdot \cos[2\pi(\nu_0 - \nu_m)t] \}$$

So the first term corresponds Rayleigh scattering, and the second term represents anti-Stokes ( $\nu_0 + \nu_m$ ) and Stokes Raman scattering ( $\nu_0 - \nu_m$ ).

Raman spectroscopy has played an important role in the study of the  $sp^2$  nano-carbon materials, such as CNTs and graphenes. Elastic constants, edge structure, crystalline size, optical energy gap, doping, defects, strain, number of graphene layers, and diameter of nanotube can be evaluated by Raman spectroscopy.

Fundamentals of Raman spectroscopy can be explained by using solid state physics. Vibrations in any crystalline solids can be seen as the superposition of plane

waves called the normal modes of vibration. The vibration of these modes are quantized as phonons ( $Q = Q_0 \cos(2\pi\omega_{\text{vib}}t)$ ), which has linear relationship with bond lengths and angles. Their wavevectors are shown in reciprocal space called the Brillouin zone. Those modes with in-phase oscillations of adjacent atoms are called acoustic vibrations (A) and modes with out-of-phase oscillations of adjacent atoms are called optical vibrations (O) which usually have higher energy than acoustic vibrations (Figure 2.14). These vibration modes can also be classified as out-of-plane modes (o) which are perpendicular to graphene plane or in-plane modes (i) which exist in plane of graphene. Besides, the phonon vibration modes are divided as longitudinal (L) which is parallel to A-B carbons bond and transverse (T) according to vibrations perpendicular to A-B carbon bond

The unit cell of graphene contains two carbon atoms, A and B. In accordance there are six phonon dispersion modes (Figure 2.15) which are iLO, iT0, oTO, iLA, iTA, and oTA along the  $\Gamma\text{M}$  and  $\Gamma\text{K}$  directions.

The in-plane optical modes corresponding to single phonon process near the  $\Gamma$  point. The phonon vibration modes near the K point are very important since these modes are related to the Raman D-band and  $G'$ -band.

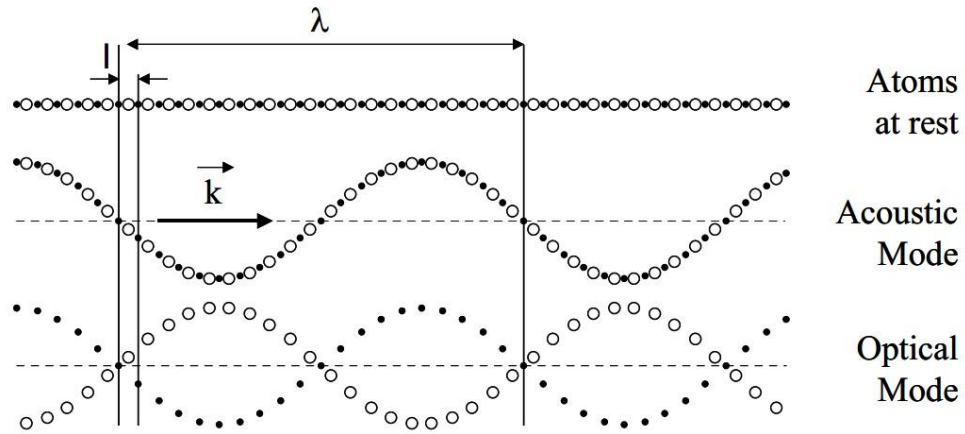


Figure 2.14 The transverse phonons in a 1D solid [150].

For the nano-carbons, there are some special features containing the single phonon G-band which is common to the  $sp^2$  carbon bonds, the radial breathing mode (RBM) which depends on the diameter and the optical transition energy, and the double phonon resonance features such as the disorder-induced D-band showing the defects level and dispersive  $G'$ -band providing the electronic and geometrical structure information.

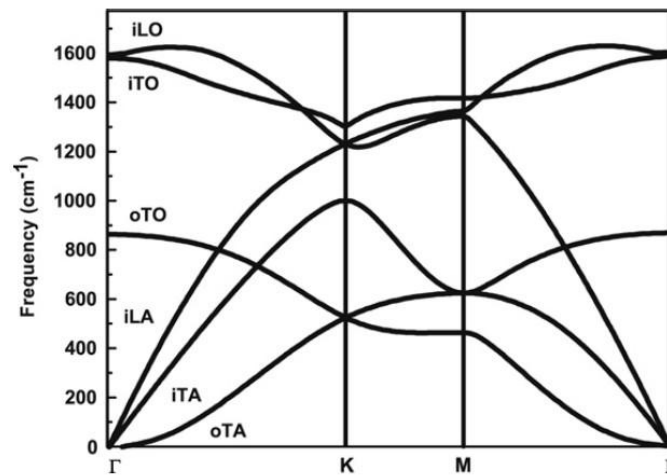
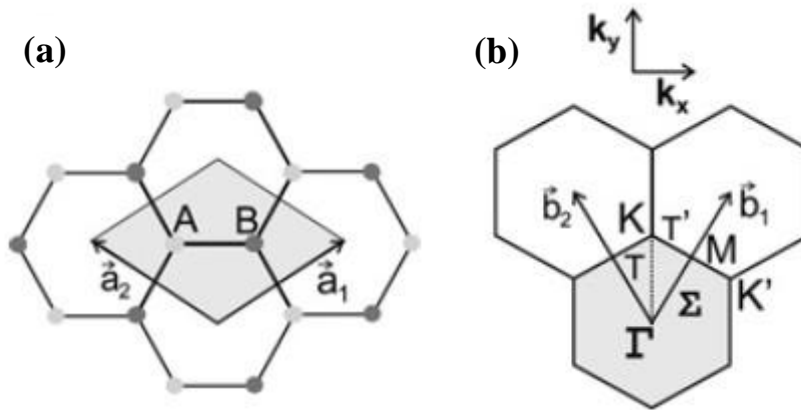


Figure 2.15 The calculated phonon dispersion relation of graphene showing the iLO, iTO, oTO, iLA and oTA phonon branches [151].

The ideal  $sp^2$  nano-carbons like CNT and graphene can be seen as a single monolayer graphene sheet including two atoms A and B per unit cell in Figure 2.16(a). The distance between the two carbons is  $a_{c-c} = 0.142 \text{ nm}$ .

Figure 2.16(b) shows the reciprocal space which is rotated 90 degree from the real space and it shows some important points of high symmetry in the first Brillouin zone for graphene: the  $\Gamma$  point at the zone center, the middle point M of hexagonal side, and corner points K and K'.



**Figure 2.16 (a) The shadowed area is a real-space unit cell of graphene showing the inequivalent atoms A and B and unit the vectors  $a_1$  and  $a_2$ ; (b) the shadowed area is a reciprocal-space unit cell showing the 1<sup>st</sup> Brillouin zone [151].**

The main special features for nano-carbon materials are listed below:

The Radial Breathing Mode (RBM)

The radial breathing mode for CNTs, which usually appear between  $100 \text{ cm}^{-1}$  to  $500 \text{ cm}^{-1}$ , can be used to determine the diameter of the nanotube. Such vibrations are

radial. Many authors fit the experimental data with  $\omega_{\text{RBM}} = A/d_t + B$ , where constants A and B are determined experimentally. The relationship between the RBM frequency and the tube diameter is widely accepted by different groups, whereas the values of A and B are slightly different and depend on the specific nanotubes as well as the tube environment. The RBM also can be used to study the optical transition energy of the nanotube.

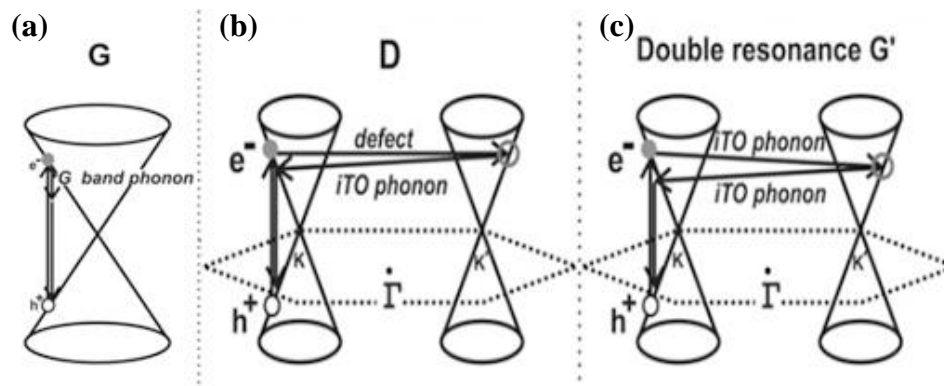


**Figure 2.17** (a) First order G band; (b) one phonon second order D band; (c) two phonon second order G' band [151]

### The G-band

The G-band, which is the only band coming from single phonon process, is related to the doubly degenerate (iTO and iLO) phonon mode at the Brillouin zone center.  $\Gamma$ . The G-band is common to all the  $sp^2$  carbon materials because it is originated from the relative vibration of neighboring carbon atoms. It is similar for graphene and nanotubes. The G-band is highly sensitive to strain because the strain can modify the bond length and the angles and, thus, it can probe any modification to the flat geometric structure of

graphene. For SWNTs, it can be observed between  $1500 \sim 1605 \text{ cm}^{-1}$ . Up to 6 G-band phonons are Raman allowed and two of those dominate the G-band spectrum:  $G^+$ , which reveals the atomic vibration along the tube axis, and  $G^-$ , which shows the atomic vibration along the circumferential direction. A G-band single peak is observed for the 2D graphene.

### The Disorder-Induced D-Band and Dispersive $G'$ - Band

The D-band and  $G'$ -band are originated from double resonance processes (Figure 2.17). For the D-band, the double resonance process starts with activating an electron by a photon of the induced laser with wave-vector  $\mathbf{k}$ . The electron is inelastically scattered to a point very close to  $\mathbf{k}'$  point by a defect (Figure 2.17(b)) or phonon with wave-vector  $\mathbf{q}$  and energy  $E_{\text{phonon}}$  (Figure 2.17(c)), and then is scattered back to a  $\mathbf{k}$  state and emits a photon by recombining with a hole. If this process includes one elastic scattering by defects and one inelastic scattering by emitting or absorbing a phonon, it is D-band process. For the  $G'$ -band, two inelastic scatterings and two phonons are involved,.

The D-band can be observed in the  $1250\text{-}1450 \text{ cm}^{-1}$  region and it is most sensitive to characterize the disorder in the  $sp^2$  bonds. The intensity ratio between the D-band and the G-band is usually used to quantify the disorder in nano-carbons. The  $G'$ -band appears in the range  $2500 - 2800 \text{ cm}^{-1}$  and it is a second-order two-phonon process and it depends strongly on the excitation laser frequency. Because the  $G'$ -band depends on any perturbation to the electronic and photon structure, it provides a very sensitive probe to

differentiate single layer and many layer graphene and to characterize the electronic structures of CNTs.

### 2.5.2 Introduction to X-ray Photoelectron Spectroscopy

The X-ray photoelectron spectroscopy (XPS) was developed in 1967 by Siegbahn at the University of Uppsala and can be used to investigate different chemical elements under ultra-high vacuum [152]. Because the photoelectron can penetrate through a limited depth of only several nanometers, namely, only few layers of atoms, XPS is a surface analysis tool.

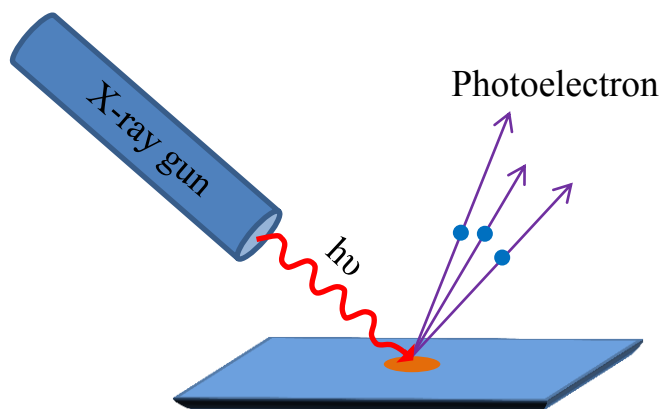


**Figure 2.18** A schematic process image of the X-ray photoelectron spectroscopy

Figure 2.18 depicts the process of XPS. Frequently, the X-ray photons are first ejected from an Al-K $\alpha$  (1486.6 eV) or Mg-K $\alpha$  (1253.6 eV) source in the X-ray gun. The X-ray from X-ray gun is directed into the sample. When an X-ray photon is absorbed by an atom, one of its core electrons is ejected with a certain kinetic energy, producing a photoelectron. When this occurs, another electron in a higher energy state jumps into the vacant inner core state, while releasing energy to another electron which becomes a free

electron (Auger electron) (Figure 2.19). The ejected electrons, including photoelectrons and Auger electrons, are collected and their kinetic energy (KE) are measured to calculate the binding energy (BE) of the inner core electron by using following equation.

$$BE = h\nu - KE - \Phi,$$

where  $\nu$  is the frequency of the incident X-ray photon and  $\Phi$  is a correction factor which depends on the spectrometer system.

By analyzing the XPS spectrum, one can derive the different types and the chemical states of chemical elements by fitting binding energy peaks. The chemical composition of the sample may be obtained by fitting the XPS spectrum with the known binding energy peaks. In such fittings, the atomic sensitivity factors (ASF) for each element must also be taken into consideration.

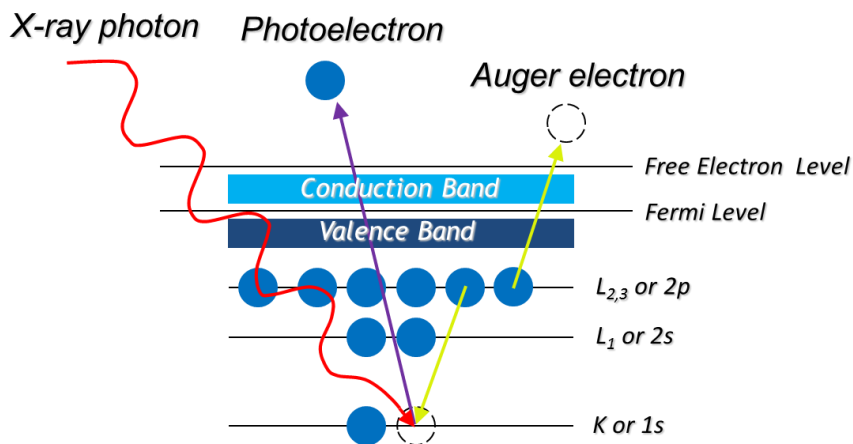


**Figure 2.19** The schematic diagram of the photoelectric process (purple) and the Auger process (yellow).

Previously, XPS was used to investigate the carbon bonds in CNT and graphene. Lee et al found that the binding energy of the  $sp^2$  carbon,  $sp^3$  carbon, and oxygen atoms were 284.3, 285, and 288.5 eV, respectively [153]. Another study from Chen's group

used XPS to study the difference between the carbon bonds in CNT and in graphene. Their study showed that CNT has weaker C-C bonds than graphene [154]. Besides, some other groups like Droppa used XPS to study the structure modification of CNT. C1s was shown to have a binding energy shift and an asymmetric broadening [155]. Investigation of the mechanisms of formation of nano-carbon/polymer interface was done using XPS in this dissertation.

## **2.6 Stress sensitivity of polymer nanocomposites using Raman spectroscopy**

The interface between the reinforcement and the polymer matrix has the key effect on the load stress transfer via shear stress. The weaker the interfacial shear strength of composites, the lower load it can withstand before the interface fails. Poor interfacial bonding behaves like defect centers. Thus, strong interfacial bonding is required to achieve high mechanical strength for composites [156].

Raman spectroscopy can be used to study the interatomic bonding and to characterize the load transfer in composites. For example, Raman spectral shift has been used to study carbon and silicon carbide fibers under stress in composites [157, 158]. Ajayan *et al.* used Raman spectroscopy to study the load transfer in an MWNT/epoxy system [19]. The enhanced shift in the Raman G' band during compression was related to the higher interfacial shear stress and the higher load transfer to the nanotubes [19].

The previous Raman study in this area also probed the interfacial stress transfer in graphene monolayer nanocomposite [159]. Graphene monolayer was placed in between a layer of PMMA and SU8. The G'- band showed the change linearly up to ~0.4% strain,

and demonstrated the potential of using graphene as reinforcements in composites. More recently, Raman spectroscopy was used to study the load transfer for the composites with few-layered-graphene consisting of GNPs dispersed in PDMS. Under tensile loading, the platelets underwent compression as indicated by the upshift of Raman peaks. Similarly, under compressive loading, the platelets underwent tension as indicated by the downshift of the Raman peaks [34].

The Raman sensitivity to the stress change arises from the anharmonicity of the atomic bonds of reinforcements (Figure 2.20) [150]. As long as the elongation is limited, the bond can be modeled by a spring of length  $L$ , reduced mass  $\mu$ , speed of light  $c$ , constant stiffness  $k$ , wavenumber is  $\bar{w}$

$$\bar{w} = \frac{1}{2\pi c} \sqrt{\frac{k}{\mu}}$$

$$k = \frac{\partial^2 V}{\partial L^2}$$

Bond energy  $V(L)$  can be described below by an anharmonic atom bond model (Figure 2.20):

$$V(L) = V_0 + V_{attractive}(L) + V_{repulsive}(L)$$

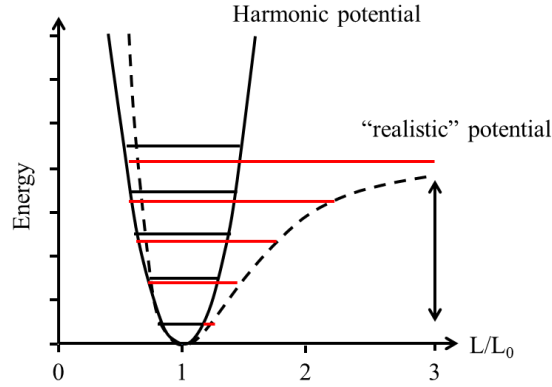


**Figure 2.20** A comparison of the “realistic” and the harmonic bond potentials [150]

By using the interatomic potentials of the harmonic bond model and including the attractive and repulsive contributions as shown in the above equation (Mie and Gruneisen parameters  $A, R, a, r$ ), the energy of the anharmonic bonds can be expressed as:

$$V(L) = V_0 - A \times L^{-a} + R \times L^{-r}$$

By using the “quasi-harmonic” approximation, the above equation is equivalent to:

$$\frac{d\bar{w}}{\bar{w}_0} = \frac{dk}{2k} = \frac{1}{2} \frac{a(a+1)(a+2)A \times L^{-(a+3)} - r(r+1)(r+2)R \times L^{-(r+3)}}{r(r+1)R \times L^{-(r+2)} - a(a+1)A \times L^{-(a+2)}} dL$$

By introducing the bond elongation  $\varepsilon_L = (L - L_0)/L$  (small strain assumption), one can derive

$$\begin{aligned} \frac{d\bar{w}}{\bar{w}_0} &= -\frac{(a+r+3)}{2} \times \varepsilon_L \\ \bar{w} &= \bar{w}_0 \left[ 1 - \left( \frac{a+r+3}{2} \right) \times \varepsilon_L \right] \\ \Delta\bar{w} &= -\left( \frac{a+r+3}{2} \right) \times \varepsilon_L \\ \Delta\bar{w} &= -R(a, r) \times \varepsilon_L, \end{aligned}$$

$R(a, r)$  is a constant which depends on the bonding type. Therefore, there is a direct proportionality between the Raman shift and the bond deformation. Under the same strain, larger wavenumber change of the Raman peak reveals larger bond length deformation.

From the above equations, we can then derive the interfacial stress which, can be seen, has the same effect of a normal stress, inducing a normal strain  $\varepsilon_L$  :

$$\Delta\sigma = E_f \varepsilon_L = -\frac{E_f \cdot \overline{\Delta w}}{R(a, r)},$$

where  $E_f$  is the Young's modulus of the filler.

Therefore, the strain induced Raman band shifts is a measure of the change in interatomic distances or bond deformation due to the load transferred from the polymer to the graphene fillers. Because the eventual mechanical properties of the composites inevitably depend on the extent to which the load is transferred from the polymer to the graphene filler, the graphene/polymer interface should play the most important role in efficient load transfer.

## CHAPTER 3 NIR PHOTON-ASSISTED POLYMERIZATION OF CARBON NANOTUBE/POLYMER COMPOSITES

### 3.1 Introduction

One of the important applications of CNTs is their use as nanoscale fillers to improve the mechanical properties of polymeric materials. The high aspect ratio, Young's modulus, and tensile strength of CNTs make them attractive as nanoscale fillers to enable increased load transfer and improved mechanical strength of polymer nanocomposites. The nanotube/polymer interface has been demonstrated to play an important role in efficient stress transfer to the nanotube and determination of overall nanotube/polymeric composite mechanical properties [160]. Ajayan *et al.*, measured the load transfer in a MWNT/epoxy system using Raman spectroscopy [19]. The enhanced shift in Raman G' mode during compression demonstrated higher interfacial shear stress and load transfer to the nanotubes [19]. Later, numerous reports have demonstrated enhanced load transfer to nanotubes utilizing strategies such as surface functionalization of nanotubes [20-22], refluxing CNTs with nitric acid to create carboxyl, carbonyl and hydroxyl groups [23, 24], sidewall functionalization for better dispersion of nanotubes in the matrix [25], alignment of nanotubes in the matrix [26], in-situ melting and polymerization [27, 28], melt compounding [29], and more recently using flexible

spacers at the nanotube/polymer interface [30]. The work by Zhang *et al.*, is notable in that it achieved an impressive Young's modulus increase of ~214% for adding just 2 wt. % of MWNTs in a polymer matrix [29].

SWNTs and MWNTs have been known to absorb significant amounts of NIR light, resulting in photo-thermal heating [47]. Applications of such nanoscale photo-thermal heating include bio-nanotechnology to kill cancer cells [47, 49], targeted drug delivery [50], photo-mechanical actuators [51], and laser assisted photo-thermal imprinting in polymeric materials [52]. Irradiation of nanotube/polymer composites by NIR during crosslinking could potentially result in significant heating of nanotubes inside the polymer, thus enhancing the crosslinking process and strengthening the nanotube/polymer interface. This is a paradigm in polymerization of the samples by enabling crosslinking to start at the nanotube/polymer interface using photo-thermal heating of nanotubes. This type of polymerization and strengthening is not possible using oven based heating methods as heat flows into the sample from the outside. We compare the load transfer and Young's modulus of our NIR light treated samples with that of a sample by the conventional crosslinking method with oven baking to 125 °C for 30 m.

### **3.2 Results and discussions**

Samples containing various fractions (0.01-1 wt. %) of MWNTs in PDMS were synthesized by conventional baking method and NIR photon-assisted polymerization in Figure 3.1, and those samples are studied by SEM, Raman spectroscopy, mechanical test system (See details in Appendix A).

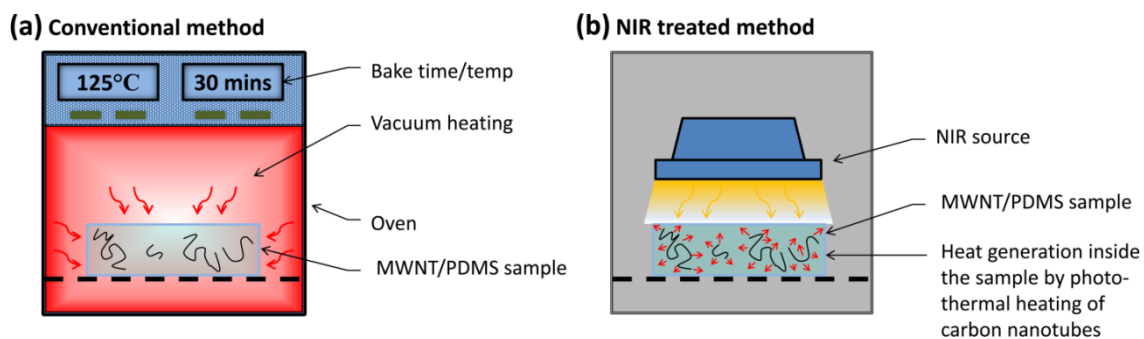


**Figure 3.1 Schematic of the two different polymerization techniques: (a) oven based heating; (b) NIR light treatment.**

### 3.2.1 Characterization of MWNT/PDMS composites

Figure 3.2(a) presents the cross-sectional SEM images of the nanotube/polymer interface for various weight fractions of MWNTs (0.01-1 wt. %) in PDMS. Raman spectra for both the pure PDMS and the MWNT/PDMS composites are presented in Figure 3.2(b).

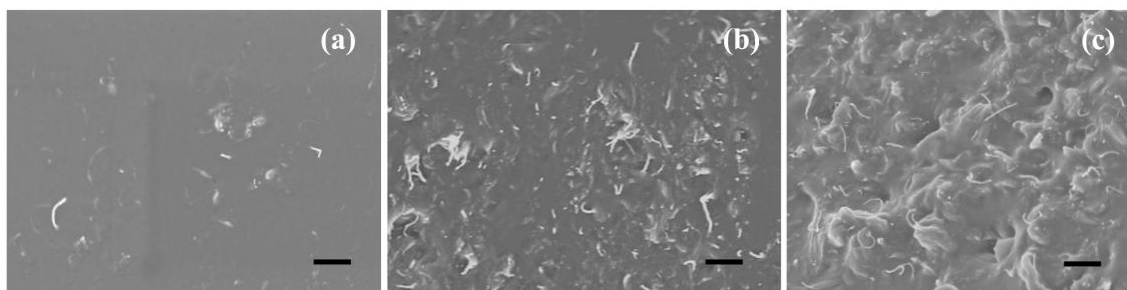


**Figure 3.2 SEM images of the MWNT/PDMS samples, scale bar 500 nm; (a) 0.01 wt. %; (b) 0.1 wt. %; (c) 1 wt. % of MWNT.**

The SEM images clearly show dispersion of MWNTs with increasing nanotube density with increasing the wt. % of MWNT. In all the three SEM images, one end of the MWNT was stretched out of the matrix while the other end was embedded firmly in the

matrix. This is indicative of strong interfacial adhesion between the nanotubes and the PDMS/polymer [29].

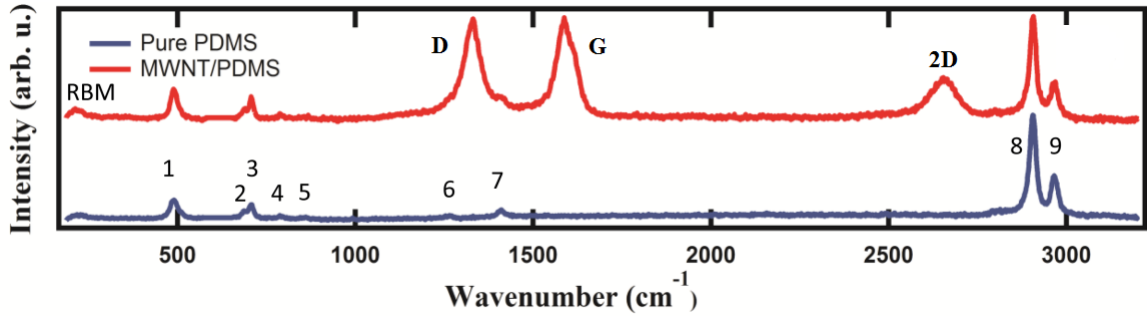


**Figure 3.3 Raman spectra of the pure PDMS and the 1 wt. % MWNT/PDMS sample.**

The SEM images of both the oven baked samples and the NIR photon irradiated samples qualitatively exhibited the similar results. In the Raman spectra of Figure 3.3, one can see all the nine peaks associated with the PDMS in both the samples. The RBM mode (219.3 cm<sup>-1</sup>), the disorder induced D band (1328 cm<sup>-1</sup>) tangential mode G band (1588 cm<sup>-1</sup>) and 2D or G' (2657 cm<sup>-1</sup>) bands of the MWNT are clearly seen in the nanotube/polymer sample, demonstrating high purity of sample preparation, subsequent crosslinking, and polymerization methods.

### 3.2.2 Raman-strain sensitivity study of MWNT/PDMS composites

Raman spectroscopy has been used by many groups in the past to measure the strains in nanoscale fillers such as CNTs [19, 161-168]. When a strain is applied, interatomic distances change resulting in a shift in the vibrational frequencies. The G' band near 2700

$\text{cm}^{-1}$  in the Raman spectra for MWNTs is highly sensitive to strain. The larger shift in the G' band peak position is indicative of a larger load carried by nanotubes. Since the SEM images and Raman signatures of the samples look qualitatively similar before applying strain, characterizing wavenumber shift in G' peak in both the samples indicates strength of the nanotube/polymer interface in both of these samples. Figure 3.4 presents the shift in Raman peak position of the G' band for both oven polymerized (Figure 3.4(a-1)) and NIR light polymerized 1 wt. % MWNT/PDMS samples (Figure 3.4(b-1)) as a function of applied tensile strain. It is clear that oven polymerized samples have a smaller shift to the left in the Raman peak position compared to NIR light treated samples.

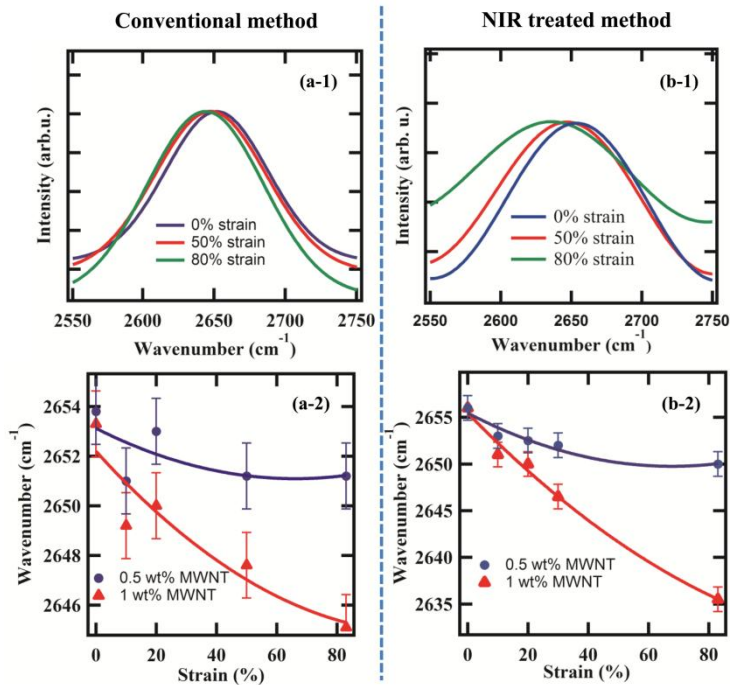


**Figure 3.4** Load transfer in the conventional (a-1) and NIR light polymerized samples (b-1); the change in the wavenumber is displayed as a function of the percentage strain for the conventional (a-2) and NIR light polymerized samples (b-2).

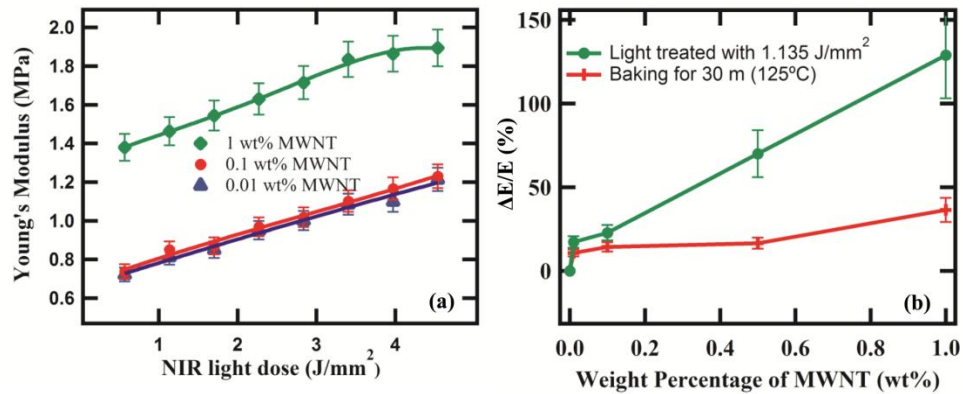
There are several interesting characteristics in the Raman spectra as a function of applied strains. For both conventional and NIR photon irradiated methods, at 0% strain, Raman signatures look identical (blue line). As we increase the strain to ~50%, oven baked samples undergo only a small shift to the left (red line, Figure 3.4(a-1)), while NIR light treated method undergoes much larger shift (red line, Figure 3.4(b-1)). The shift in Raman peak position at ~ 80% strain is even more predominant for NIR photon polymerized samples (green line). It is clear from Figure 3.4(a-1 & b-1) that higher load transfer to the nanotubes occurred in samples treated with NIR light compared to oven polymerized samples. This may indicate better crosslinking and polymerization of the nanotube/polymer interface.

Figure 3.4(a-2 & b-2) presents the change in wavenumbers as a function of strain. For both oven baked samples and NIR light treated samples, there is a decrease in G' mode wavenumbers for 0.5 wt. % and 1 wt. % MWNT/polymer samples. For the oven baked method, there was 3 cm<sup>-1</sup> change in wavenumber for 0.5 wt. % and 9 cm<sup>-1</sup> change in wavenumber for 1 wt. % MWNT/polymer composites for the strain values tested. On the other hand, there was 5 cm<sup>-1</sup> change in wavenumber for 0.5 wt. % and 20 cm<sup>-1</sup> change in wavenumber for 1 wt. % MWNT/polymer composites for the NIR light treated method at strains from 0-80%. Samples strained >80% lead to complete failure.

The past reports on Raman spectroscopy for investigating load transfer on nanotube/polymer composites have only been done in a limited range ( $\pm 15\%$  strains) before sample failure [19, 169]. Higher strains used here and larger shifts in the Raman positions (up to  $\sim 20$  cm<sup>-1</sup> wavenumbers) show the greater load transfer to the nanotubes than the past reports. It should be noted that for  $\sim 0.5$  wt. % MWNT/polymer samples the

wavenumber shift saturates beyond ~40%. There is no appreciable change in wavenumbers at 80% strain, and thus strains are not resolvable beyond ~40%. This is true for both types of samples, suggesting that saturation of the Raman signal is related to weight fraction of nanotubes in the polymer matrix or number of nanotube/polymer sites that undergo strain. This may be related to the percolation threshold (PT) and requires further exploration. As nanotube wt. % increases in the matrix, not only is there significant increase in load sharing but samples below and above the PT should exhibit different Raman shifts. From our past experience, the PT of nanotube/PDMS composites is ~0.5 wt. % [170]. Therefore at 1 wt. %, above the PT, load is shared more uniformly and the interpenetrating network of nanotubes in the polymer matrix makes wavenumber shifts resolvable at higher strains.

### 3.2.3 Mechanical properties of MWNT/PDMS composites



**Figure 3.5 (a) Young's modulus versus NIR light dose for MWNT/PDMS fractions; (b) change in Young's modulus versus weight percentage of MWNT for light treated and oven baked methods.**

Figure 3.5(a) presents Young's modulus as a function of NIR energy dose with increasing fraction of MWNTs in polymer composites. For small fractions (0.01-0.1 wt. %) of MWNTs in PDMS, there is only a small change in Young's modulus values and both curves look similar. However, at ~1 wt. % MWNTs, Young's modulus values increase by roughly twice for all NIR dose energy levels. This suggests that as NIR dose is increased and with more CNTs in the matrix, significant strengthening occurs. This can only happen if nanotubes are heating the polymer and strengthening the interface. Figure 3.5(b) compares the change in Young's modulus as a percentage for both samples. It is clear that for all wt. % MWNTs, change in Young's modulus is higher for NIR treated samples compared to the oven polymerized samples. A ~36% increase in Young's modulus at 1 wt. % MWNTs was observed for oven polymerized samples versus ~130% increase in Young's modulus for the same wt. % of MWNTs for NIR light polymerized samples.

These impressive results suggest that irradiating samples with NIR light caused nanotubes to heat inside the polymer, thereby resulting in enhanced crosslinking and polymerization of the nanotube/polymer interface leading to better mechanical properties and increased load transfer. Macroscopic temperature rise was measured to be ~75 °C for NIR photon irradiated samples. However, actual temperature rise at the nanotube/polymer interface must be much higher than this value to enable such exceptional strength and load transfer. As the nanotubes are well dispersed and with increase in weight fraction of MWNTs in the polymer, each nanotube/polymer interface must undergo significant heating and therefore improved the overall load transfer to the nanotubes thereby enabling higher mechanical strength. Materials such as CNTs or

graphene can heat up and cool rapidly (within micro to nano-seconds) and therefore future time resolved studies at the nanotube/polymer interface can capture the actual fast thermal events that resulted in such exceptional strength of the nanotube/polymer interface.

### **3.3 Conclusion**

In summary, we demonstrate photon assisted heating of MWNTs inside a polymer matrix that resulted in better polymerization of the nanotube/polymer interface. Dramatic enhancement in the load transfer to the embedded nanotubes and the subsequent increase in Young's modulus were observed. Compared to traditional polymerization techniques, NIR method yielded an increase in the Young's modulus value of ~130% for adding just 1 wt. % MWNT in PDMS polymer. Such an increase is greater than the most reported values to date. Raman spectroscopy suggested shift in wavenumbers of  $\sim 20 \text{ cm}^{-1}$  for ~80% strain, larger than the most past reported values. These results suggest NIR light-induced heating of CNTs at the nanoscale could potentially be used as a scalable nanomanufacturing technique for increased load transfer and higher mechanical strength for reinforced polymer composites.

Looking forward into variety of applications, NIR heating of nanotubes in polymers could be used as a fundamental technique to enable large scale cross-linking and enhanced mechanical properties of nano-composite materials in general. The method reported here could be useful in improving the interfacial shear strength and mechanical properties of emerging class of light weight and high strength nanocomposites based on

graphene. While surface chemical functionalization of nanotubes/graphene are quite attractive, recent reports have shown that improvement in interfacial adhesion due to surface functionalization of nanotubes does not always promote substantial improvement in mechanical properties [171]. This is due to surface degradation of nanotubes/graphene during functionalization. Compared to these techniques, the use of NIR light is benign and can render high strength nanocomposites as reported here. The structural properties of nanotubes should remain unaffected for both the process. What is being changed is the heat flow. In the conventional process, the heat flows from the outside to the insides of the sample. Depending on the heat transfer rate in the polymer and the thermal conductivity of the filler, one can find localized cold and hot spots that can affect cross-linking process and eventual mechanical properties. On the other hand, in the NIR method, exciting the nanotubes to high temperature, each and every nanotube in the matrix should participate in the heating process. As a result, the matrix is crosslinked around the nanotube more uniformly that resulted in higher load transfer as suggested by Raman spectroscopy. Since the structural properties remain unaffected so should the electron transport properties of the composites.

On a more practical note, nanotubes/graphene functionalized with sulphur and followed by NIR treatment as reported here can enable nano- to macroscopic scale vulcanization of rubber materials that is of significant use to many day to day applications worldwide. Other applications of nanotube-polymer composites could be envisioned in aerospace structures, reinforced laminates, high strength plastics, wear resistant and bullet proof textiles, and electrical cables. All these applications could

benefit the NIR method reported here for enhanced cross-linking that can result in significant load bearing and mechanical strength without damaging the nanotubes.

## CHAPTER 4 NIR PHOTON-ASSISTED POLYMERIZATION OF GRAPHENE/POLYMER COMPOSITES

### 4.1 Introduction

While in the previous chapter, the novel NIR polymerization technique was demonstrated as a practical way for developing nanotube composites, in this chapter, the investigations in graphene/polymer composites for higher load transfer and improved mechanical properties is discussed. Like CNTs, graphitic nano-carbons can also be used as nanoscale fillers to enhance the load transfer and improve the mechanical properties of polymeric materials. The isolation of single layer graphene achieved in 2004 has rejuvenated the research in the area of graphitic nano-carbons. Defect free sheets of SLG, exfoliated mechanically from graphite flakes, was measured to have a second order elastic stiffness of 340 N/m, a breaking strength of 42 N/m, and a Young's modulus of 1.0 TPa [95]. Such excellent mechanical properties of the exfoliated SLG spurred investigation of using it as nanoscale fillers in advanced polymer composites. Recently, the interfacial stress transfer of exfoliated SLG, after transferred on the top of polymer substrate, was demonstrated using Raman spectroscopy [32, 33]. Significant shift in the Raman G' and 2D bands ( $> -50 \text{ cm}^{-1}/\%$  strain) were observed, demonstrating load transfer to the SLG [32, 33]. Several studies on exfoliated graphite based polymer composites have shown enhanced mechanical strength, toughness, glass transition

temperature and increase in electrical conductivity and gas barrier properties [36-43]. The work by Coleman *et al.*, is notable as it yielded an increase of ~100 times in Young's modulus at 3% strain for samples with 50 wt. % exfoliated graphene drop casted in polyurethane [43]. While these studies are impressive reiterating the importance of graphene as filler materials in polymer composites, the current methods of fabricating advanced polymer composites using mechanically exfoliated graphene face a huge challenge. This is due to the fact that at present the yield of mechanically exfoliated graphene is limited to 1 wt. % which could be further increased to 7-12% with some additional processing [44]. In this context, the use of chemically reduced graphene as fillers in polymer composites becomes important and warrants investigation for development of low cost and high strength advanced composites. Graphene sheets chemically derived from GO using Hummer's method and subsequent reduction by hydrogen plasma has been heralded as one of the methods for large scale production of the graphene suitable for industrial use [45]. Microscopic characterization of such graphene sheets has shown large unoxidized graphitic regions in between defective clusters and therefore could witness interesting mechanical properties [46]. Recent studies have shown that despite the defects in their lattice, such sheets have shown extraordinary stiffness with Young's modulus  $E=0.25$  TPa, approaching that of pristine graphene, with high flexibility and lower built-in tension [45]. Therefore, studying the interfacial load transfer and mechanical properties of reduced graphene sheets in polymers can make progress in the area of low cost, high strength and scalable composites by using graphene.

Over the past years Raman spectroscopy has become a powerful tool to understand the interfacial load transfer in carbon fibers and nano-carbon fillers such as CNTs in polymer composites [19, 172]. The disorder induced 2D bands and tangential mode G band has been demonstrated to be sensitive to both the compressive and tensile strains in nano-carbon fillers such as CNTs [19, 172]. The Raman stress sensitivity arises from the anharmonicity of the atomic bonds [150]. By using the interatomic potentials of the harmonic bond model and including the attractive and repulsive contributions (Mie and Gruneisen parameters), the previous theoretical work has demonstrated a direct relationship between the wavenumber shift in the Raman bands and the bond deformation

that can be expressed mathematically as:  $\bar{w} = \bar{w}_0 \left[ 1 - \left( \frac{a+r+3}{2} \right) \times \varepsilon_L \right]$ , where  $a$  and  $r$  are positive constants depending on the bond type and  $\varepsilon_L$  is the applied strain [150].

Therefore, the strain induced Raman band shifts can be used to measure the change in the interatomic distances or the bond deformation due to the load transferred from the polymer to the graphene fillers. The ultimate mechanical properties of the composites inevitably depend on the extent to which the load is transferred from the polymer to the graphene filler and the graphene/polymer interface should play the most important role in the efficient stress transfer. Therefore, large shift in Raman wavenumbers signals high stress transfer from the polymer to the graphene fillers. This relationship can be

mathematically expressed using the following equation:  $\Delta\sigma = E_f \varepsilon_L = -\frac{E_f \cdot \Delta\bar{w}}{R(a,r)}$ , where

$E_f$  is the Young's modulus of the filler material, and  $\Delta w$  the wavenumber shift. Thus, if the filler has the same bond type and assuming that the applied strain field is constant

throughout the composite matrix, a larger Raman wavenumber shift means a higher load transfer.

More recently, Raman spectroscopy was employed to measure the load transfer of the few layer graphene consisting of GNP in PDMS. Under tensile loading, the platelets went into compression corresponding to upshift of Raman wavenumbers and similarly, under compressive loading, the platelets went into tension corresponding to downshift of the Raman wavenumbers. While these initial studies were quite impressive, practical applications of graphene based composites can only be realized through similar strategies that were utilized in CNT-based composites in the past such as NIR photo-thermal heating and polymerization of nanocomposites [173], surface functionalization [146, 174-176], refluxing with nitric acid to create carboxyl, carbonyl, and hydroxyl groups, solution-based [177-180], *in-situ* melting and polymerization [181-185], and melt compounding [186-190]. However, these studies have not been conducted on graphene based nanocomposites. Here, we demonstrate load transfer and improved mechanical strength of RGO and GNP based polymer composites fabricated using *in situ* NIR photon-assisted heating of graphene and polymerization of graphene/PDMS interface. We focus on two types of graphene with differences in the number of layers to investigate how the number of layers can have a profound effect on the mechanical properties of the composites.

As discussed earlier, the photo-thermal effect in nano-carbons is through absorption of NIR photons which subsequently produces heat. For example, because the nano-scale fillers such as CNTs are quite small, the localized photo-thermal effects can be focused on a small area to kill cancer cells but without harming the neighboring

normal cells, thus achieving molecular targeting and subsequent photo-thermal ablation. Nanoscale photo-thermal heating has also found applications in targeted drug delivery, photomechanical actuators, and laser assisted photo-thermal imprinting in polymeric materials. Recently, Xu *et al.* demonstrated the photo-thermal polymerization of nanotube-polymer composites by *in situ* heating of CNTs using NIR photons. Instead of utilizing conventional baking methods in vacuum oven typically used for polymerization of samples where heat flows from the outside to the inside, the samples were irradiated with NIR photons. It was expected that NIR photons would heat the nanotubes more focusedly to high temperatures at the nanotube/polymer interface, thereby strengthening the interface. It was found that irradiation of the nanotube/polymer samples with NIR photons during cross-linking resulted in enhanced strengthening of the nanotube/polymer interface. A ~36% increase in the Young's modulus at ~1 wt. % MWNTs was observed for oven polymerized samples versus ~130% increase in Young's modulus for the same wt. % of MWNTs for NIR light polymerized samples. Raman spectroscopy showed that MWNT/polymer samples that were fabricated using NIR method underwent large shifts in its G' band from 0-80% strains ( $20\text{ cm}^{-1}$  at 1 wt. % MWNT) compared to the oven baked samples ( $9\text{ cm}^{-1}$  at 1 wt. % MWNT). This suggested the marked enhancement of the load transfer and the higher mechanical strength for nanotube/polymer composites using NIR polymerization. However, no such studies have been conducted on graphene/polymer composites. Graphene is a 2D sheet compared to nanotubes that are quasi 1D. The thermal conductivity of graphene is higher than CNTs and the phonon heat transfer can occur in both dimensions of the sheet, whereas for CNTs thermal conduction is efficient only along the axial direction. Rigid stack-like morphology and lack of inter-

plate interactions of GNPs could mean that their dispersion properties and eventual load transfer and mechanical strength could be different in polymer composites compared to their RGO counterparts. Mixing RGO in polymers could potentially result in folding, kinking, doping and defect inducement of the 2D sheet that can lead to D bands, broaden G bands and change the intensity of 2D bands. Mixing graphene sheets in polymers can result in the edges of the graphene sheet being functionalized thereby resulting in greater dispersion, enhanced stiffness, shorter polymer chain lengths and better mechanical properties. No information is available on how Raman bands evolve when different types of graphene sheets are mixed in polymeric materials. For all these reasons we have investigated the NIR photon-assisted polymerization of graphene polymer composites using Raman spectroscopy. Our results show significant shifts in G band both in tension and compression for the NIR treated method compared to the conventional oven baking methods for both GNP and RGO. Full Width Half Maximum (FWHM) data show minimum slippage for the NIR photon-assisted polymerization compared to conventional oven polymerization. A ~75% improvement in Young's modulus was achieved for the RGO/PDMS polymerized using NIR method compared to ~30% improvement for the conventional oven based polymerization. Several insights are provided as to the differences between NIR and conventional polymerization of composites, the use of GNP versus RGO and how each type of filler brings in unique characteristics. Finally, comparison is made with their CNT counterparts and how dimensionality affects the overall mechanical properties of the advanced composites. These results have significance in development of advanced polymer nanocomposites based on graphitic nanostructures.

## 4.2 Results and discussion:

Homogenous dispersion of graphene (1 wt. % of RGO and GNP for comparison) in PDMS was prepared using a shear mixing process. Samples containing 1 wt. % RGO or GNP in PDMS were synthesized by both conventional baking method and NIR photon-assisted method, and those samples are studied and tested by SEM, Raman, and mechanical test system (See experimental details in APPENDIX B).

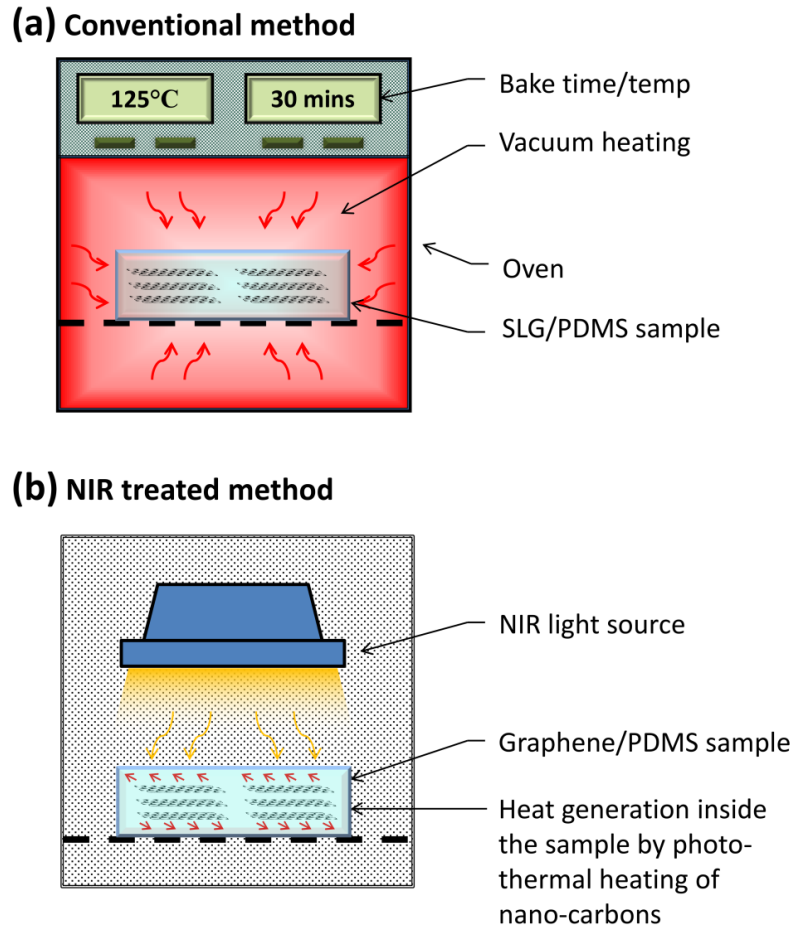


**Figure 4.1 Schematic of the two different polymerization techniques: (a) oven based heating; (b) NIR light treatment method.**

Figure 4.1(a) presents the schematic image of the conventional oven polymerization. In conventional oven curing, samples are heated in a vacuum oven at 125 °C for 30 min following addition of cross-linkers and degasing. In this type of heat treatment, heat flows from the outside to the insides of the sample. At this time and temperatures, the Young's modulus values saturate indicative of the end of the crosslinking process. Figure 4.1(b) presents the irradiation of NIR photons on the samples following addition of cross-linkers and degasing. Irradiation of NIR photons on the sample results in *in situ* heating of the graphene/polymer interface to high temperatures. This is a paradigm in polymerization of the graphene nanocomposites as it enables crosslinking to start at the graphene/polymer interface using photo-thermal heating of graphene. This is analogous to bottom up manufacturing of polymer composites.

The advantages of NIR photon-assisted polymerization of nano-carbon composites include: 1) all the nano-carbons participate in the polymerization process simultaneously by absorbing photons and converting them into heat, 2) rapid stiffening of the samples due to the entire sample being heated at the nano-scale simultaneously, 3) shorter segmental chain length resulting in higher stiffness and better values for Young's modulus 4) ability to dynamically tune the polymerization process and control over stiffness of sample using the NIR dosage, and 5) ability to create selective regions with dynamically tunable stiffness in polymers, rubbers and gels.

#### 4.2.1 Characterization of graphene and graphene/PDMS composites

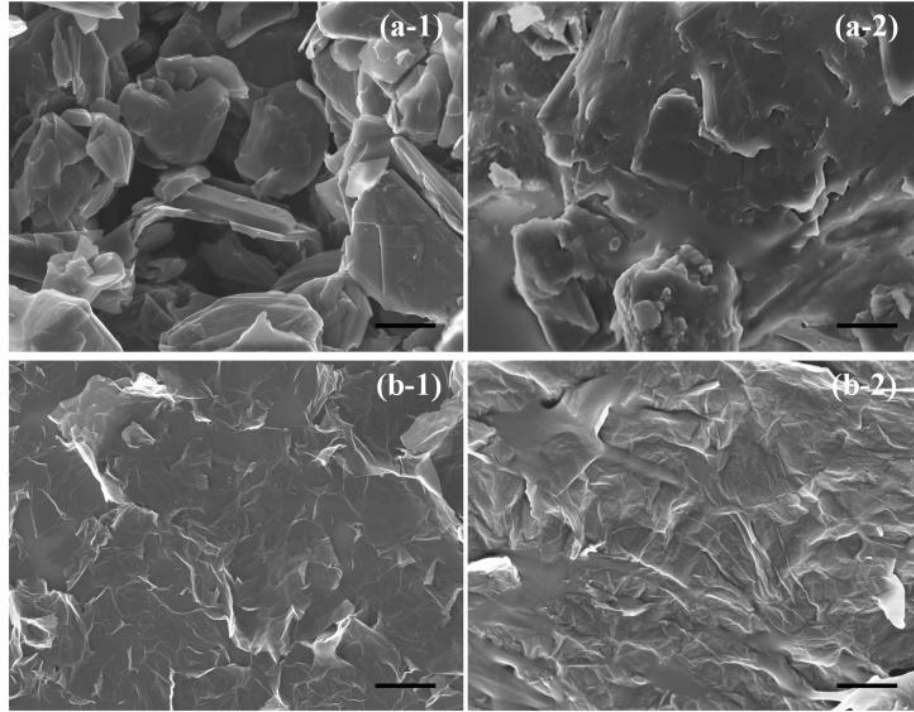


**Figure 4.2 SEM images of (a-1) GNP; (a-2) GNP/PDMS; (b-1) RGO; (b-2) RGO/PDMS**

Figure 4.2(a-1) presents an SEM image of GNPs, which are comprised of 3-5 graphitic layers [79]. Figure 4.2(a-2) presents an SEM image of GNP/PDMS composite. One can see that the rigid stack like morphology of GNP is maintained in the polymer matrix. Figure 4.2(b-1) presents an SEM of RGO. Figure 4.2(b-2) presents an SEM image of RGO/PDMS composite. GNPs show a rigid stack/plate like morphology while RGO demonstrate morphology of thin ribbon but with excellent dispersion.

Figure 4.3(a-1 & a-2) presents the fracture surface of GNP/PDMS and Figure 4.3(b-1 & b-2) presents the fracture surface of RGO/PDMS samples to investigate microscopic morphology of load transfer. Two important observations were made in the images. From the morphology of Figure 4.3(a), it looks like GNP fillers were pulled out of the PDMS matrix and fell onto the crater surface due to lack of flexibility. This is

contrasted by other areas where GNP/PDMS is seen bridging the gaps between the cracks (Figure 4.3(a-2)). These images suggest that GNPs act like reinforcers, as they assist in bridging cracks between the surfaces and aid in load transfer. However, investigations into RGO/PDMS cracks lead to different results. Most RGO (Figure 4.3(b-1)) looks similar to their polymeric composite and is still seen to bridge the crack opening.

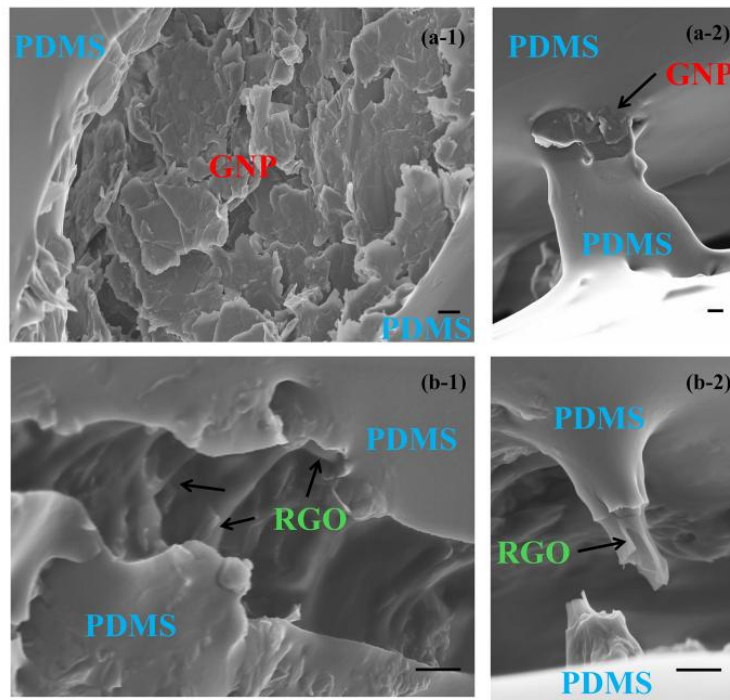


**Figure 4.3 SEM images of the cracks (a-1) collapsed GNPs on the crater of the micro-crack; (a-2) GNPs aiding load transfer; (b-1) RGO between the crack openings; (b-2) cracking of RGO filler after peeling of PDMS. Scale bar: 500 nm in all the images.**

However an interesting result that was seen was the fracture surface from other areas. Figure 4.3(b-2) presents the fractured filler inside the crack. It is clear that the layers of polymer and RGO plates are seen distinctly with the polymer pulled out of the RGO filler before complete failure of the filler. It is seen from these images that the failure

mechanisms of RGO is quite different compared to nanotubes which needs to be investigated [191]. Nanotube tends to slide between the bundles much more easily than break compared to RGO fillers as seen in these SEM images [191]. This warrants further investigation depending on the strains applied, crack widths, graphene filler aspect ratio and number of graphitic layers.

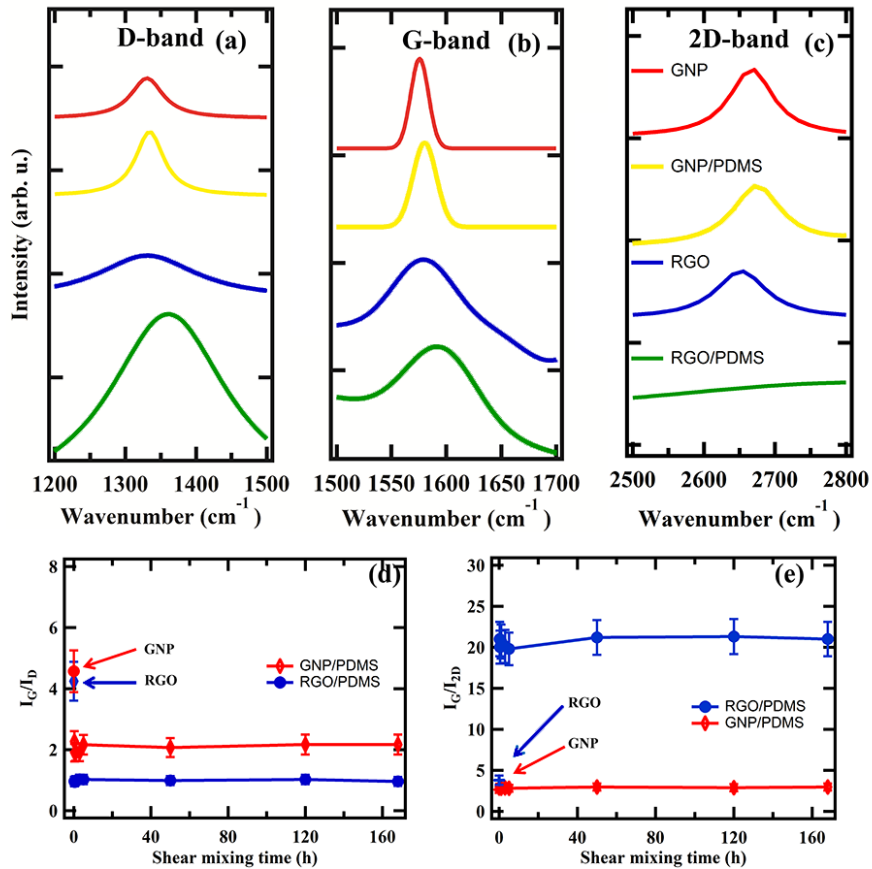


**Figure 4.4** Raman spectra of (a) D band, (b) G band, (c) 2D band of GNP, RGO, GNP/PDMS, and RGO/PDMS, (d) and (e) ratio of  $I_G/I_D$  and  $I_G/I_{2D}$  versus shear mixing time respectively

Figure 4.4 presents the evolution of the Raman D, G and 2D bands for pure GNP, RGO and their polymer counterparts as a function of the mixing process. Multilayer configuration of GNPs causes a frequency shift in both peaks as compared to RGO [192].

From the Raman bands, it is seen that both G band (Figure 4.4(b)) and the 2D band ratios (Figure 4.4(c)) do not change significantly for GNP and GNP/PDMS samples. Comparing RGO and RGO/PDMS samples however, the 2D band decreases significantly (Figure 4.4(c)) in intensity and the D band intensity increases (Figure 4.4(a)) and is quite intriguing. Plausible causes of change in D and 2D band intensities may suggest damage of the RGO due to shear mixing, doping of RGO by the polymer and functionalization of RGO sheets by the polymer. In order to ascertain whether the change in Raman D and 2D band intensity was result of mechanical damage over 7 days of shear mixing or doping and functionalization, the ratio of  $I_G/I_D$  and  $I_G/I_{2D}$  was measured at different intervals of mixing time.

Figure 4.4(d & e) presents the  $I_G/I_D$  and  $I_G/I_{2D}$  as a function of mixing time from 5 minutes to 168 hours. It is observed that within 5 minutes of mixing, the ratio's change and stays there even after 160 hours. As a comparison the ratio of  $I_G/I_D$  for pure RGO and GNP flakes are marked as such in Figure 4.4(d & e). Mechanical damage due to shear mixing should demonstrate progressive increase in D band intensity due to increased number of defects between shorter and longer intervals of time, which is not observed in Figure 4.4(d & e). The instantaneous change in  $I_G/I_D$  and  $I_G/I_{2D}$  suggests doping and functionalization of graphene sheets [193, 194]. The ratio of 2D to G band intensities ( $I_{2D}/I_G$ ) is a sensitive probe to monitor the effects of electron-donor and electron-acceptor molecules on electronic properties of graphene [193]. Electron-donors markedly decrease the ( $I_{2D}/I_G$ ) ratio while electron-acceptor molecules increase this ratio [193]. The ratio of  $I_D/I_G$  shows an opposite trend for the RGO/PDMS sample suggesting that as D band intensity increases, 2D band decreases [193]. Similarly, broadening of 2D bands and

increase in D band intensities could also mean high functionalization densities of the polymer as reported in the past [194].

**Table 4.1 Raman wavenumbers of D, G and 2D bands and their FWHM**

	D-band ( $\text{cm}^{-1}$ )	FWHM-D ( $\text{cm}^{-1}$ )	G-band ( $\text{cm}^{-1}$ )	FWHM-G ( $\text{cm}^{-1}$ )	2D-band ( $\text{cm}^{-1}$ )	FWHM-2D ( $\text{cm}^{-1}$ )	$I_G/I_D$	$I_G/I_{2D}$
GNP	1330.5	59.09	1575.8	18.27	2666.9	74.13	4.57	2.65
GNP/PDMS -Baking	1333.3	61.26	1580.1	24.38	2673.7	76.56	2.17	2.96
GNP/PDMS -NIR	1334.3	59.62	1580.4	19.35	2674.5	74.99	2.61	3.10
RGO	1336.1	195.25	1568.3	28.37	2654.6	84.97	4.24	3.80
RGO/PDMS -Baking	1351.6	222.48	1592.8	88.31	2673.7	726.72	0.96	21
RGO/PDMS -NIR	1352.5	216.26	1593.6	85.32	2675.1	722.18	0.98	27

Table 4.1 presents the  $I_D/I_G$  ratio and  $I_{2D}/I_G$  ratio for all samples tested. This table presents evolution of Raman bands both in pure and mixed polymer composites suggesting both doping and functionalization due to charge injection from the polymer as witnessed by the marked decrease in  $I_{2D}/I_G$  for the RGO samples. Recent reports on charge injection as a function of pressure have been quantified using Raman spectroscopy [195]. A marked decrease in  $I_{2D}/I_G$  values were seen in alcohol compared to argon with increase in pressure from 0-7 GPa of RGO and BLG samples on  $\text{SiO}_2$  substrates suggesting doping of the samples [195]. Since the experiments in this case were done at ambient pressure, the doping and functionalization is a result of the mixing process of the polymer interacting with the RGO defective sites. Mixing induced folding can result in unique D band and folds can appear as defective sites that can scatter phonons [196].

All these observations show that mixing of graphene in polymer such as PDMS results in charge injection even at ambient pressure and resulted in doping and functionalization. The source of the charge injection may be due to the reactive linkers in

PDMS namely silanol (Si-O-H) groups or from the methyl or ethyl groups from the side chains that have been used to link molecules to the Si-O backbones. Past work on using scanning surface potential microscopy to investigate the origins of gate hysteresis in nanotube field effect transistors have shown the charge injection from the silanol groups resulted in considerable screening of charges at the nanotube/SiO<sub>2</sub>/ambient interface [197]. So all these past reports mentioned above confirms our results on the effect of charge injection due to mixing of RGO in PDMS that resulted in shift in I<sub>2D</sub>/I<sub>G</sub> ratio.

#### 4.2.2 Raman-strain sensitivity of graphene/PDMS composites

Figure 4.5(a-1) and Figure 4.5(b-1) presents the shift in G band for GNP and RGO respectively. On application of ~10% compressive strain, the G band shifts to the left signaling lattice tension. Similarly, on application of 50% tensile strain, the G-band shifts right or increasing in wavenumbers. This suggests lattice compression. These results are true for RGO/PDMS samples too as shown in Figure 4.5(b-1). These results are also in agreement with the earlier work on load transfer in GNP polymer composite.

Figure 4.5(a-2) and Figure 4.5(b-2) presents the Raman wave number change as a function of strain for GNP/PDMS and RGO/PDMS samples. As presented in both the figures, the conventional oven baked samples in both GNP/PDMS and RGO/PDMS resulted in lower Raman wave number change or less load transfer on application of strain. The NIR polymerization produced much higher change in Raman wave numbers thereby demonstrating enhanced load transfer from polymer to the filler. Since the SEM and Raman signatures of the G band look similar for both baking and NIR polymerization,

characterizing wavenumber shift in G peak in both samples upon application of strain is a measure of the graphene/polymer interfacial strength. Our results suggest that RGO/PDMS sample polymerized using NIR irradiative technique exhibited higher interfacial strength compared to their GNP counterparts.

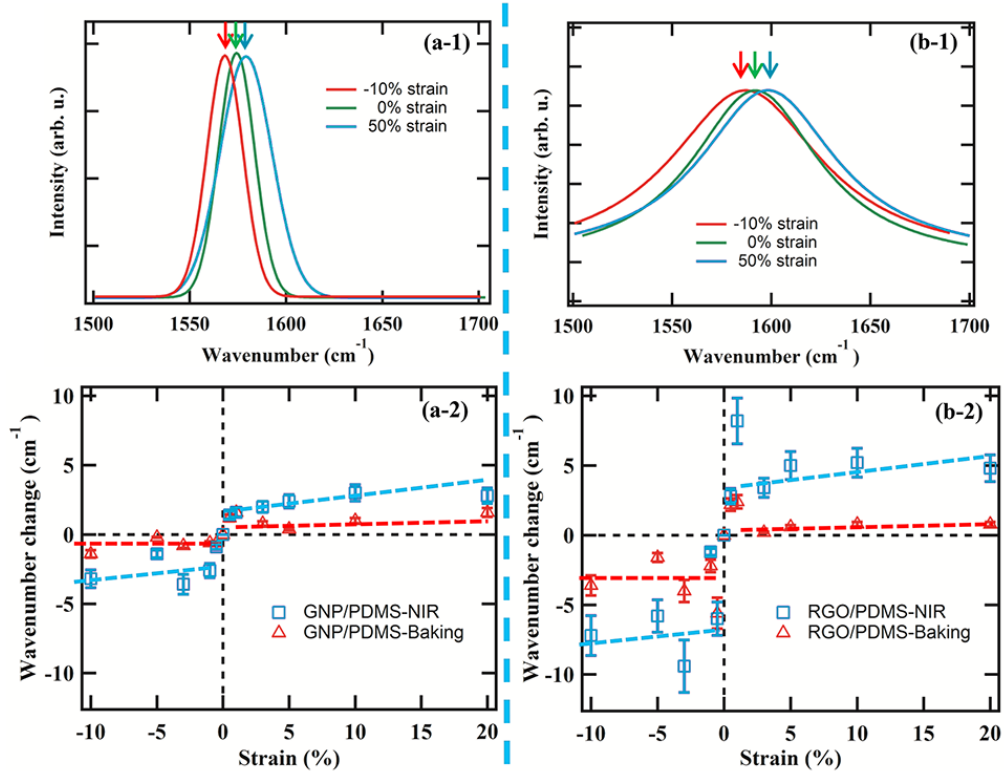


**Figure 4.5 Load transfer: G band shift in (a-1) GNP/PDMS and (b-1) G band shift; change in wavenumbers with strains of (a-2) GNP/PDMS and (b-2) RGO/PDMS.**

The change in Raman wavenumbers saturate at  $\sim 10\text{-}12\text{ cm}^{-1}$  after 20% strain in both GNP and RGO counterparts and strains are no longer resolvable  $> 20\%$ . This suggests that the saturation of the Raman signal is related to the number of graphene/polymer sites or weight fraction of the graphene in polymer matrix. This was also seen in past studies on nanotube/polymer composites. It should be noted that such

impressive change in wavenumbers for ~20% strain considering the low fraction of graphene (~1 wt %) used in these composites. For GNP/PDMS composites, rate of peak shift with strain was ~ 2.4 cm<sup>-1</sup>/% strain in tension and ~1.2 cm<sup>-1</sup>/% strain under compression as shown in Figure 4.5(a-2) and rate of peak shift is similar to the earlier report [34]. In addition, we also measured the 2D band shifts that were quantified to be ~0.8 cm<sup>-1</sup>/% strain under tension and ~0.7 cm<sup>-1</sup>/% strain under compression, which was smaller than G band, however demonstrating use of 2D band shift in GNP fillers for measuring load transfer. On the contrary, the 2D bands were the most sensitive to strains in CNTs where 6 cm<sup>-1</sup>/% was witnessed in tension in our past work for the same process conditions [173]. Based on the G-band Raman shift, the interfacial stress was calculated to be ~80 GPa for the GNP/polymer interface in compression. For RGO/PDMS, rate of G-peak shift with strain was ~4.4 cm<sup>-1</sup>/% strain in tension and ~11.2 cm<sup>-1</sup>/% strain in compression suggesting enhanced load transfer in compression in bulk. The interfacial stress was calculated to be ~410 GPa for RGO interface suggesting fivefold increase in stress transfer in compression. For tension, the load transfer of RGO polymer interface was calculated to be ~3.5 times that of GNP interface. This also suggest greater load transfer of RGO compared to single wall nanotube fillers in tension [34]. Enhanced load transfer was witnessed for RGO fillers in both tension and compression compared to GNP fillers (Figure 4.5). Such large Raman shifts suggest large bond deformation, minimum slippage that must originate only from intimate contact of the RGO with the polymer and better dispersion through long mixing. Comparing this to past report on nanotube composites have only demonstrated either large Raman peak shift (15 cm<sup>-1</sup> of 2D band) in compression and small peak shift in tension [191].

Investigating further, full width half maximum (FWHM) of the wavenumbers were plotted against strain to investigate the extent of slippage in graphene/polymer composites. The extent to which graphene sheets will slip inside the polymeric matrix on application of strain is relatively unknown. Depending on the morphology and the number of layers, it is expected that RGO will slip less compared to its rigid stack like GNP counterparts. Figure 4.6(a & b) presents the FWHM data for both the types of graphene and both types of polymerization. First and foremost, graphene/polymer composites (both RGO and GNP) undergo slippage in the polymer matrix similar to CNTs. For the oven based baking method, GNPs underwent significant slippage compared to their RGO counterparts. This can be explained from the rigid plate like morphology. GNPs in polymers act as discrete rigid plates and do not interact with the polymer. This resulted in the plate sliding in the matrix much more easily on application of strain. FWHM data in compression show almost  $15\text{ cm}^{-1}$  for 10% compression. The sign of the FWHM also change quite dramatically on changing the compression. This suggests discrete movement of GNPs in the polymer matrix or slippage. However, for RGO, the SEM images from Figure 4.1 show a continuous matrix. RGO due to its one carbon layer can weave itself with the polymer creating a continuous matrix. This resulted in better dispersion and higher change in Raman wavenumbers upon application of strain for both the fabrication methods. The higher integration of RGO also meant minimum slippage both in tension and compression for the oven baked samples. For the NIR treated method, there is a dramatic difference in GNP based polymer composites. The NIR treated method resulted in no slippage of the GNP in the polymer matrix. The FWHM data is seen to be almost zero for both compression and tension. This can only

happen through better integration of the GNPs in the matrix. On irradiation of NIR light, the GNPs edges should heat up to high temperatures at the nano-scale thereby bonding with the polymer matrix. This probably does not occur for the oven baked methods. In oven baked samples, heat is transferred from the outside to the inside the matrix. Depending on the thermal conductivity of the matrix and fillers and the polymer chain lengths, hot and cold spots may exist at the nanoscale that can locally change the polymerization process. On the other hand the NIR irradiation resulted in heating the fillers all over the matrix that may result in shorter segmental chain length of the polymer and therefore can result in stiffer composite.

Similarly, Figure 4.6(b) for RGO composite show minimum slippage for the NIR treated method compared to the oven baked method although the result is not as dramatic as the GNPs in Figure 4.6(a). This again may be due to the morphology of the RGO weaving itself in the polymer matrix that results in better dispersion and integration for both polymerization methods.

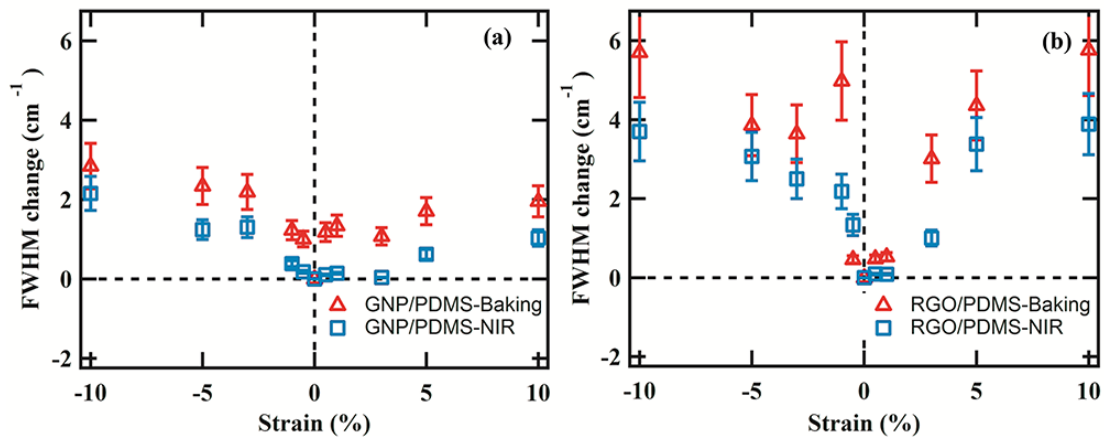


**Figure 4.6 G-band FWHM value of GNP/PDMS (a) and RGO/PDMS (b) polymerized by conventional baking (blue) and NIR photon-assisted method (red) versus strain**

### 4.2.3 Mechanical properties of graphene/PDMS composites

Figure 4.7(a-1 & b-1) presents the cyclic stress-strain curves of PDMS, GNP/PDMS, and RGO/PDMS samples polymerized by conventional oven and NIR photon-assisted method respectively. The area under the hysteresis curve represents energy loss during the loading and unloading cycles. The area under hysteresis curve is larger for NIR samples indicating 1431% (RGO/PDMS) and 324% (GNP/PDMS) improvement in damping capability compared pure PDMS. On the other hand, area under the hysteresis loop is smaller for conventional baking samples ~673% increase for RGO/PDMS and ~139% increase for GNP/PDMS compared pure PDMS. High performance of NIR photon-assisted polymerization is addressed. Besides, RGO/PDMS shows higher damping capability than GNP/PDMS using the same polymerization method. The large damping capability of RGO fillers demonstrate considerable interfacial slippage between the PDMS and fillers and high thermal conductivity [198]. This brings in an interesting question of whether the orientation of the graphene with respect to the longitudinal or transverse loading can affect energy dissipation and could serve as useful design parameter for future composites and is worth investigating in future.

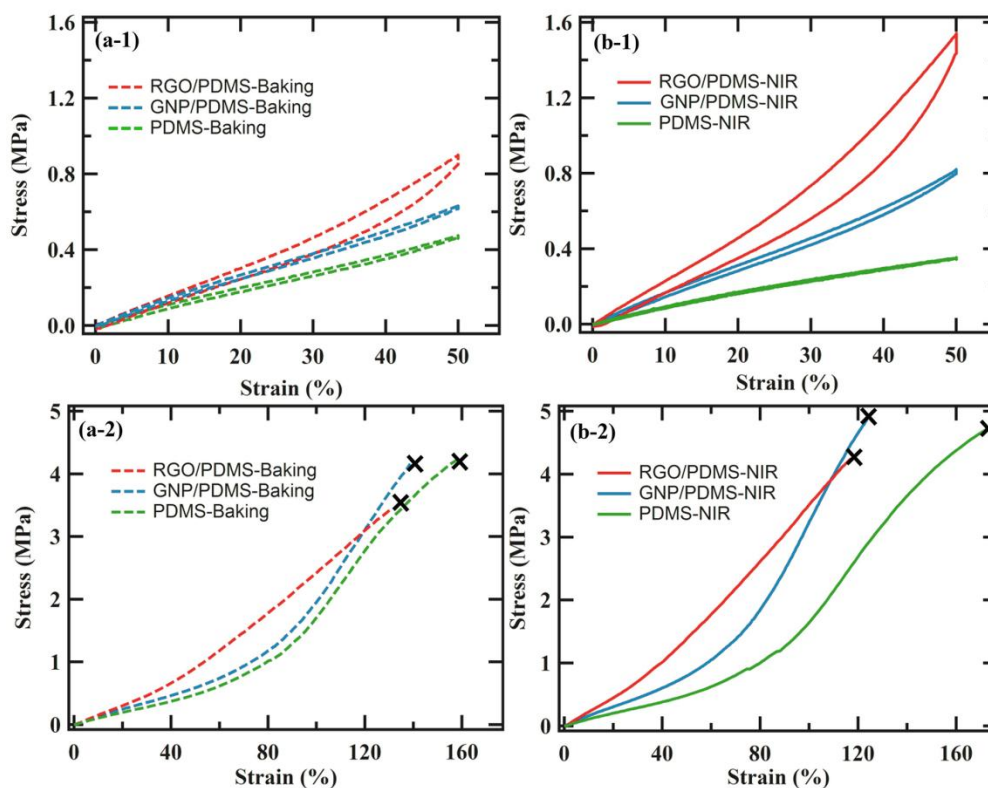


**Figure 4.7 Cyclic stress-strain curves (a-1) and stress-strain curves (a-2) until failure of pure PDMS, RGO/PDMS, and GNP/PDMS polymerized by conventional baking method; Cyclic stress-strain curves (b-1) and stress-strain curves (b-2) until failure of pure PDMS, RGO/PDMS, and GNP/PDMS polymerized by NIR photon-assisted method.**

Figure 4.7(a-2, b-2) presents the stress-strain curves of GNP/PDMS, RGO/PDMS and pure PDMS samples till failure under different polymerization methods. As more strain is applied, the polymeric chains in PDMS are stretched out till final failure was seen ~160%. RGO/PDMS samples exhibited a linear stress-strain curve with failure at ~120%, almost 25% lower failure strains. This suggests considerable stiffening of the matrix with addition of RGO at these low weight percentages. The increase in Young's modulus for RGO/PDMS was ~42% while that of GNP/PDMS was ~32% polymerized by conventional baking method in Figure 4.7(a-2). Figure 4.7(b-2) presents increase in

Young's modulus for RGO/PDMS was ~115% while that of GNP/PDMS was ~55% polymerized by NIR photon-assisted method.

Comparing two graphene/PDMS samples polymerized by NIR photon-assisted method, this was calculated at  $2.20 \text{ MJ/m}^3$  for RGO/PDMS,  $1.76 \text{ MJ/m}^3$  for GNP/PDMS and  $0.97 \text{ MJ/m}^3$  for pure PDMS at 115% end point strain. The flexibility of RGO can result in large energy absorption without failing resulting in increased toughness of the composite. Finally, energy density values were calculated as  $\sim 2.14 \text{ kJ/Kg}$  for RGO/PDMS,  $\sim 1.68 \text{ kJ/Kg}$  for GNP/PDMS and  $\sim 0.91 \text{ kJ/Kg}$  for pure PDMS. This suggests an increase in strain energy density of  $\sim 233\%$  for RGO fillers in PDMS. The high surface area of RGO sheets makes the intimate interaction with the polymer due to increased adhesion resulting in higher strain energy densities [199]. In the elastic regime, these high densities can be recovered as useful mechanical work thereby making RGO highly attractive for realization of advanced composites.

Figure 4.8(a) presents Young's modulus as a function of NIR energy dose with 1 wt. % RGO/PDMS and GNP/PDMS. For both graphene/PDMS composites, Young's modulus will increase while increasing NIR dose. Young's modulus of RGO/PDMS is much higher than modulus of GNP/PDMS due to higher surface area of RGO compared to GNP with same weight percentage. Figure 4.8(b) compares the change in Young's modulus as a percentage for RGO/PDMS and GNP/PDMS polymerized by NIR photon-assisted treatment. It is clear that for all wt. % graphene, change in Young's modulus is higher for RGO samples compared to GNP samples.

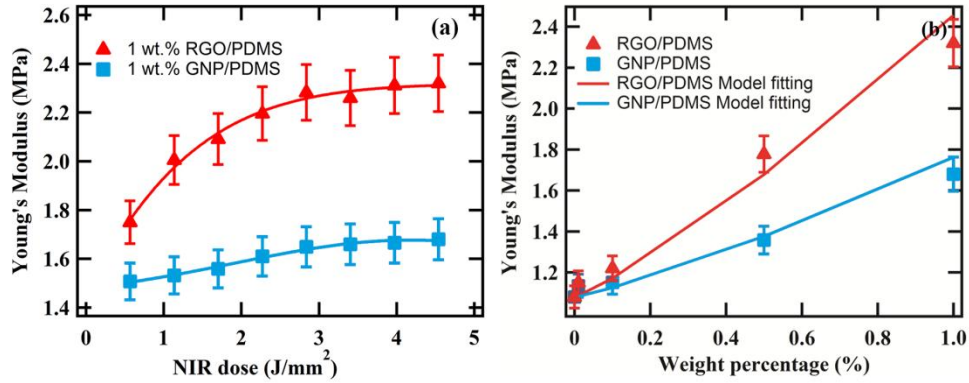


Figure 4.8 (a) Young's modulus versus NIR light dose for RGO/PDMS (red line) and GNP/PDMS (blue line) fractions; (b) change in Young's modulus versus weight percentage of RGO (red line) and GNP (blue line) for NIR light treated.

Calculating the change in Young's modulus, Table 4.2 presents the Young's modulus values and the change in Young's modulus with respect to the pristine polymer for each of the fabrication method. There was ~32.14% change in Young's modulus for the GNP/PDMS composite compared to the pristine polymer for the oven based polymerization. The change in Young's modulus was ~42.86% for RGO/PDMS samples for this polymerization method. On the other hand, the NIR treatment resulted in ~115.81% change in Young's modulus values for RGO/PDMS and ~55.56% change in Young's modulus for GNP/PDMS. These results suggest that the graphene polymer composites are getting stiffer due to NIR irradiation.

Table 4.2 Young's modulus and Young's modulus change of different graphene/PDMS composites with different polymerization methods

Composite (1 wt. % nano-carbon/PDMS)	Young's modulus (MPa)	Young's modulus change
Pure PDMS-Baking	1.12 ± 0.02	--
GNP/PDMS-Baking	1.48 ± 0.02	32.14 %
RGO/PDMS-Baking	1.60 ± 0.03	42.86 %
Pure PDMS-NIR	1.08 ± 0.02	--
GNP/PDMS-NIR	1.68 ± 0.03	55.56 %
RGO/PDMS-NIR	2.32 ± 0.01	115.81 %

### 4.3 Conclusion

In conclusion, NIR photon-assisted polymerization of graphene/PDMS composites was demonstrated in this chapter. The first and most important conclusion is that mixing RGO in polymers can influence its G and 2D band significantly compared to its few layer counterparts. The ratio of  $I_G/I_{2D}$  went from 2.65 for GNP to  $\sim 3$  for GNP/PDMS, while from 3.80 to  $\sim 25$  for RGO/PDMS counterparts. This suggests significant electron doping in line with earlier studies on monolayer graphene. By investigating the changes in 2D and G band one can understand the effects of doping, and graphene crystallite size due to mixing on the eventual electron-phonon interactions. This study investigated two types of polymerization of graphene/PDMS composites namely: 1) oven based heating to 125 C for 30 minutes and 2) NIR irradiation. The G bands of pure fillers and post fabrication of GNP or RGO/PDMS composites were found to be shifted suggesting compressive loading on the filler lattice. The out of plane vibration due to the polymer entanglement is coupled to the in plane vibration of the  $sp^2$  carbon atoms suggesting three dimensional entanglement of the polymer to the filler lattice. Investigating the two polymerization techniques, it was found that NIR based polymerization resulted in higher load transfer and mechanical strength of GNP and RGO based composites. The load transfer was higher for RGO/PDMS based composites compared to GNP/PDMS based composites for both types of polymerization. The rigid stack like morphology of the GNPs and the lack of interplate interactions with the polymer using conventional oven based polymerization played an important role in slippage during load transfer and lower mechanical strength. On the other hand, RGO

sheets were able to weave itself with the polymer thus enabling a continuous polymeric composite that enabled higher load transfer and minimized slippage. The NIR treatment resulted in ~115.81% change in Young's modulus values for RGO/PDMS and ~55.56% change in Young's modulus for GNP/PDMS showing differences in mechanical strength of composites for just few atomic layers of carbon.

## **CHAPTER 5 SYNERGY EFFECT OF BINARY (1D MWNT, 2D RGO) NANO-CARBONS/POLYMER COMPOSITES**

### **5.1 Introduction**

In the previous chapter, the use of NIR polymerization of graphene/polymer composite was demonstrated. In this chapter, we investigated the use of 2 different nano-carbons in polymer composites and how their interaction in polymer composites affects the overall mechanical properties of the polymer composites. In general use of two nano-carbons based on different dimensionalities can result in enhanced stiffness of the composite and overall improvement in mechanical properties. However, it could also show some insights into how two different nano-carbons with different geometric shapes can limit deformation in composites. Raman spectroscopy again aids in looking into such interesting behavior, therefore extending the possible applications of non-destructively studying the internal dynamics of polymer composites.

An important application of graphitic nano-carbons is their use as reinforcers/fillers in polymer composites for enhanced mechanical strength and load transfer. In this respect, use of CNTs has been effective due to their high tensile strength, high aspect ratio, and one-dimensional (1D) nature leading to directional stress transfer and compatibility with surface functionalization techniques [19-24, 26, 29, 160, 164, 166-168, 200-209]. Recently, two-dimensional (2D) graphitic nano-carbon, namely few layer GNPs, have shown impressive load transfer both in tension and compression when acting

as reinforcers in polymer composites [34]. A surprising observation was that for large strains (>1.5%), GNP fillers went into compression under uniaxial tensile deformation. Similarly, under uniaxial compressive load, the Raman signature was one that of tension in the lattice. This effect although intriguing is not yet well understood. Further, lack of clear understanding of how mechanical strength and load transfer are affected in binary mixtures of nano-carbon/polymer composites warrants further investigation.

### 5.1.1 Synergy in binary nano-carbons in polymer composites

Recent reports have shown extraordinary synergy in binary nano-carbon mixtures consisting of SWNT and nano-diamonds (ND), and few layer graphene (FLG) and ND in matrix of polyvinyl alcohol (PVA) [210]. The nano-carbons (ND, SWNTs and FG) were surface functionalized using acid treatment to form carboxyl and hydroxyl groups that could better interact with the PVA matrix [210]. The ~400% enhancement in Young's modulus of PVA was reported due to the inducement of crystallization of the polymer with addition of nano-materials [210]. Since that impressive study, further studies have shown synergistic effects of increased toughness resulting from the combination of SWNTs and RGO flakes in solution-spun polymer fiber [211]. Similarly, not only mechanical strength, synergistic effects in thermal conduction has been reported in hybrid GNP-MWNT fillers in epoxy composites. Thermal conductivity enhancement of ~800% at ~10 wt. % loading of hybrid nano-carbons in epoxy was demonstrated [212]. Synergistic effects of SWNT and GO composite fibers coagulated from acidic PVA solution exhibited both high strength and high conductivity and was reported to be

promising candidates for actuation applications [213]. While these studies are quite impressive and show the synergy between use of binary mixtures of nano-carbons in polymers affecting mechanical strength, interfacial thermal conductivity, and device actuation, Raman spectroscopy has not been previously employed to investigate actual change in lattice expansion or contraction due to cooperative effects of binary mixtures of nano-carbons for load transfer/mechanical strength/interfacial thermal conduction.

### 5.1.2 Raman spectroscopy of binary nano-carbons in polymer composites

Over the years, Raman spectroscopy has emerged as a powerful method in understanding load transfer and mechanical properties of single nano-carbon/polymer composites. It was Ajayan *et al.*, who demonstrated load transfer in a MWNT/epoxy system using Raman spectroscopy [19]. The enhanced shift in Raman G' mode during compression demonstrated higher interfacial shear stress and load transfer to the nanotubes [19]. Since then, numerous reports have emerged on the use of Raman spectroscopy for studying load transfer and mechanical strength of nano-carbon reinforced polymer composites using both G-band shifts and 2D-band shifts [19, 160, 168, 171, 172, 209, 214, 215]. However, there are no studies on how load is transferred in polymer composites consisting of binary nano-carbon mixtures using Raman spectroscopy.

Raman spectroscopy studies on binary mixtures of nano-carbons polymer composites in tension and compression can give us a deeper understanding of how strains are developed in the lattice and the synergy of two carbons in different dimensional states

aiding load transfer. The use of binary mixtures of nano-carbon as reinforcers in polymer matrix could have different impacts on load transfer and mechanical strength. Extraordinary synergy is only achieved at a specific concentration of the nano-carbons in the polymer matrix and therefore is not an additive property. One can envision different scenarios of mixing binary mixtures of nano-carbons in polymer matrix: 1) load could be shared equally by both the nano-carbons (this could potentially occur at equal weight percentages or same dimensional state), 2) load could be shared predominantly by one nano-carbon, thereby eliminating influence of the second carbon, 3) one of the nano-carbons may limit the deformation of the other in the matrix resulting in selective and directional load transfer, 4) shape induced anisotropy of the nano-carbons can result in enhancement in stiffness and mechanical strength, and 5) adding binary mixtures of nano-carbons and subsequent polymerization of the composite can lead to smaller segmental chain length and limited extensibility of polymer chains. Finally, dimensionality and mechanical properties of individual nano-carbons should also play a significant role in enhancing interfacial interactions in determining collective composites properties. Therefore, we investigated load transfer and mechanical strength of binary mixtures of nano-carbon fillers in PDMS matrix using Raman spectroscopy. PDMS was used in this study due to its high significance in many day to day industrial applications. PDMS belongs to the group of silicones and is a common polymer used in industries, such as medical, food, aerospace, tri-biological, lithographic, cosmetics and microfluidics. Recently nano-carbons in PDMS have found applications as photo-thermal polymerization agents and photomechanical actuators [79, 173, 216-218]. Such actuators have found applications in MEMS as micro-actuators, micro-mirrors, and micro-grippers

utilizing photomechanical actuation principle [219-222]. Therefore, the present investigations could make an impact in the above mentioned areas where synergy between nano-carbons can be exploited for actuation applications. Our results suggest small amounts of MWNT<sub>0.1</sub> in RGO<sub>0.9</sub>/PDMS matrix (for simplicity we refer wt. % of nano-carbon as subscripts) eliminates the previously reported compressive deformation of RGO [34], thereby reversing the sign of the Raman wavenumber changes (from positive to negative) in uniaxial tension. This resulted in load transfer to RGO and almost fourfold increase in Young's modulus compared to single nano-carbon RGO<sub>1.0</sub>/PDMS and MWNT<sub>1.0</sub>/PDMS counterparts. We discuss a mechanism where strain induced orientational order of MWNT and the shorter segmental length and the limited configuration of the polymeric chain on MWNT addition can result in the synergistic effect of eliminating the compressive deformation of RGO in direction perpendicular to the applied strain thereby changing the sign of Raman wavenumbers and increasing the Young's modulus.

## **5.2 Results and Discussion**

Different binary mixtures of RGO and MWNTs were dispersed in the PDMS (Sylgard) matrix and these samples were used to study the synergistic effect on the load transfer and the mechanical strength. The prepared samples were first investigated by using SEM to examine the sample cross-sections and the nano-carbon/polymer interface. Raman spectroscopy was used to ascertain the Raman peak shift with increasing strains to compare the load transfer between adding single nano-carbon filler or binary mixtures

of nano-carbon fillers in polymer matrix. The elastic moduli ( $E$ ) were measured for the series of samples. (See experimental details in Appendix C)

### 5.2.1 Characterization of binary mixture nano-carbons/PDMS composites

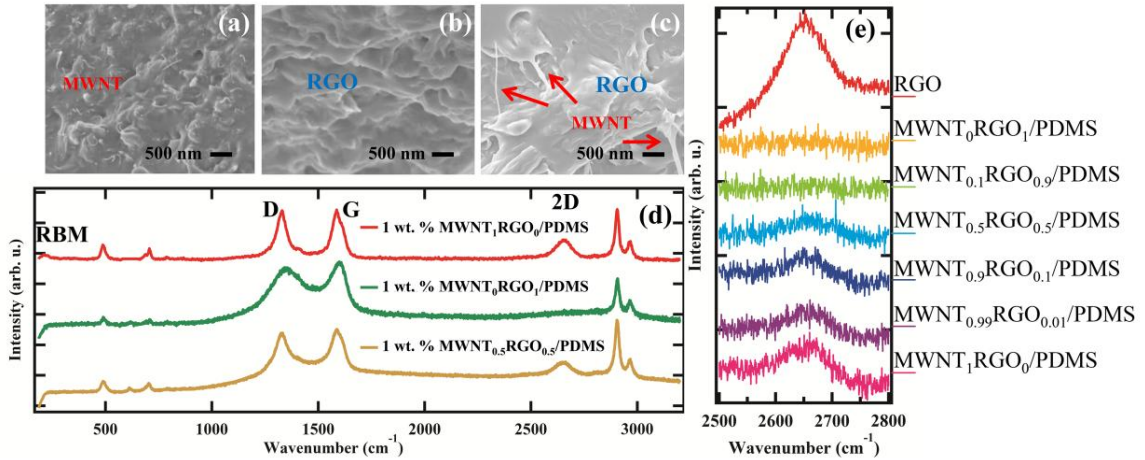


**Figure 5.1** The SEM images of (a) MWNT<sub>1</sub>RGO<sub>0</sub>/PDMS, (b) MWNT<sub>0</sub>RGO<sub>1</sub>/PDMS, (c) MWNT<sub>0.5</sub>RGO<sub>0.5</sub>/PDMS, each with a scale bar of 500 nm. (d) The Raman spectra of (a-c) samples. (e) The comparison of 2D peaks between pure RGO and a series of MWNT- RGO/PDMS composites.

Figures 5.1(a), 5.1(b), and 5.1(c) display the cross-sectional SEM images for the MWNT<sub>1</sub>RGO<sub>0</sub>/PDMS, MWNT<sub>0</sub>RGO<sub>1</sub>/PDMS, and MWNT<sub>0.5</sub>RGO<sub>0.5</sub>/PDMS samples respectively. The SEM image for MWNT<sub>1</sub>RGO<sub>0</sub>/PDMS (Figure 5.1(a)) clearly shows dispersion of MWNTs in the matrix. One end of the MWNT appears stretched out of the matrix while the other end is embedded in the matrix. This is indicative of the strong interfacial adhesion between the nanotube and the PDMS polymeric chains [29]. The SEM image of MWNT<sub>0</sub>RGO<sub>1</sub>/PDMS (Figure 5.1(b)) shows that the plate-like morphology is retained in the polymer matrix. The SEM image of the MWNT<sub>0.5</sub>RGO<sub>0.5</sub>/PDMS (Figure 5.1(c)) shows a combination of the retention of RGO

morphology and the nanotubes stretched out of the polymer. Particularly, there are places where the nanotubes are seen to bridge the gap between two RGO/PDMS plate structures (arrows in Figure 5.1(c)). The SEM images clearly show that the MWNTs covered in PDMS act as bridges between two RGO plates. Even in the mixtures, one end of the MWNT is seen to stretch out of the matrix while the other end is anchored in the RGO/PDMS matrix (Figure 5.2(c)). This again reveals the strong interfacial adhesion of the MWNTs in the mixtures.

The Raman spectra for the three samples are displayed in Figure 5.1(d). All the 9 peaks associated with PDMS are shown for the samples. For the MWNT<sub>1.0</sub>RGO<sub>0.0</sub>/polymer sample, the RBM mode at  $\sim 219.3 \text{ cm}^{-1}$ , the disorder induced D band at  $\sim 1,329 \text{ cm}^{-1}$ , the tangential mode G-band at  $\sim 1,588 \text{ cm}^{-1}$ , and the 2D or G'-band at  $\sim 2,657 \text{ cm}^{-1}$  are associated, demonstrating the high purity of the prepared sample. For the MWNT<sub>0</sub>RGO<sub>1</sub>/PDMS samples, the D-band at  $\sim 1,344 \text{ cm}^{-1}$ ) and the G-band at  $\sim 1,596 \text{ cm}^{-1}$  are clearly measured. The previous Raman study on monolayer graphene on PDMS has measured the G-band at  $\sim 1581.6 \pm 15.6 \text{ cm}^{-1}$  [223]. Therefore, our measured G-band peak is within the fluctuations for monolayer graphene. The 2D band appears at  $2680 \text{ cm}^{-1}$  but is very weak for these spectra. The low intensity of the 2D resonance and the broadening of the G-band and the D-band indicate high functionalization densities of graphene as seen in the past report [194]. This suggests higher level interaction of RGO with the polymer.

Figure 5.1(e) presents the evolution of the 2D band for the pure RGO and the RGO/PDMS mixtures with MWNT. For the binary mixtures the 2D peak was seen to increase in intensity with addition of MWNT. Ideally, lack of any defect center in RGO

should lead to no D-band. The presence of the D-band in the measured spectra, its broadening and the lower intensity of the 2D peaks may suggest the folding of the graphene sheet induced during the evaporative mixing process [196]. The spatially inhomogeneous curvature of the RGO in polymer can act as a smooth one dimensional defect line along the fold and therefore can lead to the D-band peak for the RGO/PDMS composite [196]. The direct contact of the polymer to the RGO and the process of mixing over 24-36 h inside the polymer can lead to folds, kinks, and doping and functionalization of the graphene sheets, all of which can induce a D-band, broaden G band and lower the relative intensity of the 2D band. While this warrants further investigation, the lower intensity of the 2D band suggests that the electronic properties of RGO are directly affected by mixing in the polymer. The decrease or increase in  $I_G/I_{2D}$  compared to the pure samples may be indicative of hole or electron doping respectively. Based on the intensity values,  $I_G/I_{2D} = 10.5$  was calculated for the RGO samples and  $I_G/I_{2D} = 132.2$  was calculated for the RGO/PDMS sample. This may not be the case for FLG as only the top layer comes in contact when mixed with the polymer and keeps the layers in between in pristine condition. Therefore, the 2D band is expected to have higher intensities even when mixed in polymers for FLG compared to their RGO counterparts or no change in the electronic properties. For FLG, we found  $I_G/I_{2D} = 3.1$  and for FLG/PDMS,  $I_G/I_{2D} = 3.0$  was found from our measurements. This show that during mixing with polymers RGO is affected more by the polymer compared to the FLG. The lack of variation of  $I_G/I_{2D}$  for FLG and FLG/PDMS is remarkable and shows that the electronic properties for FLG are not affected by mixing with the polymer. A fundamental result observed in this study is

that mixing RGO in polymers can have a profound effect on its Raman bands and could have significance in fabrication and characterization of advanced composites.

For the Raman spectrum of the binary mixture MWNT<sub>0.5</sub>RGO<sub>0.5</sub>/PDMS, the D-band (1,344 cm<sup>-1</sup>), G-band (1593 cm<sup>-1</sup>) and 2D-band (2,654 cm<sup>-1</sup>) are clearly visible. The appearance of the 2D band in binary mixtures may suggest that the electronic properties of the CNTs are unaffected by the curvature effects [224]. The similarity of the 2D peak compared to the pure MWNT/PDMS samples with lower relative intensity may suggest the MWNT entanglement atop the graphene sheet, similar to the decrease in relative intensity of 2D peaks with increase in number of graphitic layers (FLG) [224]. This is quite reasonable as the SEM investigation also suggests the entanglement of MWNTs on the RGO plates. Based on the RBM mode of the nanotube/polymer sample, the diameter of the nanotube was calculated using equation  $\nu_{\text{RBM}} = A/d + B$ , where  $A = 233 \text{ cm}^{-1} \text{ nm}$  and  $B = 10 \text{ cm}^{-1}$  are constants. It gives an inner diameter for MWNTs at  $\sim 1.06 \text{ nm}$ . The diameter value based on the RBM mode in the nanotube/polymer samples demonstrates the lack of bundling of the MWNTs and excellent dispersions within the polymer samples using the evaporative mixing and the NIR cross-linking process [225]. Lack of bundling and smaller diameters may also indicate a higher level nanotube/polymer interaction, leading to better interfacial adhesion and strength.

Figure 5.2 presents the SEM images of MWNT<sub>0.5</sub>RGO<sub>0.5</sub>/PDMS at three different areas. In all the three areas, nanotubes are seen to bridge the RGO plates in the polymer matrix. The SEM images show a density of 1-2 MWNT or small bundle bridging adjacent RGO plates. This is reasonable given the small weight fraction of MWNTs. Figure 5.2(d) presents a schematic model based on the SEM observation of how the

MWNTs are arranged among the graphene plates. The 1D nature of MWNTs can cause entanglement of the individual tubes between the mesh like RGO lattice in the polymer. The long evaporative mixing and subsequent polymerization cause the MWNTs to be entangled in the RGO lattice permanently by the polymeric chains. This may warrant further investigation as long or short chain polymers can have different effects on the entanglement of MWNT that may affect the overall properties of the composites.

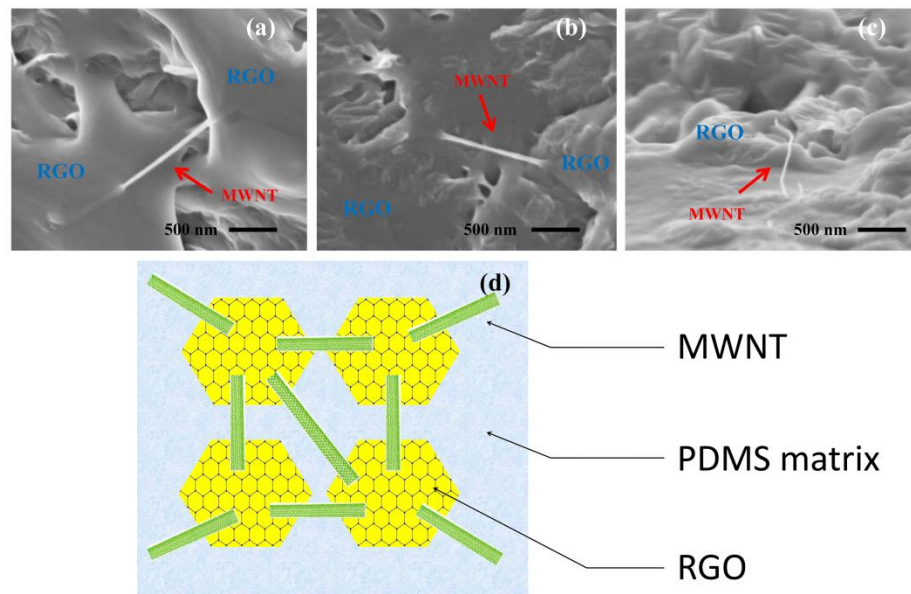


**Figure 5.2 (a-c) The SEM images of MWNT<sub>x</sub>RGO<sub>1-x</sub>/PDMS matrix, and (d) the schematic representation of the RGO-MWNT/polymer system based on the above SEM images.**

### 5.2.2 Raman-strain sensitivity of MWNT/PDMS and RGO/PDMS composites

Raman spectroscopy has been used by many groups in the past to measure the strain in the nanoscale fillers such as CNTs and graphene [19, 161-168]. When a strain is applied, the change of the interatomic distance induces shift in the vibrational frequencies.

The G-band ( $\sim 1,588 \text{ cm}^{-1}$ ) and G'-band ( $\sim 2,700 \text{ cm}^{-1}$ ) are known to exhibit such shifts both for MWNT and RGO, and thus can serve as the Raman signatures [34]. The larger shift in the Raman peak position of the G-band or the G'-band is indicative of larger load carried by the nano-carbon. A recent study on the graphene/polymer composites, with few layer graphene sheets subject to strain on top of different substrates, showed that the G-band shift by the rate of  $\sim 10 \text{ cm}^{-1}/\text{strain } \%$  [34]. In our study, we also used the G-band to investigate the load transfer because the 2D band in RGO/PDMS is shown as weak in Figure 5.1(c). An increase in the G-band wavenumber with increasing strain signals in-plane lattice compression, while a decrease in the G-band wavenumber with increasing strain signals tensile forces on the nano-carbon lattice. Thus, the shift measurements of the G-band peak for the various samples under both tension and compression can determine the strength of the nanotube-polymer interface and the comparison study may lead to in-depth understanding of the synergistic effects in binary nano-carbon/polymer composites.

In order to use the G-band to investigate the synergistic effects, Raman spectroscopy was conducted on MWNT<sub>1</sub>RGO<sub>0</sub>/PDMS and MWNT<sub>0</sub>RGO<sub>1</sub>/PDMS separately under tension and compression. Figure 5.3((a-1) & (b-1)) presents the shift in G-band peak position from  $-10\%$  to  $50\%$  strain. The G-band peak under  $0\%$  strain was measured at  $\sim 1,588 \text{ cm}^{-1}$ . Similar to the past report on MWNTs [225]. By contrast, the opposite trend was observed on the MWNT<sub>0</sub>RGO<sub>1</sub>/PDMS (Figure 5.3(b-1)). Under  $10\%$  uniaxial compression the G-band peak shifted to a smaller wavenumber (inferring a net tensile strain) and under  $50\%$  uniaxial tension the G-band shifted to a larger wavenumber (inferring net compression). This observations in line with the recent report for the GNP

polymer composites [34]. This suggests that the application of uniaxial tension in one direction induces compression of the RGO lattice in the other. This may be due to that the polymeric chains extend along the direction of the strain owing to the lower glass transition temperature and rubbery elasticity [34].

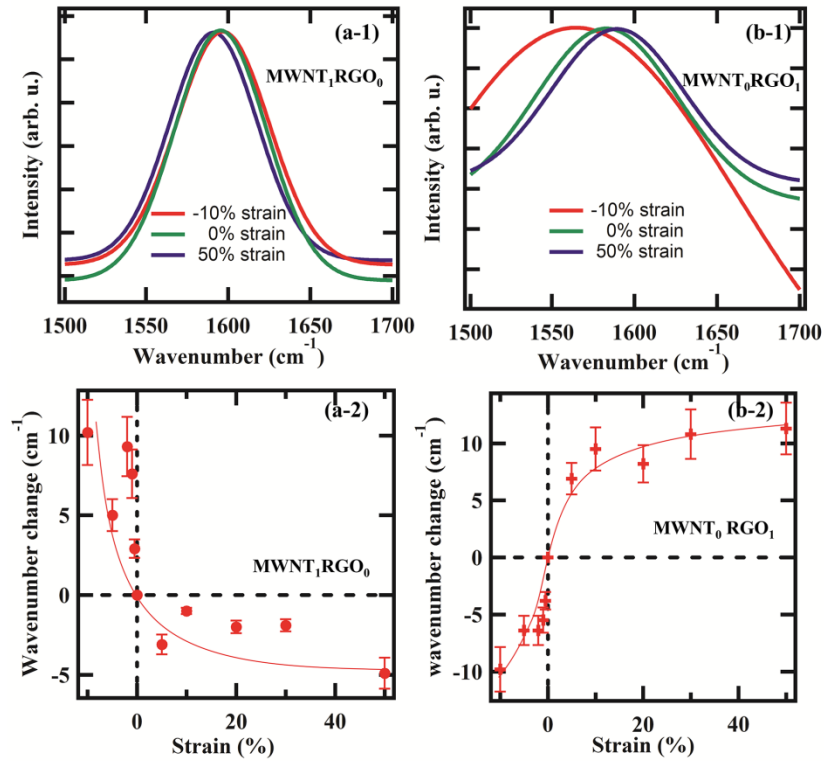


Figure 5.3 (a-1) & (b-1) plot the Raman intensity versus the shift in wavenumber under uniaxial tension and under uniaxial compression for MWNT<sub>1</sub>RGO<sub>0</sub> and MWNT<sub>0</sub>RGO<sub>1</sub>, respectively; (a-2) & (b-2) plot the change of the shift in wavenumber versus the strain under uniaxial tension and under uniaxial compression for MWNT<sub>1</sub>RGO<sub>0</sub> and MWNT<sub>0</sub>RGO<sub>1</sub>, respectively

Figures 5.3((a-2) & (b-2)) show the change of the Raman peak in wavenumber as a function of the applied strain for MWNT<sub>1</sub>RGO<sub>0</sub>/PDMS and MWNT<sub>0</sub>RGO<sub>1</sub>/PDMS, respectively. In Figure 5.3(a-2), the change of the Raman shift in wavenumbers is ~10 cm<sup>-1</sup> under compression while it is only ~5 cm<sup>-1</sup> under tension shows that larger load

is transferred to the MWNT filler under compression. For the MWNT<sub>0</sub>RGO<sub>1</sub>/PDMS, there was ~10 cm<sup>-1</sup> change in wavenumbers in both tension (50%) and compression (10%), but in the opposite direction as MWNT fillers (Figure 5.3(b-2)). Again, the shift in wavenumbers was 1 cm<sup>-1</sup>/% strain in compression and 0.2 cm<sup>-1</sup>/% strain in tension, suggesting that larger load is transferred under compression. It should be noted that there is no linear relationship between the Raman wave number change and the tension and compression strain.

### 5.2.3 Synergy effect of binary mixture nano-carbon/PDMS composites

Using the Raman signature to probe the binary mixtures (Figure 5.4), the synergistic effects on the load transfer are revealed for the MWNT<sub>x</sub>RGO<sub>1-x</sub>/PDMS samples. First, as shown in Figure 5.4(a) for MWNT<sub>0.1</sub>RGO<sub>0.9</sub>/PDMS under the -10% strain (Figure 5.4(a)), the G-band peak is shifted to the larger wavenumber (inferring compression) from to the zero-strain peak position. Similarly, under the ~50% tensile strain, the G-band peak is shifted to the smaller wavenumber (inferring lattice tension). This is surprising because MWNT<sub>0</sub>RGO<sub>1</sub>/PDMS (Figure 5.3(b-2)) showed the opposite trend. Indeed it is intriguing that for MWNT<sub>0.1</sub>RGO<sub>0.9</sub>/PDMS, the Raman signature completely changed signs from compression to tension. Figure 5.3(b) presents the wavenumber change versus the strain for the samples. An increase of 4 cm<sup>-1</sup> in wavenumber was observed under 10% compression and a decrease of ~8 cm<sup>-1</sup> decrease in wavenumber was observed under 50% tension.

Figure 5.4(c) presents the Raman peak shift in wavenumber as a function of the relative weight ratio of MWNT in the binary filler measured under the 50% uniaxial tension. Positive wavenumber change was observed for 0-0.01 wt. % of MWNTs in the binary filler. It suggests on average compression dominates the RGO lattice under uniaxial tension, similar to results in Figure 5.3 (pure 1 wt. % RGO/PDMS). For ~0.1 wt. % MWNTs in the binary filler, a negative wavenumber change was observed, suggesting that a net tension is built on the lattice under the applied tensile strain. The complete reversal in the wavenumber change with a small change of the relative ratio of MWNTs in the binary filler suggests synergy between RGO and MWNTs.

Further increase of the relative ratio of MWNTs does not change the sign of the wavenumber change, namely, the samples are under tension. When the relative weight ratio of MWNTs is between 80% to 100%, the wavenumber change is saturated. The total change in wavenumber is  $\sim 20 \text{ cm}^{-1}$  per 0.1 wt. % MWNT, or  $200 \text{ cm}^{-1}/\text{wt. \%}$ . This rate is quite remarkable transformation of the Raman signal given the small weight fractions used.

A plausible mechanism of how MWNTs aids in limiting deformation of RGO in the direction of applied strain has been suggested. Without any MWNTs, the collective Raman signature of  $\text{MWNT}_0\text{RGO}_1/\text{PDMS}$  is one of compression. This was also seen in the recent report on the FLG/polymer composites [34]. The mobile large chain PDMS network in the direction of applied strain can lead to compressive force on RGO resulting in net Raman peak shift for compression [34]. The earlier understanding was that the

tension along one direction can cause the graphene plate to compress along the perpendicular direction. This may be possible for the case under small strain. The more plausible mechanism is that wrapping of the polymer chains around RGO can make it fold, thereby causing RGO to compress. The D-band of RGO/PDMS may suggest folding of the RGO lattice where the fold can appear as a defect center for scattering [196]. One or more foldings of the RGO sheet can thus exert a net compressive stress on the RGO lattice.

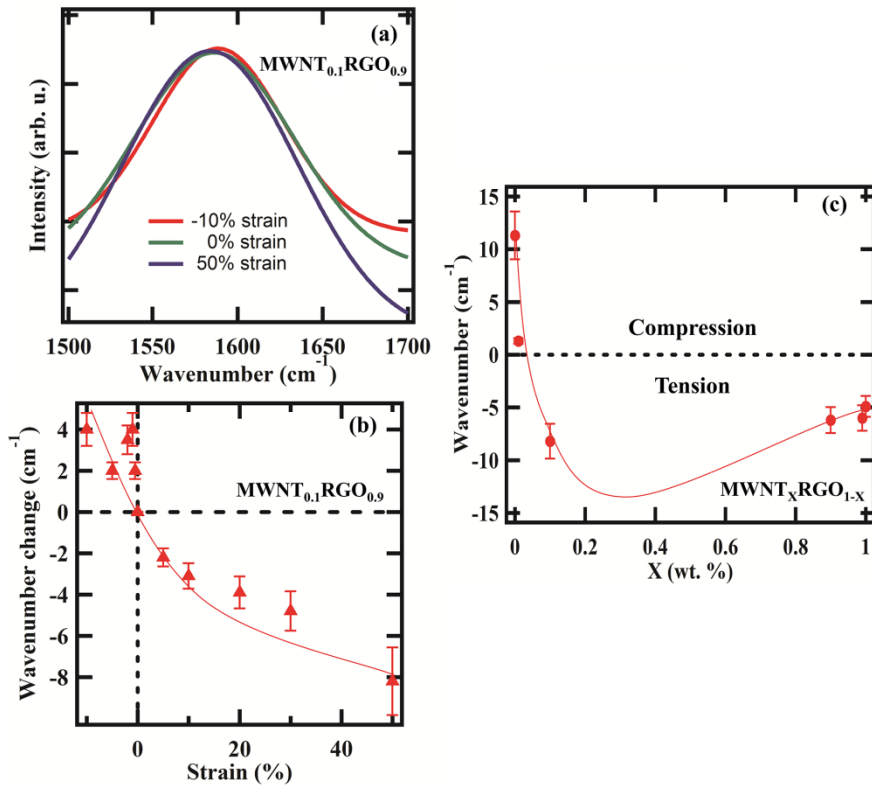


Figure 5.4 Load transfer (G-band) in RGO<sub>0.9</sub>MWNT<sub>0.1</sub>/PDMS: (a) the Raman intensity versus wavenumber; (b) the change of the Raman peak in wavenumber as a function of the strain; and (c) the Raman peak shift in wavenumber versus the relative weight fraction of nano-carbons under 50% uniaxial tension.

Stretching the polymer sample leads to an increase of the potential energy in the sample. Therefore, the elastic free energy, which is also called the Helmholtz free energy ( $A = U - TS$ ), of the sample should increase [226]. Since the internal energy ( $U$ ) and temperature ( $T$ ) of the polymer system are both assumed to remain constant, the entropy ( $S$ ) of the system must decrease. This qualitatively makes sense as well, as stretching the sample results in polymeric chains going from a high entropically disordered state (unstrained configuration), to a low entropically ordered state (strained configuration) [226]. Assume the entropy of the system to equal  $S = S_0 + k \cdot \ln[W(r)]$ , where  $S_0$  is the initial entropy,  $k$  is the Boltzmann constant, and  $W(r)$  is the density distribution of the end-to-end polymeric chains [226]. Substituting these results into  $A$ , the  $A = U - T(S_0 + k \cdot \ln[W(r)])$ . In other words, the elastic free energy is dependent on the density distribution of the end to end polymeric chains. Assuming that the polymeric chain length follows a Gaussian distribution, the density distribution is the number of configurations allowable to the polymeric chain. Shorter chains result in a stiffer polymer [226].

While the mechanism of molecular reinforcement is poorly understood [226], we believe that the addition of the two carbon nanostructures to the polymer results in different polymeric chain/carbon configurations. Because of the 2D mesh-like structure of RGO, it is likely that the polymer chains can be entangled in the mesh or warp around RGO. The polymer chains wrapping around the RGO can fold the RGO or make the lattice go to a net compressive state which is seen in the Raman data. CNTs however, likely present a different mechanism for shortening the polymeric chains. Because of the high aspect ratio, 1D CNTs likely present opportunities for polymeric chains to become much more entangled along the axis of the nanotube. The CNTs cannot fold as the

RGO's and therefore always remain in tension on application of uniaxial tension. Therefore, for the same wt. % additive, CNT/PDMS composites should be stiffer than RGO/PDMS composites, which have been confirmed experimentally by our results in the next section. The expression for the true strain can therefore be written as  $\tau_x = V^{-1} \lambda_x \sum_{i=1}^3 (\partial \Delta A_{el} / \partial \lambda_i^2) \partial \lambda_i^2 / \partial \lambda_x$  and can be evaluated for the  $x$ ,  $y$  and  $z$  dimensions [226]. The shorter polymeric chains due to the CNTs could result in limiting the strain in the  $x$  and  $y$  directions (assuming uniaxial tension is applied in the  $z$  direction). Since the chains are polymerized from inside by NIR illumination, the effective segmental length must decrease with the addition of MWNT or making it stiffer. The entanglement of the MWNT onto the RGO as the SEM suggest can also make the net polymeric chain length shorter during the polymerization process. [226]. The shorter polymeric chains due to the CNTs could result in limiting the strain in the  $x$  and  $y$  directions (assuming uniaxial tension is applied in the  $z$  direction). Since the chains are polymerized from inside by NIR illumination, the effective segmental length must decrease with addition of MWNT or making it stiffer. The entanglement of the MWNT onto the RGO as the SEM suggest can also make the net polymeric chain length shorter during the polymerization process.

#### 5.2.4 Orientational ordering: A 2D model

Another factor that may affect the load transfer is the orientational order of the nano-carbons in the presence of strain. By using nanotube as an example, we developed a 2D model to calculate the change in the angular orientation of the nanotube with shift in Raman wavenumbers. Orientation of the nanotube should play an important role in load

transfer. When a uniaxial tensile strain is applied to MWNT/PDMS composite, the MWNT will align itself or undergo change in orientation in the direction of the strain. This has been shown to improve photomechanical stresses in the past for actuation applications [218, 219]. Figure 5.5 presents the shift in Raman wavenumbers (measured) versus the orientational angle (calculated) of the CNTs. The calculation is based on the model that describes the movement of a rigid rod in polymer matrix as shown in Figure 5.5(a). The average change in the angular orientation of the nanotube in polymer matrix can be written as:

$$\langle \Delta\theta \rangle = \int_0^{\frac{\pi}{2}} \arctan\left(\frac{\delta_{x'}}{L}\right) P(\theta_0) d\theta_0$$

where  $\delta_{x'} = \delta_y \cdot \sin\theta_0 + \delta_x \cdot \cos\theta_0$ , is the change in length in the  $x'$  axes on change in orientation of the nanotube in the presence of uniaxial tension;  $\delta_y = \varepsilon_y \cdot d$ ,  $\delta_x = \nu \cdot \varepsilon_y \cdot a$ ,  $P(\theta_0)$  is the orientational probability distribution of the nanotube and this is a flat distribution of  $\frac{1}{\pi/2}$ . The change in the orientational angle can therefore be calculated based on the applied uniaxial tensile strain using the above equation.

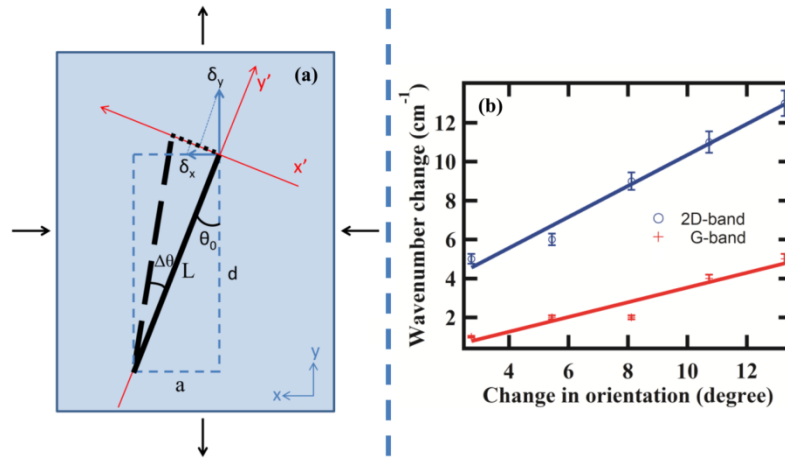


Figure 5.5 (a) Model describing the change in orientation of the nanotube in polymer on application of a uniaxial tensile strain, (b) the change in Raman

**wavenumbers for G and 2D band (measured) versus change in orientation angle (calculated) for different uniaxial tensile strains applied to the sample.**

Figure 5.5(b) presents the shift in Raman wavenumbers versus the calculated change in orientation angles using the above model. Surprisingly a linear relationship is established between the calculated angles and the actual measured Raman values. The linear relationship between the orientation angle and the Raman wavenumber shift for both the G and 2D band suggest that the load transfer is closely related to the orientation ordering of CNTs in the matrix.

For RGO, similar angle change can be expected if it is treated as a rigid 2D sheet on a 2D plane. However, for the mixtures, a 3D model might be required to take into account the entanglement of CNTs between 2 RGO plates as observed in the SEM images. This is beyond the scope of the PhD work and future atomistic modeling may reveal the actual synergy between the nano-carbons and how the orientation of the nano-carbons affects the synergy. Nevertheless, the model described here gives some insights into the change in the Raman wavenumber as a function of the calculated orientation angle.

In principle, such change in the Raman wavenumber with the orientation angles could be useful for design of nanoelectronic devices based on strains. Furthermore, under uniaxial tension 1D MWNT are better reinforcers compared to 2D RGO sheets in polymer composites. The single dimensionality and high strength of the nanotubes can be expected to exhibit much higher load transfer along the axial direction compared to 2D RGO sheets in tension.

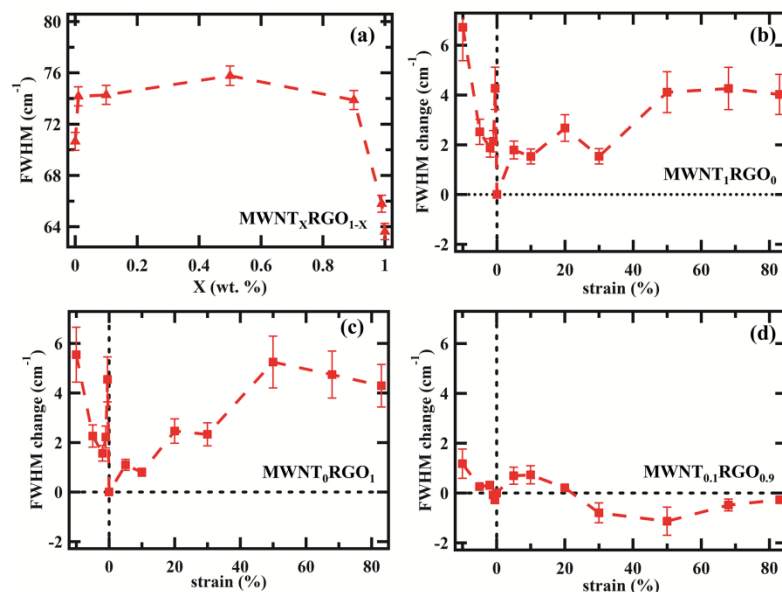


**Figure 5.6** The Full Width Half Maximum (FWHM) data for the different compositions of MWNT<sub>x</sub>RGO<sub>1-x</sub>/PDMS: (a) the FWHM versus weight fraction of the nano-carbon; (b) the FWHM change versus percentage strain for MWNT<sub>1</sub>RGO<sub>0</sub>/PDMS; (c) the FWHM change versus strain for MWNT<sub>0</sub>RGO<sub>1</sub>/PDMS; and (d) the FWHM change versus strain for MWNT<sub>0.1</sub>RGO<sub>0.9</sub>/PDMS.

Investigating further, the Full Width Half Maximum (FWHM) of the G peak could indicate the measure of the stress distribution of the nano-carbon in the composite. Slippage is expected due to the high level of strains used in these experiments and the viscoelastic nature of the polymer. It should be noted that the past reports on load transfer of nano-carbon composites using Raman spectroscopy has investigated only limited uniaxial tension and compression ( $\pm 20\%$ ) [19, 161-168]. Figure 5.6(a) presents the FWHM versus weight fraction of the nano-carbon. The FWHM is almost a constant for all the weight fractions of the binary mixtures in PDMS under zero strain. Figure 5.6(b) presents the change in FWHM versus strain for MWNT<sub>1</sub>RGO<sub>0</sub>/PDMS sample. Smaller change in a FWHM means uniform stress distribution and no slippage on applied tension or compression. In Figure 5.6(b) one can see change in FWHM of almost 6 cm<sup>-1</sup> from 10%

compression to the unstrained state. The FWHM change data in tension is better ( $4 \text{ cm}^{-1}$ ) suggesting less slippage in tension and more uniform stress distribution achieving saturation in the values with increasing strain. One can see that the FWHM change is almost constant between -5% to 30% at  $2 \text{ cm}^{-1}$  suggesting uniform load transfer at these strain values. Figure 5.6(c) presents the FWHM change versus strain for  $\text{MWNT}_0\text{RGO}_1/\text{PDMS}$  sample. Similar trends are seen here in compression accompanied by slippage and in tension more uniform stress distribution. Although we see values of  $6 \text{ cm}^{-1}$  for FWHM change in compression, it should be noted that the change in FWHM is less than  $\sim 10\%$  of the actual FWHM values ( $74 \text{ cm}^{-1}$ ) presented in Figure 5.6(a). Therefore, this is not a significant effect and load is still transferred in compression more than in tension. Figure 5.6(d) presents the FWHM versus strain for the synergistic mixture  $\text{MWNT}_{0.1}\text{RGO}_{0.9}/\text{PDMS}$ . This sample shows that the FWHM is almost constant in both uniaxial compression and tension. The FWHM change is seen to be reduced by 3 times (from  $6 \text{ cm}^{-1}$  change in FWHM for  $\text{MWNT}_0\text{RGO}_1/\text{PDMS}$  to  $2 \text{ cm}^{-1}$  change for  $(\text{MWNT}_{0.1}\text{RGO}_{0.9})/\text{PDMS}$ ). This is only  $\sim 2.7\%$  of the actual FWHM values and can be practically considered as no slippage. The change in FWHM in tension for all strains is almost zero suggesting no slippage and stress distribution remaining constant throughout the matrix or the same as un-strained sample. The use of binary nano-carbons therefore minimized slippage and made the stress distribution constant throughout with narrow FWHM change. This can only happen if the effective segmental chain is reduced and severe entanglement of MWNT and RGO with the polymeric chains giving the chains limited extensibility. It should be noted that even the  $6 \text{ cm}^{-1}$  values of the FWHM change

for pure samples is still narrow (<10%) suggesting uniform load transfer and minimum slippage in both compression and tension.

### 5.2.5 Mechanical properties of binary nano-carbon/PDMS composites

**Table 5.1 Synergistic effects in Young's modulus of MWNT<sub>x</sub>RG0<sub>1-x</sub>/PDMS composites**

Composite	Young's modulus (MPa)	Young's modulus change
PDMS	0.96 ± 0.03	0
MWNT <sub>1</sub> RG0 <sub>0</sub> /PDMS	1.72 ± 0.04	76%
MWNT <sub>0.99</sub> RG0 <sub>0.01</sub> /PDMS	1.56 ± 0.05	63%
MWNT <sub>0.9</sub> RG0 <sub>0.1</sub> /PDMS	1.49 ± 0.04	55%
MWNT <sub>0.5</sub> RG0 <sub>0.5</sub> /PDMS	1.57 ± 0.03	64%
MWNT <sub>0.1</sub> RG0 <sub>0.9</sub> /PDMS	1.95 ± 0.06	103%
MWNT <sub>0.01</sub> RG0 <sub>0.99</sub> /PDMS	1.87 ± 0.05	94%
MWNT <sub>0</sub> RG0 <sub>1</sub> /PDMS	1.19 ± 0.02	26%

The Raman results on the enhanced load transfer and the synergistic effects in binary nano-carbon mixtures are also supported by the measurements of elastic moduli. Table 5.1 presents the measured Young's modulus values of pure PDMS, MWNT<sub>1</sub>RG0<sub>0</sub>/PDMS, MWNT<sub>0.99</sub>RG0<sub>0.01</sub>/PDMS, MWNT<sub>0.9</sub>RG0<sub>0.1</sub>/PDMS, MWNT<sub>0.5</sub>RG0<sub>0.5</sub>/PDMS, MWNT<sub>0.1</sub>RG0<sub>0.9</sub>/PDMS, MWNT<sub>0.01</sub>RG0<sub>0.99</sub>/PDMS and MWNT<sub>0</sub>RG0<sub>1</sub>/PDMS. Young's modulus values were measured to be ~ 0.96 MPa ± 0.03 for pure PDMS, ~1.72 MPa ± 0.04 for MWNT<sub>1</sub>RG0<sub>0</sub>/PDMS, ~1.19 MPa ± 0.03 for

MWNT<sub>0</sub>RGO<sub>1</sub>/PDMS and finally  $\sim 1.95 \text{ MPa} \pm 0.06$  for MWNT<sub>0.1</sub>RGO<sub>0.9</sub>/PDMS. Table 5.1 also presents change in Young's modulus for all the samples.

An impressive increase of  $\sim 103\%$  in Young's modulus was observed in the binary-nano-carbon sample compared to the pristine polymer. By comparison, the Young's modulus value increase of MWNT<sub>0</sub>RGO<sub>1</sub>/PDMS was only  $\sim 26\%$  compared to the pristine polymer. This may be due to the defects, kinks and folding of RGO in the polymer that lowers the Young's modulus values in tension. The change in Young's modulus value for all the other mixtures are reported to be 55 - 94%. It is seen that with increasing relative weight ratio of MWNT, the change in Young's modulus increases, reaches a maximum, and then decreases again. It suggests that the synergy is optimized  $\sim 0.1$  wt. % of MWNT. Because the Young's modulus values were measured under tension, compressive deformation of RGO due to folding could lower the increase in Young's modulus. Adding small amounts ( $\sim 0.1$  wt. %) of MWNTs limits this deformation and therefore increases the Young's modulus value of almost  $\sim 4$  times. This means, adding small amounts of MWNT must make the effective segmental chain length smaller due to severe entanglement and lead to stiffer RGO/PDMS matrix. In other words, MWNTs limit deformation of RGO, enabling larger load transfer in tension, minimum slippage and enhanced Young's modulus values.

#### 5.2.6 Halpin-Tsai model for predicting Young's modulus of composites

Investigating further, one can develop a simple model to predict the change in Young's modulus of the composites based on the rule of mixtures and the Halpin-Tsai

equations as shown in the past [227]. Using simple rule of mixture approach, we predict the Young's modulus of the MWNT<sub>x</sub>RGO<sub>1-x</sub>/PDMS composites by assuming the composite to be an isotropic and elastic matrix filled with binary nano-carbons. In the case of rule of mixtures, it is assumed both RGO and MWNT are well bonded and homogenously dispersed. The strain is assumed to be the same and equally distributed in both the nano-carbons. The Young's modulus of RGO is ~250 GPa [45], MWNT is ~300 GPa [228] and PDMS is 0.96 MPa (measured). The Young's modulus of the composite using rule of mixtures can be written as:

$$E_m = (\eta_o \eta_l \cdot E_{MWNT} - E_{PDMS}) \cdot w_{MWNT} + (\eta_o \eta_l \eta_f \cdot E_{SLG} - E_{PDMS}) \cdot w_{SLG} + E_{PDMS}$$

$\eta_o$  is orientation efficiency factor,  $\eta_l$  is the length efficiency factor and  $\eta_f$  is the topological efficiency factor. Since RGO can undergo folding or change in topology, this may affect the eventual Young's modulus values and therefore is quite reasonable to have such efficiency factors. The  $\eta_l$  is the length efficiency factor is described by the equation:

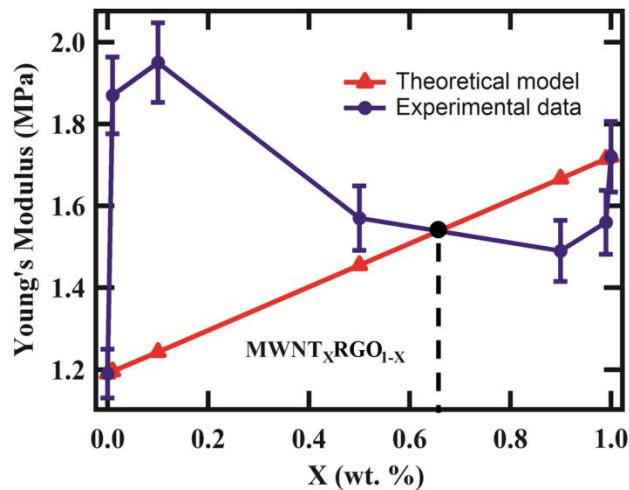
$$\eta_l = 1 - \frac{\text{Tanh}(a \cdot L/D)}{a \cdot L/D}$$

where  $a$  can be described as:

$$a = \sqrt{\frac{-3 \cdot E_{PDMS}}{2 \cdot E_{carbon} \cdot \ln(w_{carbon})}}$$

The length efficiency factor approaches unity as  $aL/D$  becomes large. This suggests that high aspect ratio fillers give better Young's modulus values. Since the Young's modulus values of the both MWNT<sub>1</sub>RGO<sub>0</sub>/PDMS and RGO<sub>1</sub>MWNT<sub>0</sub>/PDMS are known, these experimental values can be used in these theoretical equations to arrive

at L/D and L/W values. The L/D for MWNT was calculated as  $\sim 61$  and for RGO L/W of  $\sim 10$  was used [229]. Assuming RGO to be rolled out CNT, and setting  $D = W/\pi$ , gives us L/D for RGO = 31.4. In both cases the L/D values of  $>10$  underscores that both MWNT and RGO are good choices as reinforcers for polymer composites. The orientation efficiency factor is assumed to be 0.2 for randomly aligned fibers and the topological efficiency factor  $\eta_f$  is suggested to be 0.9. The topological efficiency factor assumes that RGO retains most of its plate like configuration and the defects are quite small. As the number of defects increase, the  $\eta_f$  value will decrease. One can develop a relationship between defect density and topological efficiency that could be included in the model for future calculations. Further, a relationship could be developed based on the Raman D band changes that can predict the topological efficiency more accurately depending on the defects, folds, kinks and doping. However, such complex model is beyond the scope of the current PhD work.



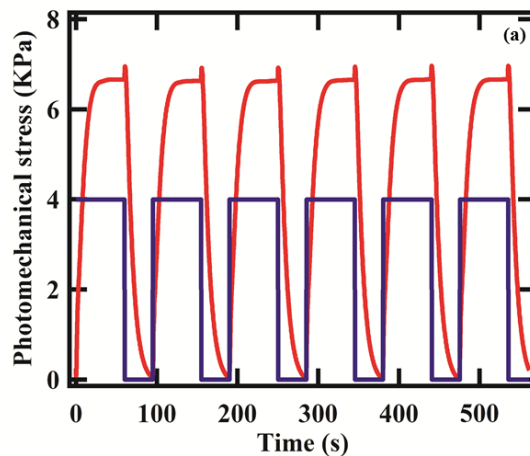
**Figure 5.7** The Young's modulus versus weight percentage of nano-carbon filler for MWNT<sub>x</sub>RGO<sub>1-x</sub>/PDMS composite calculated using the rule of mixtures and compared to the experimental data.

Figure 5.7 presents the Young's modulus of the  $MWNT_xRGO_{1-x}/PDMS$  versus weight fraction of the nano-carbon using the above described theoretical model. The actual experimental data is also plotted for comparison. A linear relationship is established for the Young's modulus of the composite with different fractions of MWNT and RGO. However, looking at the experimental values, the model cannot accurately predict the synergy between 2 nano-carbons. There is a cross-over point shown in dotted lines where the model and the experimental values agree at 0.5-0.7 wt. % MWNT or equal mixtures. There are several reasons why the model does not accurately agree with the experimental values. The model cannot predict events such as folding of graphene sheets, dimensionality of the sheets affecting mechanical strength and how MWNT may be bridging between 2 graphene sheets thereby eliminating the compressive deformation. While, these physical events are reflected in the Raman data, highly sophisticated atomistic simulations are needed to predict events such as synergy which is beyond the scope of this PhD work. This also suggest that simple models that were previously used to predict the mechanical properties of single nano-carbon fiber in polymer composites cannot be fully extended to the use of 2 nano-carbons if there is synergy between the nano-carbons. Nevertheless, the theoretical equation above is still quite useful for predicting the Young's modulus of the composite with 2 nano-carbons where synergy may not be involved (Ex: nano-carbons of the same dimensional states but different elastic properties such as CNT and carbon nano-fiber). The experimental results show that use of 2 nano-carbons is better than one nano-carbon and that could be a fundamental basis on which both the model and experimental data agree. Again, it should be made

clear that synergy may only be observed with 2 nano-carbons of different dimensional states in polymer composites.

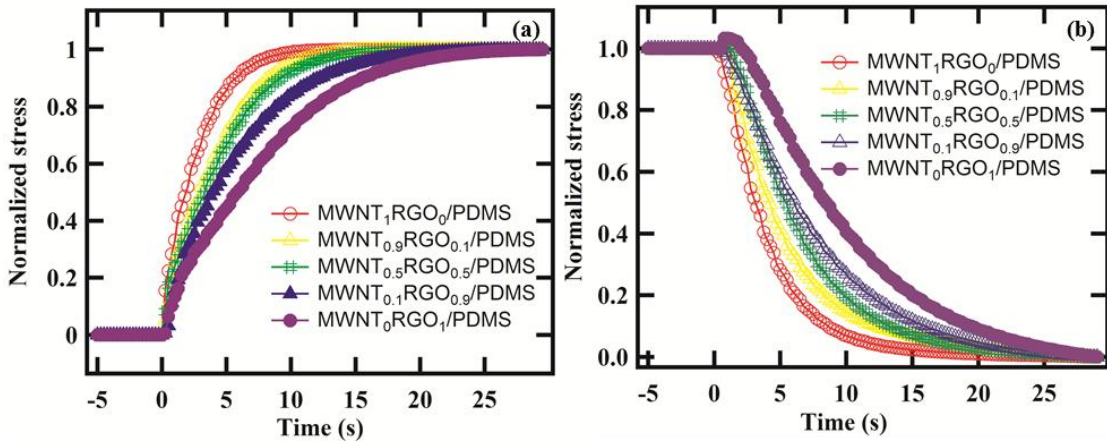
### 5.2.7 Photomechanical responses of binary mixture nano-carbons/PDMS composites

In recent years, there has been increasing number of studies on the use of nano-carbon/ elastomers for photomechanical actuation. NIR light induced stimuli responsively has been demonstrated in nanotube/polymer, GNP/polymer, and RGO/polymer composites [51, 79, 216-219, 230]. Such photomechanical studies on nano-carbon/elastomers have led to applications such as MEMS based micro-actuators, micro-grippers, micro-mirrors and nano-positioners [220-222, 231]. Therefore, as an application to actuation, binary nano-carbon/elastomer composites were explored as photomechanical actuators.



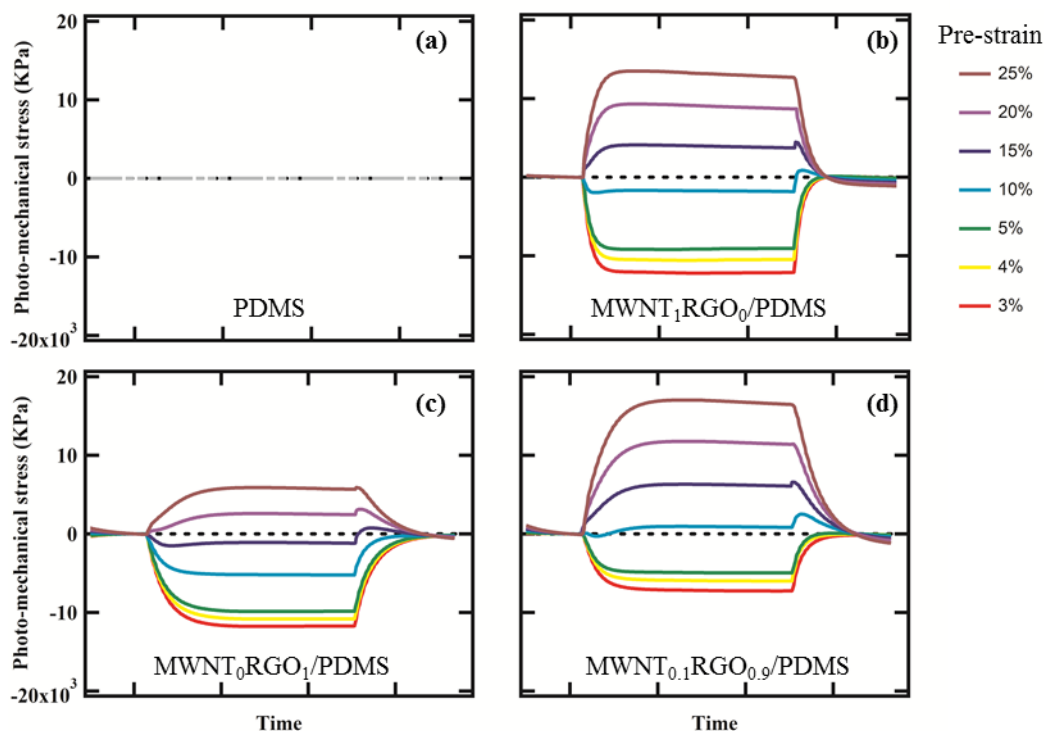
**Figure 5.8** The photo-mechanical responses and the actuation stress response of binary mixture nano-carbons polymer composites actuator for 15% pre-strain.

Figure 5.8 shows the photomechanical actuation and relaxation kinetics during a 15% pre-strain test. The test composites undergoes five cycles of NIR illumination on for 60 s, followed by NIR illumination off for 30 s. The magnitude of actuation is highly repeatable for each test sample (See details in Appendix C).



**Figure 5.9 (a) Actuation and (b) relaxation of the binary mixture nano-carbons polymer composites actuator**

Figure 5.9 shows the experimental actuation and relaxation of MWNT<sub>x</sub>RGO<sub>1-x</sub>/PDMS. MWNT<sub>1</sub>RGO<sub>0</sub>/PDMS sample shows significantly fast actuation and relaxation response compared to MWNT<sub>0</sub>RGO<sub>1</sub>/PDMS and other binary mixture composites due to highly interconnected network of CNTs.



**Figure 5.10** The comparison of increasing photomechanically induced stress change in binary mixture nano-carbons polymer composites actuator as a result of NIR illumination: (a) plain PDMS; (b) MWNT<sub>1</sub>RGO<sub>0</sub>/PDMS; (c) MWNT<sub>0</sub>RGO<sub>1</sub>/PDMS; (d) MWNT<sub>0.1</sub>RGO<sub>0.9</sub>/PDMS.

Figure 5.10 illustrates the steady-state photomechanical actuation of pure PDMS, MWNT<sub>1</sub>RGO<sub>0</sub>/PDMS, MWNT<sub>0</sub>RGO<sub>1</sub>/PDMS, and MWNT<sub>0.1</sub>RGO<sub>0.9</sub>/PDMS. These plots show the photomechanical response from 3% to 25% pre-strains. From figure 5.10(a), pure PDMS actuator shows negligible response because of its optical loss for NIR illumination. However, by a concentration of 1 wt. % nano-carbon, the photomechanical response becomes clearly observable. All the composites exhibit that low pre-strain values result in expansion while high strain values result in compression. Some interesting results were observed here: MWNT<sub>0</sub>RGO<sub>1</sub>/PDMS sample shows lower contraction stress than MWNT<sub>1</sub>RGO<sub>0</sub>/PDMS sample under high strains, by adding 0.1 wt. % MWNT/PDMS to 0.9 wt. % RGO/PDMS, the contraction stress is much higher

than single nano-carbon polymer composites. Under 10% strain, both MWNT<sub>1</sub>RGO<sub>0</sub>/PDMS and MWNT<sub>0</sub>RGO<sub>1</sub>/PDMS show expansion stress, however binary MWNT<sub>0.1</sub>RGO<sub>0.9</sub>/PDMS shows contraction stress. The balance strain, which means no photomechanical force, for the binary nano-carbon/PDMS moves to smaller pre-strain than the value of MWNT/PDMS and RGO/PDMS.

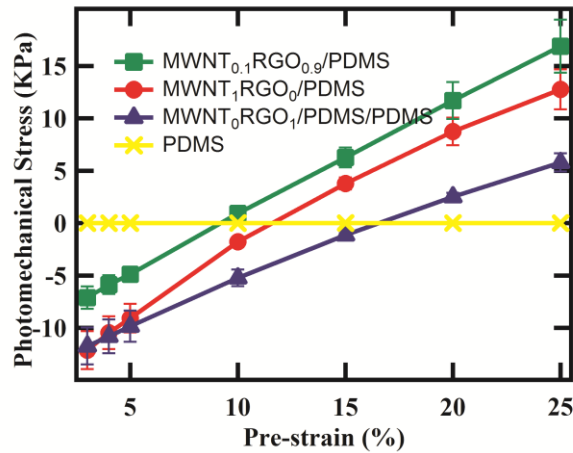


**Figure 5.11 The average photomechanically response versus the pre-strain of binary mixture nano-carbons polymer composites actuator with different weight ratio**

Overall, binary nano-carbons polymer actuator shows lower expansion stress under lower pre-strain and higher contraction stress under higher pre-strain than single nano-carbon polymer actuator.

Looking forward, the synergy between two or more nano-carbon fillers could enhance load bearing capability, limit deformation, and improve the mechanical properties of polymer composites. Graphene is a 2D structure and therefore entanglement of the polymer during the mixing process can result in folding of the lattice thereby exerting a net compressive stress. This could mean reduced/increased overall mechanical properties depending on tension/compression. Small amount of MWNTs entangled in

RGO during mixing and subsequent polymerization reduced the chain length and eliminated the folding of RGO completely. The method of using NIR polymerization as reported here could also be useful in improving the interfacial shear strength and the mechanical properties of nano-composites. While surface chemical functionalization of nanotubes/graphene are quite attractive for better interaction with polymers, recent reports have shown that improvement in interfacial adhesion due to surface functionalization of nanotubes does not always promote substantial improvement in mechanical properties [171]. This is due to surface degradation of nanotubes/graphene during functionalization. Realization of advanced mechanical properties in graphene based composites may depend on the extent to which folding of the RGO can be minimized in polymers.

### **5.3 Conclusion**

In conclusion, this chapter reports how synergy is achieved in binary nano-carbon mixtures using Raman spectroscopy. Significant shifts in the *G*-bands were observed both in tension and compression for single as well as binary nano-carbon mixtures in polymer composites. Addition of small amounts of MWNT (~0.1 wt. %) dispersed in RGO (0.9 wt. %)/PDMS samples reversed the sign of the change of the Raman wavenumber from positive to negative values demonstrating the complete reversal of lattice stress. A wavenumber change from  $10\text{ cm}^{-1}$  in compression to  $10\text{ cm}^{-1}$  in tension was observed for MWNT<sub>0.1</sub>RGO<sub>0.9</sub>/PDMS under applied uniaxial tension. MWNTs limited the deformation of RGO in one direction by providing limited extensibility to the chains and

thereby improving the Young's modulus by ~103% compared to the pristine polymer. Such impressive results suggest the cooperative action of two nano-carbon fillers is better than single nano-carbon for better interfacial strength, mechanical properties and load transfer. The synergy between 2 nano-carbons in polymer materials could be highly useful in the development of sensors, actuators, and in general mixed dimensional systems based on carbon [216]. Higher photo-mechanical response under high strain and lower photo-mechanical response under low strain are also shown for mixture nano-carbons/polymer composites compared with pure nano-carbon/polymer composites under high tension strain.

## CHAPTER 6 THE MECHANISM OF NEAR INFRARED PHOTON-ASSISTED POLYMERIZATION

### 6.1 Introduction

As discussed in the earlier chapters, we developed the NIR photon-assisted polymerization method and used it successfully to synthesize carbon-nanotube/polymer [173], RGO/polymer, GNP/polymer, and binary nano-carbons/polymer composites [232]. This method was shown to enhance the interfacial connection between the nano-carbons and the polymer matrix. For example, as discussed above, under compression the measured large shift of the Raman G'-band peak demonstrated high interfacial shear stress and load transfer to the nano carbon. The measured stress-strain curves on the nano-carbon composites prepared by the NIR photon-assisted polymerization method also showed higher toughness than those with the conventional baking method.

This method is based on photothermal heating. Nanoscale materials, such as nanotubes [47, 49], graphene [233-235], nanoshells [236-238] and other nanoparticles [239, 240], are known to efficiently absorb NIR light and induce photothermal heating. Such photothermal heating effect was demonstrated on RGO using a photographic flash camera [241], and it was used to reconstruct the entire surface of CNTs into nano-horns to enhance drug delivery [242], for photodynamic therapy [243], photo-thermal actuators [79, 217] and even photo-thermal therapy to kill cancer cells *in vivo* [234]. However,

light induced heating may not be the only mechanism of enhanced interfacial shear strength and associated increase in mechanical properties. Nano-carbons such as RGO are known to have several chemical groups such as carboxyl, hydroxyl, carbonyl and other C-O groups on its surface. Further, defects such as dangling bonds in graphene can also enhance interaction with the polymer.

In this chapter, we investigate the mechanisms using X-ray photoelectron spectroscopy first to probe the chemical groups of nano-carbons and next to examine the chemical bonds at the interface. We show that using NIR mediated polymerization of nano-carbons dispersed inside the polymer causes internal oxidation of the nano-carbon/polymer interface. For example, for the RGO/PDMS composites, it activated the –OH/=O groups on the RGO and opens the carbon-carbon double bonds of the PDMS oligomer, thereby assisting in the formation of C-O bonds between the PDMS matrix and the graphene filler. High absorption of NIR photons causes the free radical reaction between the –SiH group on the PDMS crosslinker and the hydroxyl/carbonyl groups on the RGO. The increase in C-O and Si-O bonds was confirmed by XPS and is directly correlated to the overall improvement in the mechanical properties for these composites.

## **6.2 Results and discussions**

Homogenous dispersion of 1 wt. % MWNT and graphene (RGO or GNP for comparison) in PDMS was prepared (See details in APPENEDIX B). The XPS measurements were performed on a MultiLab 3000 VG Thermo Scientific surface analysis system. Mg K $\alpha$  (1253.6 eV) radiation was used as the excitation source and the

measurements were performed at room temperature and under the ultra-high vacuum (UHV) condition with the pressure in the  $10^{-9}$  Torr range. Charging of the samples was corrected by setting the binding energy of the adventitious carbon (C 1s) at 284.6 eV. The PASS energy for scanning was set as 50 eV. Gaussian profile was used to fit the XPS peaks in XPSPEAK software. For each nano-carbon/PDMS composite, a set of five different samples were studied. An AQ-6315A optical spectrum analyzer (Ando) was used to measure the spectrum profile of the halogen lamp, an NIR light source.

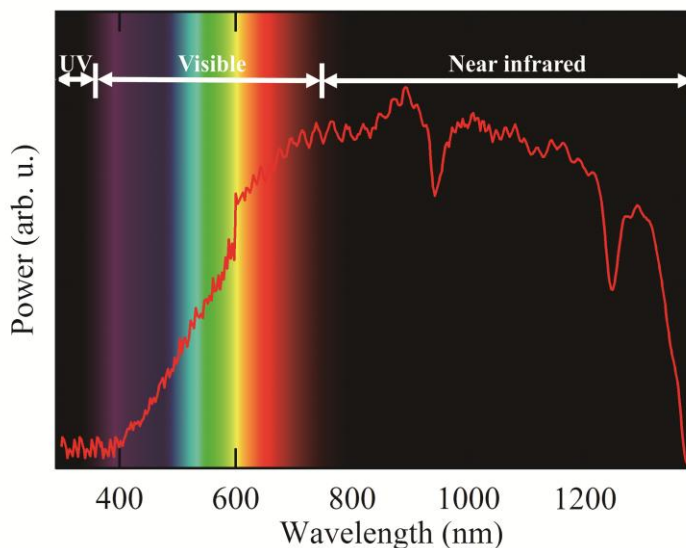


**Figure 6.1** The spectrum profile of halogen lamp with UV filter

The spectral profile produced by Halogen lamp with UV filter is presented in Figure 6.1. The halogen lamp shows high energy density in NIR range between 650 nm to 1400 nm. The spectrum of halogen lamp shows that it can be used as the NIR photon source to polymerize nano-carbon composites.

## 6.2.1 XPS characterization of nano-carbons (1D MWNT, 2D RGO, 3D GNP)

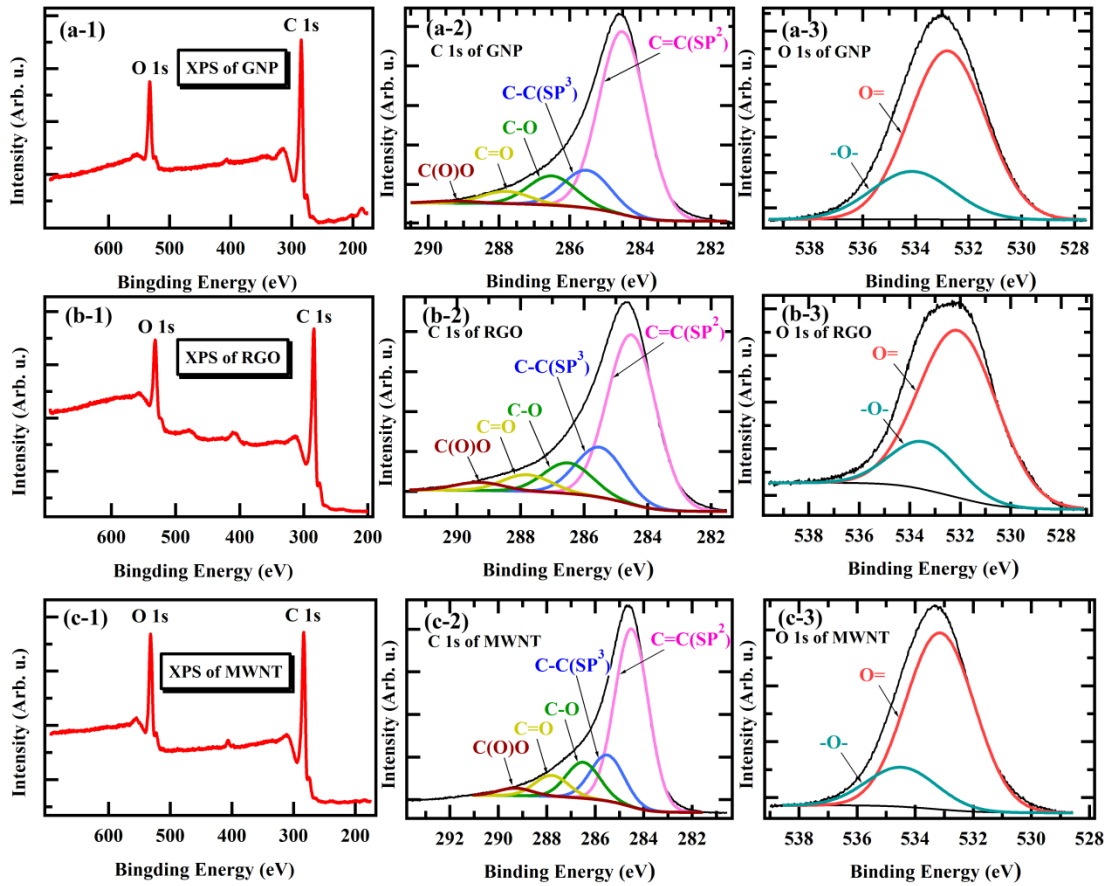


**Figure 6.2** The XPS spectra of (a-1) GNP, (b-1) RGO, and (c-1) MWNT; C 1s binding energy of (a-2) GNP, (b-2) RGO, and (c-2) MWNT; O 1s binding energy of (a-3) GNP, (b-3) RGO, and (c-3) MWNT.

Using XPS, we first investigated the MWNTs, GNPs and RGO in order to understand the surface chemical groups and morphology of the nano-carbon fillers. The XPS spectra of the MWNT, GNP and RGO fillers are shown in Figures 6.2(a-1), 6.2(b-1), and 6.2(c-1), respectively. The fittings of their corresponding C1s peaks are shown in Figures 6.2(a-2), 6.2(b-2), and 6.2(c-2), respectively. The fittings of their corresponding O1s peaks are shown in Figures 6.2(a-3), 6.2(b-3), and 6.2(c-3), respectively. The curve fittings of the C1s and O1s peaks were performed using Gaussian peak shapes for

different carbon and oxygen bonding groups after performing the Shirley background correction.

From Figures 6.2(a-2), 6.2(b-2), and 6.2(c-2), the fitted ratio and binding energy for different carbon bonding groups are summarized in Table 6.1 for MWNT, GNP and RGO. The binding energy of C1s is assigned to 284.5 eV in the  $\underline{\text{C}}=\text{C}$  bond, 285.5 eV for the  $\underline{\text{C}}-\text{C}$  bond, 286.5 eV for the  $\underline{\text{C}}-\text{O}$  bond, 287.8 eV for the  $\underline{\text{C}}=\text{O}$  bond, and 289.3 eV for the  $\underline{\text{C}}(\text{O})\text{O}$  bond. The highest percentage of the  $\underline{\text{C}}-\text{C}$  ( $\text{sp}^2$ ) bond, ~ 69.2%, is found in GNP, compared to 61.7% in MWNT and 61.6% in RGO. The high percentage of the  $\text{sp}^3$  carbon, ~18.2%, is found in RGO, likely due to hydrogen reduction of the GO. The percentages of the C-O, C=O, and C(O)O bonds are higher in RGO and MWNTs than in GNP. It infers larger amounts of OH, COOH, and C=O in MWNT and RGO, indicating the existence of more functional groups.

**Table 6.1 The fitted ratio and the binding energy of all the carbon bonding groups in the MWNT, RGO and GNP fillers**

Carbon	Binding energy (eV)	MWNT	RGO	GNP
$\underline{\text{C}}=\text{C}$ ( $\text{sp}^2$ )	284.5	61.7%	61.6%	69.2%
$\underline{\text{C}}-\text{C}$ ( $\text{sp}^3$ )	285.5	15.9%	18.2%	14.3%
$\underline{\text{C}}-\text{O}$	286.5	12.5%	11.1%	11.1%
$\underline{\text{C}}=\text{O}$	287.8	7.3%	6.1%	4.6%
$\underline{\text{C}}(\text{O})\text{O}$	289.3	2.6%	3.0%	0.8%

The information obtained by fitting the O1s peaks in Figures 6.2(a-3), 6.2(b-3), and 6.2(c-3) can complement the data from the C1s peaks. Because the O1s peaks is surface specific due to the reduced kinetic energy and sampling depth, these values could

be useful in assigning the carbonylic and carboxylic functional groups [138]. Clearly, MWNT, GNPs and RGO have similar defective groups like hydroxyl, epoxy (1,2-ether), carbonyl, and carboxyl groups on the surface, which was also indicated in the previous work [78, 244].

## 6.2.2 Mechanism of synthesizing MWNT/PDMS by NIR photon-assisted method

Figures 6.3(a-1), 6.3(a-2), and 6.3(a-3) plot the XPS peaks of O1s, C1s, and Si2p, respectively measured for the MWNT/PDMS composite synthesized by the conventional baking method. Figures 6.3(b-1), 6.3(b-2), and 6.3(b-3) plot the XPS peaks of O1s, C1s, and Si2p, respectively measured for the MWNT/PDMS composite synthesized by the NIR photon-assisted polymerization. The binding energies of O1s for the  $\text{O}=\text{C}$  and  $-\text{O}-$  atoms are 532.5 eV and 533.8 eV, respectively. These values are in good agreement with the previous work [245]. Comparing the O1s peaks in Figure 6.3(a-1) and in Figure 6.3(b-1)), the NIR treated composite exhibits a higher area percentage of the  $-\text{O}-$  bonding and a lower area percentage of the  $\text{O}=\text{C}$  bonding than the conventionally baked composite. The oxygen double bond usually contains a weak  $\pi$ -bond and a strong  $\sigma$ -bond. Under NIR irradiation, this  $\pi$ -bond can be easily opened and thus can easily react with other atoms.

The C1s peaks are fitted by two sub-peaks: one corresponds to the carbon atoms connected with hydrogen or other carbon atoms including the  $\text{sp}^2$  and  $\text{sp}^3$  bonds; the other peak corresponds to the carbon atoms covalently bonded with oxygen atom, including the carbon atoms in hydroxyl, epoxy, carbonyl and carboxylic groups. Comparing the C1s

peaks in Figure 6.3(a-2) and in Figure 6.3(b-2), it shows that the NIR treated composite possesses a higher percentage of carbons bonded with oxygen and a lower percentage of carbons with the C-C/C-H bonds than the conventionally baked composite. It infers that the NIR heat treatment is more effective in oxidizing carbons. The oxygen atoms in PDMS connect with two silicon atoms, which have a very low value of Gibbs free energy and are thus difficult to react [246]. By contrast, the oxygen atoms on the surface of the nano-carbons are much easier to react. The carbon-carbon double bond also has a weak  $\pi$ -bond and a strong  $\sigma$ -bond. Corresponding to the C1s XPS peaks, the oxygen atoms on the nano-carbons bond covalently with the carbon atoms on PDMS and are shown in the O1s XPS peaks.

Figure 6.3(a-3) and Figure 6.3(b-3) plot the Si2p peaks measured in the conventionally baked composite and the NIR treated composite, respectively. The Si2p peak of the NIR treated composite shifts by 0.15 eV to larger binding energies. It means a higher average effective electrostatic force for the Si-O bonds in the NIR treated composite [247]. Compared to the conventionally baked composite, the NIR treated composite also displays a slightly higher percentage of silicons bonded with three or four oxygens. Overall, the trends in the O1s, C1s, and Si2p peaks are in good agreement, indicating that the oxygen atoms on the nano-carbons are bonded with the carbon atoms and the silicon atoms in PDMS.

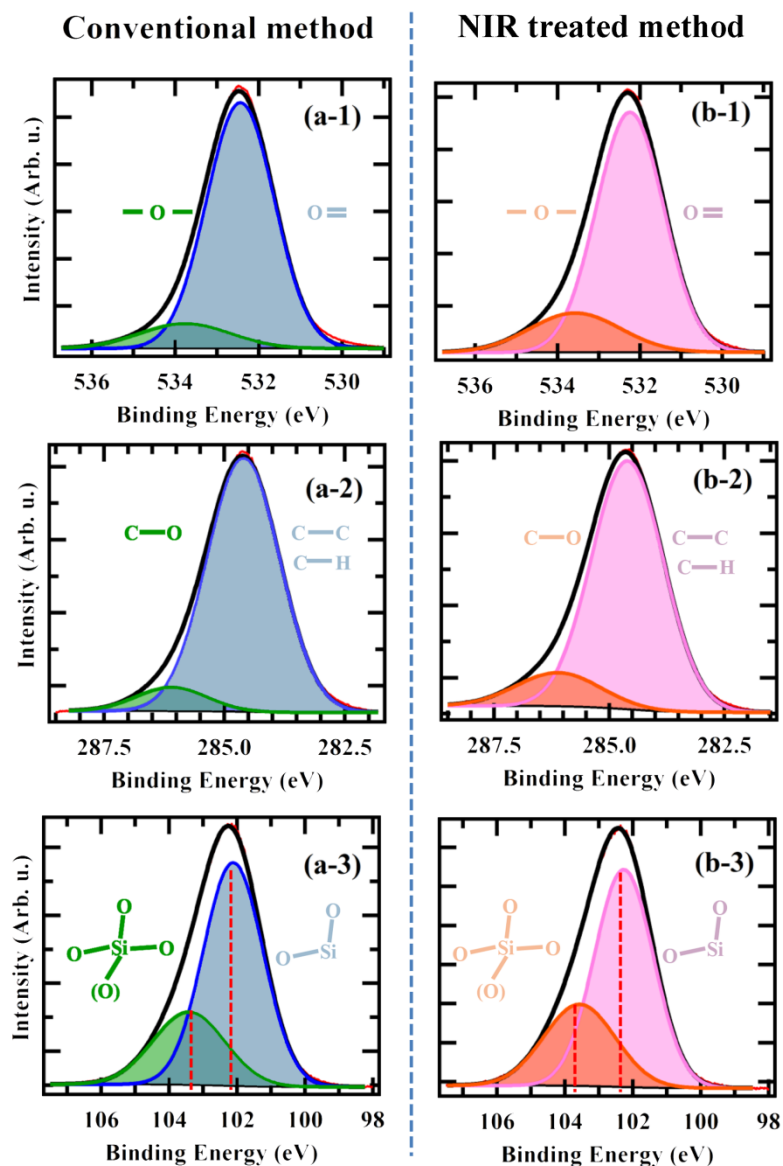


**Figure 6.3** The XPS peaks of O1s, C1s, and Si2p measured for the MWNT/PDMS composites synthesized by (a) the conventional baking method and (b) NIR photon-assisted polymerization.

Table 6.2 lists the ratios between the two different oxygen bonds, the ratios between the two different carbon bonds, and the ratios between different silicon bonds atoms for the MWNT/PDMS composites prepared by oven baking and by NIR heating. These ratios are obtained by fitting the O1s, C1s, and Si2p XPS peaks. For

MWNT/PDMS, the  $\frac{O=}{-O-}$  ratio is about 7.4 and 4.5 for the conventionally baked sample and the NIR treated sample, respectively; the  $\frac{C-C}{C-O}$  ratio is about 11.0 and 6.4 for the conventionally baked sample and the NIR treated sample, respectively; The  $\frac{O-Si-O}{(n)O-Si}$  ratio is about 2.5 and 2.2 for the conventionally baked sample and the NIR treated sample, respectively.

**Table 6.2** The ratios between the two different oxygen bonds, the ratios between the two different carbon bonds, and the ratios between different silicon bonds atoms are listed for MWNT/PDMS composites prepared by oven baking and by NIR heating.

Area ratio	$\frac{O=}{-O-}$	$\frac{C-C}{C-O}$	$\frac{O-Si-O}{(n)O-Si}$
MWNT/PDMS-Baking	$7.4 \pm 0.3$	$11.0 \pm 0.3$	$2.5 \pm 0.1$
MWNT/PDMS-NIR	$4.5 \pm 0.2$	$6.4 \pm 0.2$	$2.2 \pm 0.1$

### 6.2.3 Mechanism of synthesizing graphene/PDMS by NIR photon-assisted method

Figures 6.4(a-1), 6.4(a-2), and 6.4(a-3) plot the XPS peaks of O1s, C1s, and Si2p, respectively measured for the RGO/PDMS composite synthesized by the conventional baking method. Figures 6.4(b-1), 6.4(b-2), and 6.4(b-3) plot the XPS peaks of O1s, C1s, and Si2p, respectively measured for the RGO/PDMS composite synthesized by the NIR photon-assisted polymerization. Figure 6.4 displays the similar contrasts between the RGO/PDMS composites prepared by the two methods as seen in Figure 6.3.

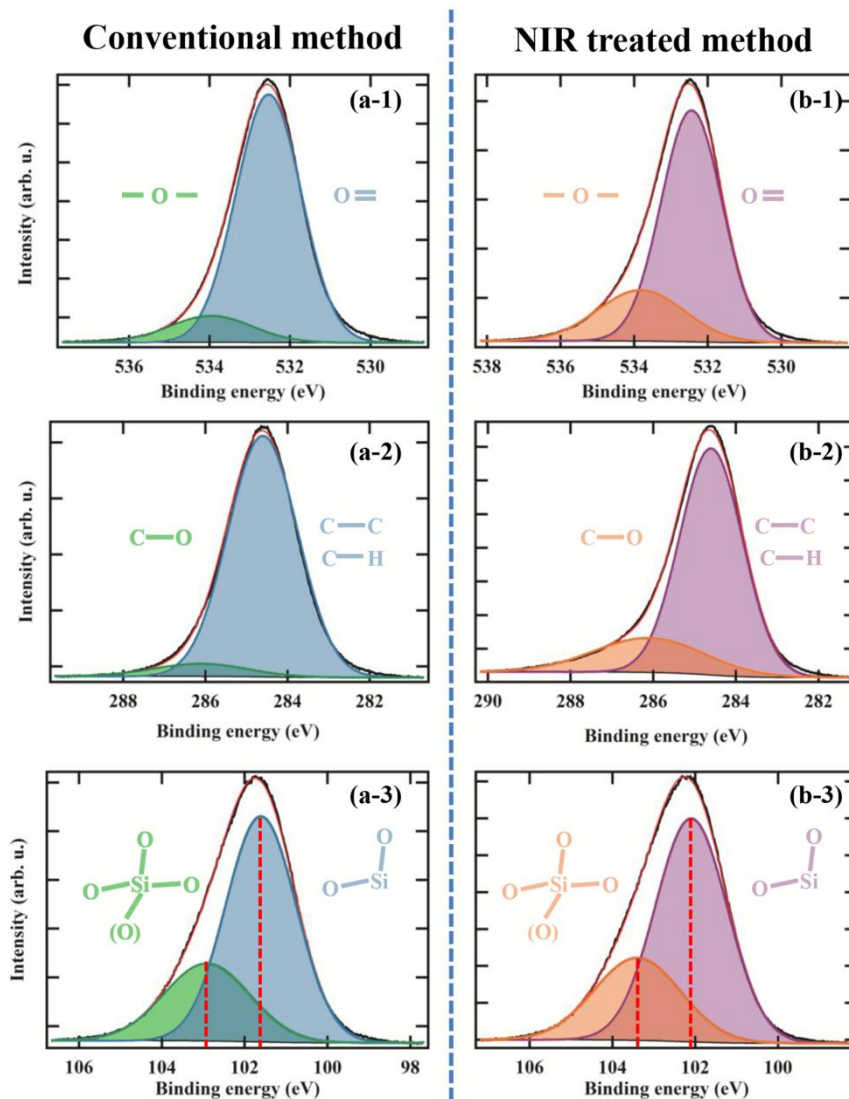


**Figure 6.4** The XPS peaks of O1s, C1s, and Si2p measured for the RGO/PDMS composites synthesized by (a) the conventional baking method and (b) NIR photon-assisted polymerization.

Again, when compared to the conventionally baked RGO/PDMS composite, the NIR treated RGO/PDMS composite shows a higher percentage of the  $-O-$  bonding and a lower percentage of the  $O=$  bonding, a higher percentage of carbons bonded with oxygen and a lower percentage of carbons with the C-C/C-H bonds, a higher percentage of silicons bonded with three or four oxygens.. The Si2p peak of the NIR treated RGO/PDMS composite shifts by 0.5 eV to larger binding energies, in comparison to the

conventionally baked RGO/PDMS composite. The GNP/PDMS composites showed lower percentages of oxygen groups. The NIR treated GNP/PDMS composite and the conventionally baked GNP/PDMS composite were measured to exhibit smaller contrast than those in the cases of MWNT/PDMS and RGO/PDMS.

**Table 6.3** The ratios between the two different oxygen bonds, the ratios between the two different carbon bonds, and the ratios between different silicon bonds atoms are listed for RGO/PDMS, and GNP/PDMS composites prepared by oven baking and by NIR heating.

Area ratio	$\frac{O=}{-O-}$	$\frac{C-C}{C-O}$	$\frac{O-Si-O}{(n)O-Si}$
RGO/PDMS-Baking	$6.8 \pm 0.6$	$10.6 \pm 0.6$	$2.5 \pm 0.1$
RGO/PDMS-NIR	$3.0 \pm 0.2$	$3.7 \pm 0.3$	$2.1 \pm 0.1$
GNP/PDMS-Baking	$10.7 \pm 0.3$	$7.6 \pm 0.3$	$2.6 \pm 0.1$
GNP/PDMS-NIR	$10.1 \pm 0.2$	$7.5 \pm 0.1$	$2.4 \pm 0.1$

Table 6.3 lists the ratios between the two different oxygen bonds, the ratios between the two different carbon bonds, and the ratios between different silicon bonds atoms also for the RGO/PDMS and GNP/PDMS composites prepared by oven baking and by NIR heating. For the RGO/PDMS composites, the  $\frac{O=}{-O-}$  area ratio is around 6.8 and 3.0 for the conventionally baked sample and the NIR treated sample; the  $\frac{C-C}{C-O}$  area ratio is around 10.6 and 3.7 for the conventionally baked sample and the NIR treated sample; the  $\frac{O-Si-O}{(n)O-Si}$  area ratio is around 2.5 and 2.1 for the conventionally baked sample and the NIR treated sample. For the GNP/PDMS composites, the  $\frac{O=}{-O-}$  ratio is around 10.7 and 10.1 for the conventionally baked sample and the NIR treated sample; the  $\frac{C-C}{C-O}$  area ratio is around 7.6 and 7.5 for the conventionally baked sample and the NIR treated sample; the  $\frac{O-Si-O}{(n)O-Si}$

area ratio is around 2.6 and 2.4 for the conventionally baked sample and the NIR treated sample.

#### 6.2.4 Mechanism of NIR light induced polymerization of nano-carbon/polymer composites

Figure 6.5(a-1) depicts the chemical structures of the oligomers and the crosslinkers of PDMS and RGO. The Epoxy, hydroxyl, carbonyl and carboxyl groups are shown on the surface of RGO. In Figure 6.5(a-2), the green circle depicts the crosslink process between the PDMS oligomers and the PDMS crosslinker. The red circle and the purple circle depict two reactions between PDMS and RGO during NIR photon-assisted polymerization. Figure 6.5(a-3) shows the model of near NIR photon-assisted polymerization. The crosslinking reaction depicted in the green circle still takes place due to the heat generated from the nano-carbons by photothermal heating. We found macroscopic temperature increase of 70 °C by using photon assisted heating. This value compares well with past photo-thermal heating of nanotubes [47, 49], graphene [233-235], nanoshells [236-238] and other nanoparticles [239, 240]. The reaction in the red circle shows the  $\pi$ -bond is opened and is connected with the hydroxyl group on the surface of RGO. As depicted in the purple circle, the silicon atom of the SiH group, which also efficiently absorbing NIR light, reacts with the carbonyl group on the surface of RGO. Such two reactions create new covalent bonds between the carbon atoms in PDMS and the oxygen atoms on RGO, thus greatly strengthening the interface and

improving the mechanical properties of the nano-carbon composites. These formations have also been shown in past work with photon-assisted [248-250].

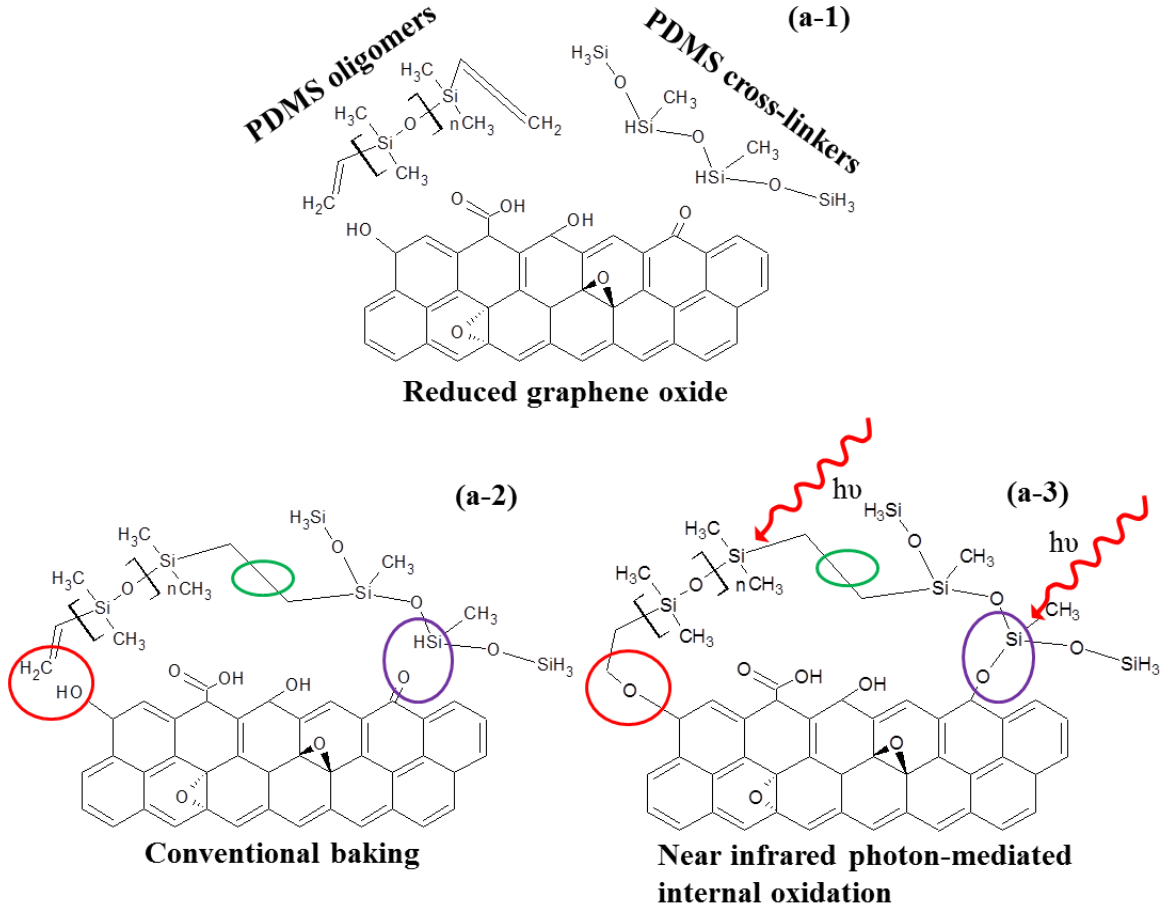


**Figure 6.5** (a-1) The chemical structures of the PDMS oligomer and the PDMS cross-linker; (a-2) the reaction model of the conventional baking polymerization; (a-3) the reaction model of the NIR photon-assisted polymerization.

### 6.3 Conclusion

This chapter compares the NIR treatment polymerization and the conventional baking polymerization by using three different nano-carbons (MWNT, GNP and RGO) to

prepare the nano-carbon/polymer composites. XPS was used to analyze and compare the interfacial bond formation of the nano-carbon/polymer composites synthesized by both methods.

It was found that, the NIR treated composites contained more C–O, –O–, Si–O bonds than the conventionally baked composites when all three types of nanocarbons were used as the fillers. It indicates that more covalent bonds are formed between the nano-carbons and the polymer matrix in the NIR heating-assisted polymerization, which helps to strengthen the interface. This result is also in agreement with the earlier Raman measurements that under strain the smaller change of the FWHM for the Raman peaks and the larger shifts for the Raman peak positions were observed for the NIR treated composites. This type of interfacial strengthening is not achievable by the conventional oven baking method because heat flows from the outside to the inside of the composite and thus strong depending on the thermal conductivities of the entire polymer matrix and the nanocarbon fillers.

Further, the XPS studies show direct correlation between bond formation and overall improvement in mechanical properties such as Young's modulus, strain energy density, toughness, and load transfer. The NIR light induced heating and oxidation is one method that can claim no interfacial damage to the nano-carbon during functionalization. Further, instead of using acids and chemicals for functionalization, this is an environmentally friendly process. Such process could be highly useful in scalable nano-manufacturing of laminates of composites with controllable properties, no achieved using oven based polymerization methods.

## CHAPTER 7 FLEXIBLE SANDWICHED-STRUCTURE STRAIN SENSOR FABRICATED BY NEAR INFRARED PHOTON-ASSISTED POLYMERIZATION

### 7.1 Introduction

Strain sensors are used to detect structural damage and measure local deformation, characterize and study the fatigue properties of materials [251]. William Thomson *et al.* first investigated the resistance change versus elongation in iron and copper in 1856 [252]. After 80 years, Edward Simmons reported the first bonded metallic strain gauge, and calculated its gauge factor about  $\sim 2$ [251, 253]. In 1950, Bardeen *et al.* first suggested relatively large conductivity changes with deformation in single crystal semiconductors leading to semiconductor based strain gauges[254]. First silicon strain gauge was reported first in 1957 by Mason *et al.*, and the sensitivity was 50 times higher than conventional metal based strain sensors [255]. Although the conventional strain gauges shows high strain sensitivity at low cost [251], they still have drawbacks namely: 1) they cannot remain active and electrically stable under large mechanical deformations like conductive flexible polymer composites [256]; 2) low resolution at micro- and nano-scale; 3) most of them can only be used to measure strains in specific direction; Besides, the conventional strain sensors are difficult to integrate into structural materials [257].

The discovery of CNT [10] and graphene [11] has rejuvenated the area of strain sensing. Nanocarbons such as nanotubes and graphene has excellent physical properties

namely: low density, high Young's modulus, high electrical conductivity and compatible to be integrated into the structural material in the form of reinforcements [257]. Also, it has been shown that the compression and tension strain has an important influence of electronic band-gap changes of CNT [258] and graphene [259].

**Table 7.1 Comparison with different types strain sensors**

Strain sensor material	Gauge Factor	Reference
Metal	2 (5% maximum strain)	[251]
Individual nanotube	1000	[260]
Carbon black/TPE composites	~20	[261]
SWNT/PDMS composites	0.06~0.82	[256]
CNT/Epoxy	23 (0.6% maximum strain)	[262]
CNT/PMMA	15 (1% maximum strain)	[263]
MWNT/PDMS composites	~2	[264]
CVD grown graphene/PET	6.1	[265]
CVD grown graphene/PDMS	2.4 (< 1.8% strain)	[266]
Graphene ripples/PDMS	~2	[267]

Several studies have used nano-carbon/polymer materials for strain sensing (Table 7.1). It is reported that the strain sensor with individual nanotube can reach the gauge factor of ~1000 [260]. However this type of sensor is difficult to fabricate, the orientation and strain test range are also quite limited. Liu *et al.* reported the work of dispersing ~9 wt. % of CNTs into PDMS to fabricate a strain sensor with gauge factor (GF) ~2 with large strain range and high repeatability [264]. Carbon black/thermoplastic

elastomer (TPE) composites strain sensor is reported to have a GF value of ~20 [261]. CNT are dispersed into epoxy and poly(methyl methacrylate) (PMMA) to fabricate strain sensors were reported to have GF values of 23 and 15 respectively. Lee *et al.* reported the chemical vapor deposition (CVD) grown graphene based strain sensor with a GF of 6.1 in 2009 [265]. Similarly, Fu *et al.* demonstrated strain sensors with a monolayer graphene with high strain sensitivity, however it failed to recover when the strain was larger than 5% [268]. In 2013, Bae *et al.* investigated a transparent and stretchable strain sensor based on CVD-grown graphene up to 7.1% strain, and the GF of 2.4 when the strain was lower than 1.8% [266].

Although some of strain sensors shown in Table 7.1 have a large GF value, they only tolerated a small maximum strain (<1%). Under a small strain, CNT and graphene can stick well to the polymer matrix by weak van der Waals interaction. However, under a large structural deformation, sliding, slippage or even fracture are expected for nano-carbons on their supporting polymer due to the rigid nature of nano-carbons [267]. Strong interface between nano-carbon reinforcements and supporting polymer is required. Therefore, we investigated whether the use of RGO with NIR photon-assisted polymerization of the interface could lead to enhanced strain sensitivity.

The NIR photon-assisted polymerization of MWNT/PDMS [173], RGO/DPMS, and GNP/DPMS composites were discussed in the previous chapters. Large load transfer, high toughness and strong nano-carbon/polymer interface were observed. Thus, the NIR photon-assisted polymerization method is advantageous for fabricating nano-carbon/polymer composites to produce strain sensor. Compared to CVD grown graphene, RGO (ACS chemicals) can be cheaply produced from graphite oxide. RGO is much

cheaper than CNTs and pristine graphene. Similar to pristine graphene, RGO also has a high toughness and can be used to improve mechanical properties.

In this chapter, we discuss a new type of strain sensor with a PDMS/RGO/PDMS sandwiched-structure fabricated by using NIR photon-assisted polymerization. The strong interfaces between RGO and PDMS enhance the repeatability and the sensitivity of strain sensor under large structure deformation.

## **7.2 Experimental section**

### **7.2.1 The fabrication process of the strain sensor**

We use PDMS, crosslinker (Sylgard 184, Dow Corning), and RGO (ACS chemicals) to fabricate RGO/polymer lamina composite. A layer of paralyene (~1  $\mu\text{m}$  thick) is first uniformly coated on a silicon wafer (SCS). Then, PDMS is spun on top of the substrate at speed of 500 rpm for 30 s. PDMS is about 150  $\mu\text{m}$  thick and is then cured by using NIR heating.

A transfer method was used to deposit a thin layer of RGO on top of PDMS, which is shown in Figure 7.1. To prepare a RGO layer on top of the PDMS layer, we used a vacuum filtration method, which has been used widely in the past to produce CNT film [269, 270], Briefly, RGO is first dissolved in IPA and the solution is ultrasonicated for 4 h. Then, the RGO suspension is filtered through a commercial mixed cellulose ester (MCE) filter with an average pore size of 50 nm. When the suspension is filtered through MCE filter, the liquid passes through the pores whereas the RGO film becomes lodged on

top of the MCE filter (Figure 7.1(b)). The thickness of the RGO film is determined by the concentration of RGO in the suspension and the volume of the suspension.

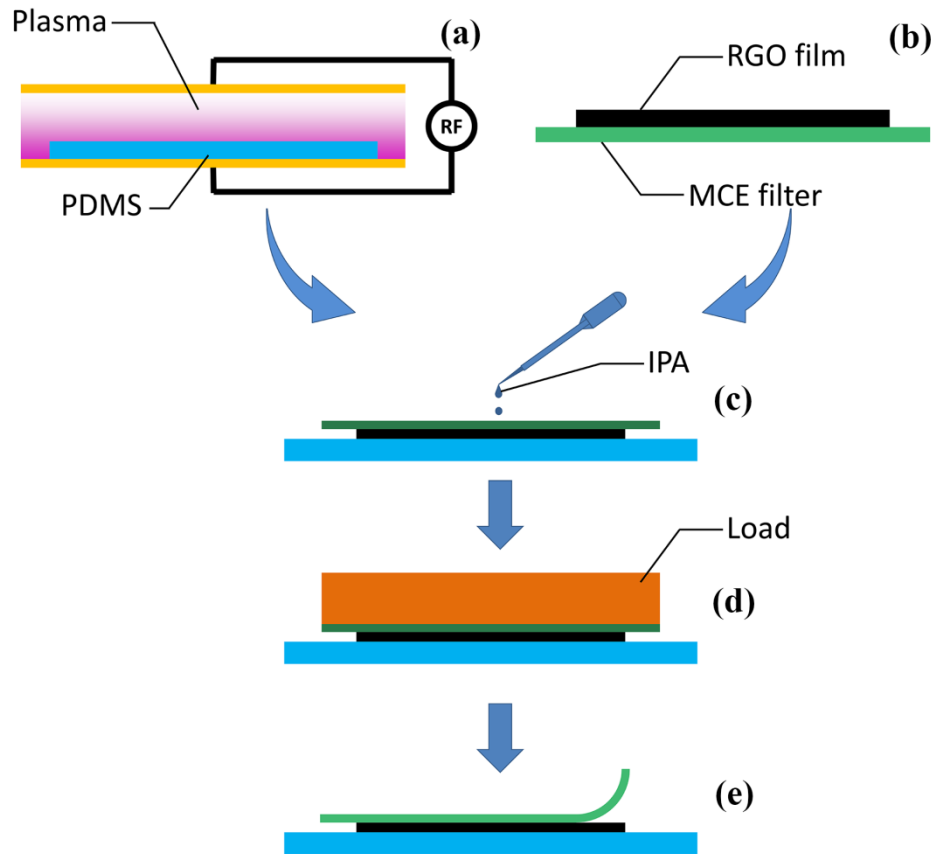


**Figure 7.1** The schematic of the RGO film transfer process

Before transferring the RGO film, the PDMS surface is treated by using oxygen plasma to change the surface energy (Figure 7.1(a)). Then, the MCE filter with the RGO film is slid down onto the surface modified PDMS layer (Figure 7.1(c)) and gently wetted with IPA. A compressing load is applied for 5 min to increase the adherence between the RGO film and the PDMS layer (Figure 7.1(d)). After removing the compressing load, the MCE filter and the RGO film are separated by themselves during the self-drying process.

The yield of the RGO film by using this transfer process is nearly 100%, indicating that the van der Waals force between the RGO film and the PDMS layer is sufficiently strong.

Photolithography is then used to define the RGO patterns. Commercial photoresist S1813 is used as the etching mask for patterning the RGO film. After patterning the photoresist, oxygen plasma is used to etch the RGO film. After etching, acetone rinsing is used to remove the etching mask and to clean the RGO film. Next, another layer of PDMS is spun on the top and is cured under NIR light heating to attain full crosslinking. At the end, the laminar composite can be easily peeled off from the substrate due to the low adherence between PDMS and the paralyene film.

The synthesized PDMS/RGO/PDMS laminar strain sensor is shown in Figure 7.2. Figure 7.2(a) displays the patterned RGO stripe sandwiched between the two PDMS layers. Figure 7.2(b) displays the sandwich-structured PDMS/RGO/PDMS strain sensor free of strain. Figure 7.2(c) displays the sensor under  $\sim 80\%$  stretch. High stretchable ability of the strain sensor is addressed here.

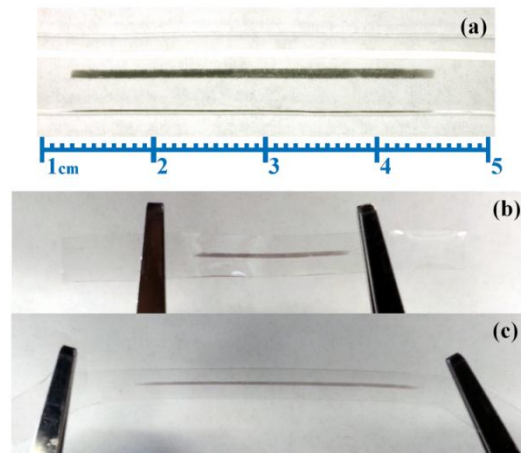


**Figure 7.2** The demo structure of strain sensor

7.2.2 The experimental setup for the strain-resistance relationship of the sandwiched-structure strain sensor

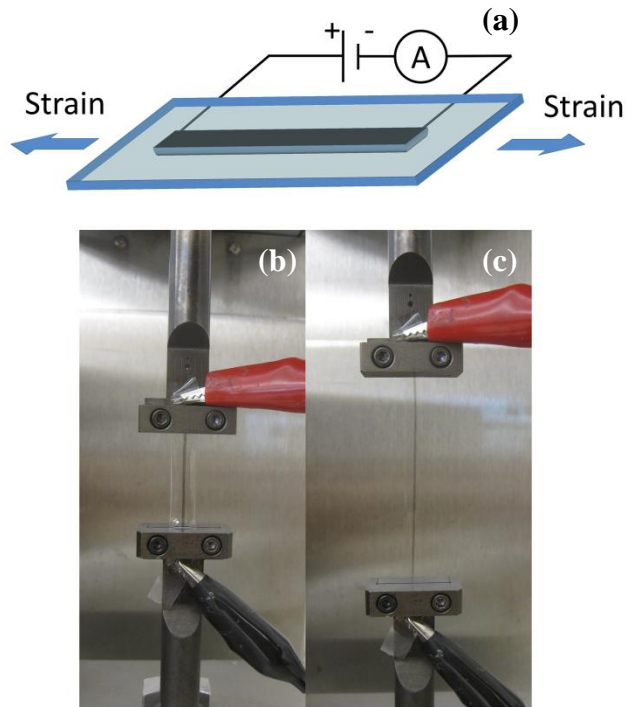


**Figure 7.3** The test setup to measure the strain-resistance relationship of the strain sensor: (a) a schematic diagram of the test setup, strain is applied to the both ends of the sensor, and two-probe electrode connections are made at both ends of RGO film using copper wires; (b) the strain sensor free of strain; (c) strain sensor under 100% strain

Figure 7.3(a) shows the schematic experimental setup for testing the strain-resistance of the synthesized strain sensor. It is anchored and supplied with different strain by using a RSA. To make a two-probe connection, both ends of the sensor are connected to copper wires and a digital multi-meter (Keithley, 2400 series) is used to record the resistance value during the stretching and relaxing processes. All the data are collected by the LABVIEW software. Figures 7.3(b) shows the strain sensor free of strain

and 7.3(c) shows the strain sensor under the 100% stretch. After removing the strain, there is no obvious structural damage to the strain sensor.

### 7.3 Results and discussion

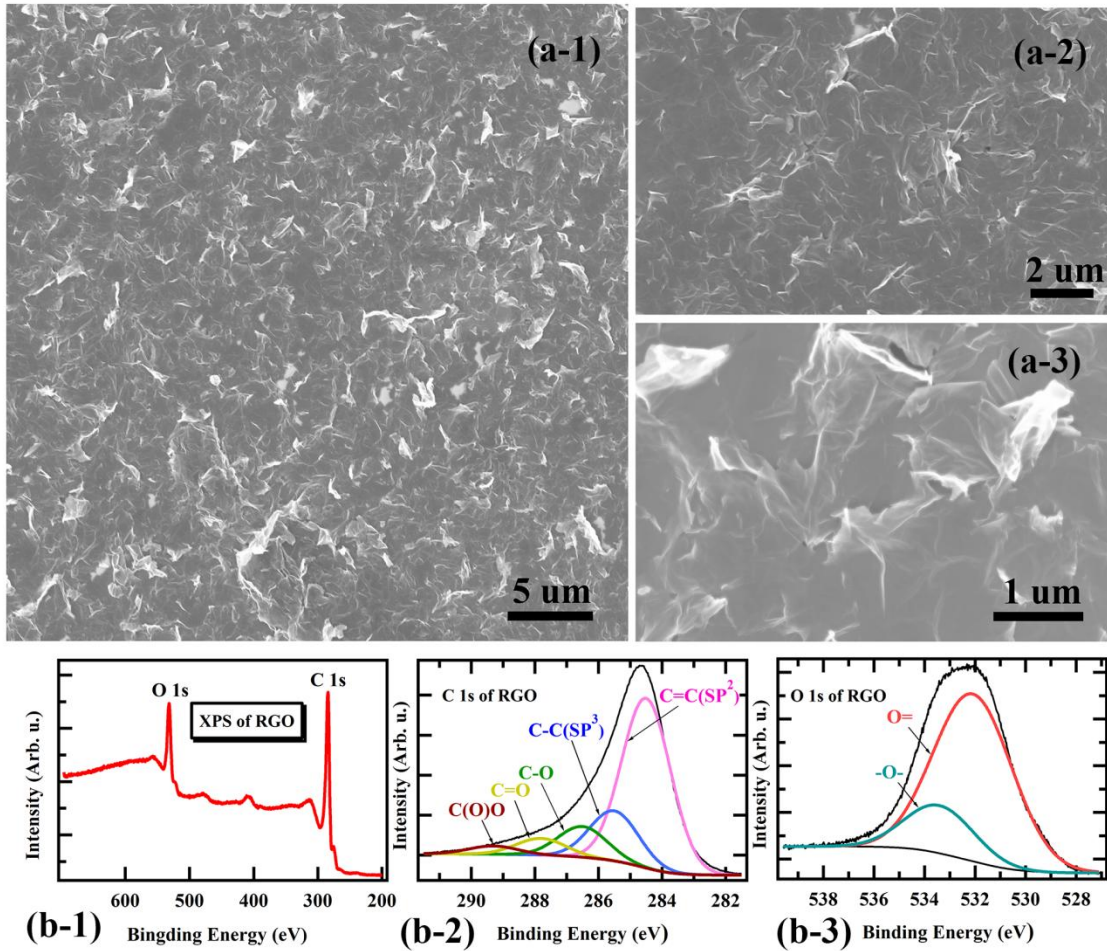


**Figure 7.4 (a) The SEM images of the RGO film under different magnifications; (b-1) the XPS spectrum of the RGO film; (b-2) the C1s and (b-3) the O1s peaks with multiple-component simulation.**

Figures 7.4(a-1), 7.4(a-2), and 7.4(a-3) display the scanning electron microscopy (SEM) images of the synthesized RGO film. Large surface area of RGO and uniform

RGO film are shown. Figure 7.4(b) shows the XPS spectrum of the RGO film. The C1s and O1s peaks are analyzed to identify the chemicals in RGO, and the analyses are displayed in Figure 7.4(b-2) and Figure 7.4(b-3), respectively.

After performing the Shirley background correction, the C1s and O1s peaks are fitted with multiple Gaussian shapes. As fit, many functional groups such as -OH, -COOH, and -C=O were shown by the C1s peak. The O1s peak also shows two different oxygen groups on the RGO film.

As shown in Figure 7.5(a), the parallel patterned RGO stripes, about 100  $\mu\text{m}$  in width and 200 nm in thickness, were fabricated by etching away the unwanted RGO using oxygen plasma. Figure 7.5(b) shows well defined and sharp edges. It is of note, even finer structures can be patterned by photolithography.

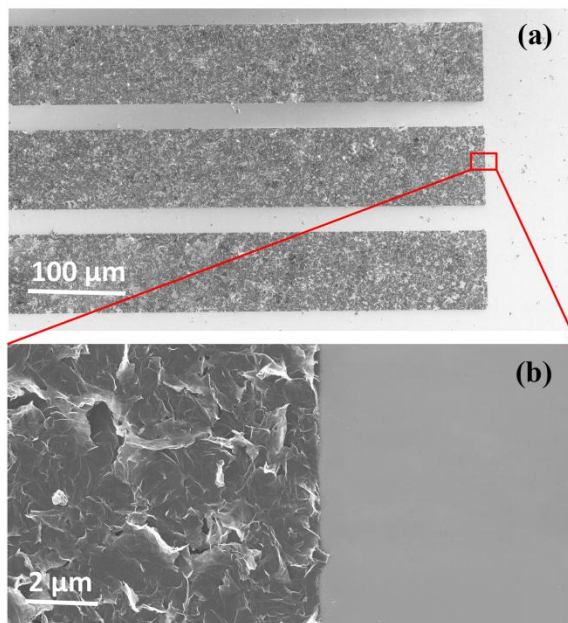


**Figure 7.5 (a) The clear pattern of the  $\sim 80\mu\text{m}$  RGO stripes with  $\sim 20 \mu\text{m}$  spacing; (b) the sharp pattern edge formed by etching.**

Figure 7.6(a) displays the SEM cross-section image of the flexible strain sensor. Uniform RGO film, which as a conductive layer, can be clearly seen between the top and bottom PDMS layers. The high transparency of the flexible sensor with a 280 nm thickness RGO film is shown in Figure 7.6(b). Figure 7.6(c) indicates the relationship among sheet resistance, transparency and thickness. Low sheet resistance of  $1.5 \times 10^5 \Omega/\square$  is observed at the thickness of 382 nm with  $\sim 20\%$  transmittance at 600 nm wavelength.

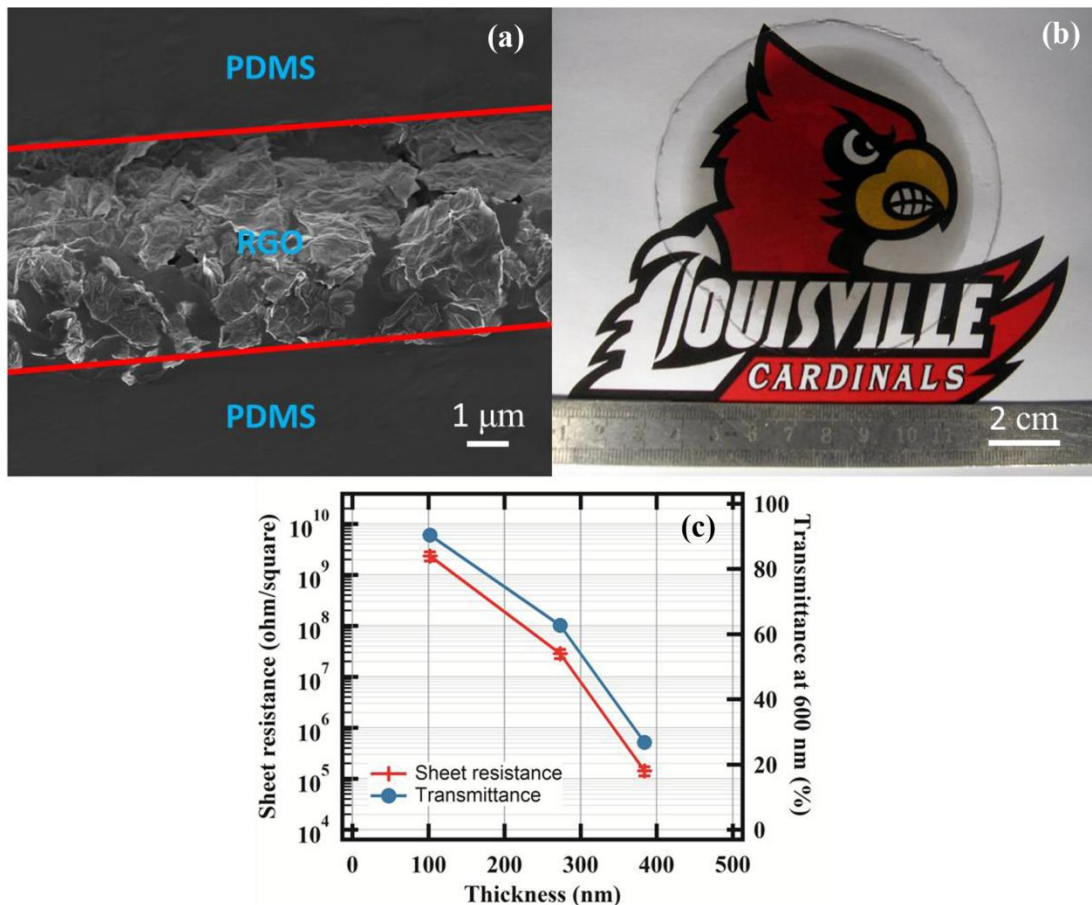


Figure 7.6 (a) The SEM cross-section image of the sandwich-structured strain sensor; (b) the large diameter  $\sim 10$  cm sandwiched structure laminar composites; (c) the sheet resistance and the transmittance at 600 nm of different thickness.

To further study the strain-dependent resistance of the nanocomposite device, multiple cycles of stretching and relaxation were applied by using RSA (Figure 7.7(a, blue line)). A 5% tension strain is applied for 100s, it is then off for 100s, and such a cycle is repeated for 100 times. Although some initial time dependence is seen from the experiment, the resistance response becomes repeatable after several tests. That is because the long chain molecule will move and establish in a low state energy. The red line in Figure 7.7(a) shows the resistance response during tensile strain loading cycle. High repeatability of the strain sensor is addressed. The inset image shows five cycle in detail. The resistance varied from about 4.1 to 4.9 MΩ, giving rise to a relative change of ~20%. It should be noted that the resistance changes after switching the strain due to polymer chain mobility.

The gauge factor (GF) of the strain sensor can be calculated as:

$$GF = \frac{\Delta R}{R} / \varepsilon$$

, where  $\frac{\Delta R}{R}$  is a relative resistance change and  $\varepsilon$  is the strain applied.

Figure 7.7(b) presents the linear relationship between the resistance change at 20% tensile strain applied to the sensor. The linear function (blue line) is used to fit the original data (red dots) in Figure 7.7(b). The average GF of this flexible strain sensor, which is the gradient of the fitting linear function, is 8.75, higher than that of conventional strain sensor [251].

Figure 7.7(c) presents the cyclic stress-strain curves for the PDMS/RGO/PMDS composite strain sensor. These curves are similar as those of pure PDMS. At lower strain, the elasticity of the composites is restored to the initial configuration after the strain is removed. Under large strain, it takes longer time for the polymer chains to restore the

initial configuration. It is noted that the composites with different thickness of RGO film show similar strain-stress curves. Obviously, to a degree the PDMS layers shield the RGO film from the external force. The Young's modulus of the composite is  $\sim 1.1$  MPa which is a little larger than pure PDMS because the load is transferred to RGO film through the interface.

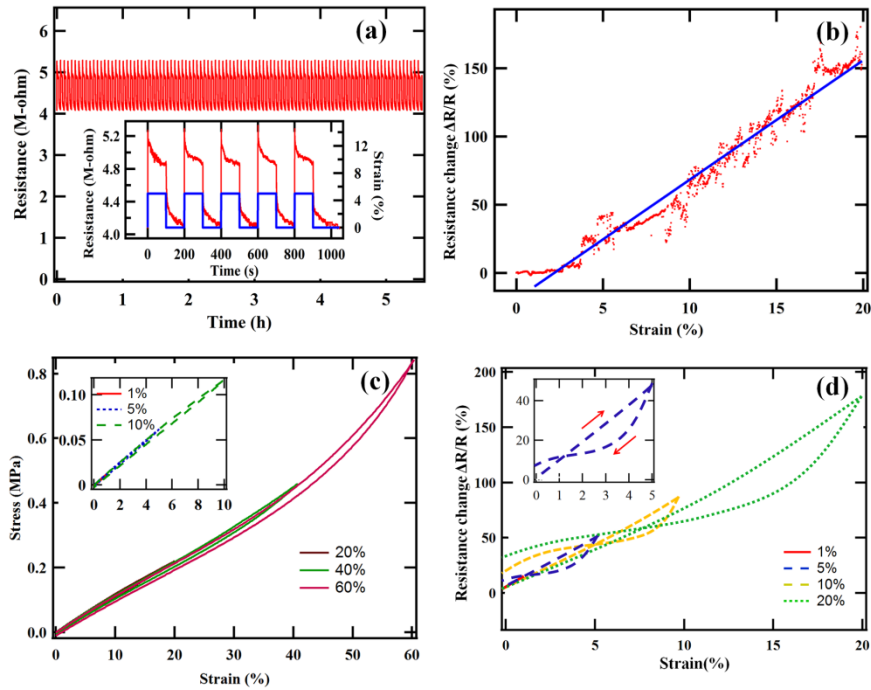


**Figure 7.7 (a) The resistance of the strain sensor over time under 100 times cyclic loading of 5% tension strain, the inset is five times cyclic loading in detail; (b) resistance change versus strain of strain sensor; (c) the cyclic stress-strain curves of strain sensor; (d) the resistance change of the strain sensor under cyclic loadings of different maximum strain.**

Figure 7.7(d) shows the relationship between loading cycle and the resistance change. The strain sensor is applied with cyclic tension strain with the same strain rate. The linear resistance change during the strain loading process is shown in the inset of Figure 7.7(d), with the maximum strain at  $\sim 5\%$ . Measurement with different maximum

strain resulted in similar curves. Additionally, different strain change rates were also applied, similar curves were still observed. During the loading process, the resistance changes linearly with strain. However the resistance does not change linearly during the unloading process, the hysteresis response was observed. Similar hysteresis response was also addressed in the previous MWNT/PDMS strain sensor [264]. As shown in Figure 7.7(d), the resistance does not return to the initial value when the strain is removed. Only after long relaxing time, does the resistance return to the initial value. Another observation of the hysteresis response is the resistance drops faster after strain changes direction, and after a certain strain point the resistance drops at a slower rate. It is probably due to the polymeric chain mobility and the viscoelastic properties of PDMS. Besides, the sensor shows less sensitivity after lots of repeated test similar to previous report due to Mullins effect, describing a phenomenon of a reduction in stress after the initial extensions [271].

Figure 7.8 shows the mechanism of the resistance response during the loading process. As shown in Figure 7.8(a), graphene layers are embedded inside of PDMS matrix. When no strain is applied, electrons can tunnel or flow through the adjacent RGO layers in the overlapping area (red zone). In Figure 7.8(b), when a uniaxial strain is applied along the horizontal direction, both PDMS and RGO films are stretched. The resistance change of the strain sensor mainly due to the modification in intrinsic resistance of RGO film and the interlayer resistance of RGO films. Related to the intrinsic resistance, the single RGO film is stretched under uniaxial strain, causing the interatomic distance increase. And following electrical band structure changes results in the intrinsic resistance of RGO film increases. Previous studies shown the intrinsic

conductivity of graphene changes exponentially with the applied strain [272]. In the aspect of interlayer resistance, two types resistance, which include contact resistance and tunneling resistance, need to be concerned. Compared to intrinsic resistance of graphene film, interlayer resistance is much larger depending on arrangement of molecules across the interface and extent of the interfacial surface [273]. When a uniaxial tensile strain is applied, RGO films are pulled away from each other due to the load transfer from PDMS to RGO through the PDMS/RGO/PDMS interface. As a result, the overlapping area is getting smaller and contact points between different RGO films are losing, increasing the interlayer resistance of RGO films. Overall, the total resistance of the strain sensor increases when the uniaxial strain is applied. After removing the strain, the RGO films are to relax and the original resistance can be restored.

Weak interface between RGO film and polymer matrix will result in slippage, sliding, and even failure under low strain. Bae *et al.* studied the strain sensor with CVD grown graphene on top of PDMS. The 300 nm Ni catalyst layer was first deposited on SiO<sub>2</sub>/Si using e-beam evaporator, following CVD method to grow the graphene on Ni catalyst layers. The photolithography and oxygen plasma were used to pattern the graphene film. After that, patterned graphene film was attached to PDMS cured at the temperature 70 °C and the substrate was etched to fabricate the strain sensor. The linear region of this type sensor only can be observed within 1.8% strain, and gauge factor ~1.4 is reached. The relationship between resistance and the strain get nonlinear in the range between 1.8% and 7.1%. And the strain sensor will be failure after 7.1% tensile strain [266]. Compared with the strain sensor Bae *et al.* studied, the strain sensor fabricated by NIR photon-assisted polymerization shows larger strain sensor range and large linear

range between resistance and tensile strain due to stronger interface between RGO and polymer.

There are limitations that needed to be addressed here. Factors that can affect electrical resistance and gauge factor of the strain sensor are namely: 1) temperature 2) pressure, 3) dispersion method of graphene, 4) defect densities, 5) sonication times and polymer material properties.

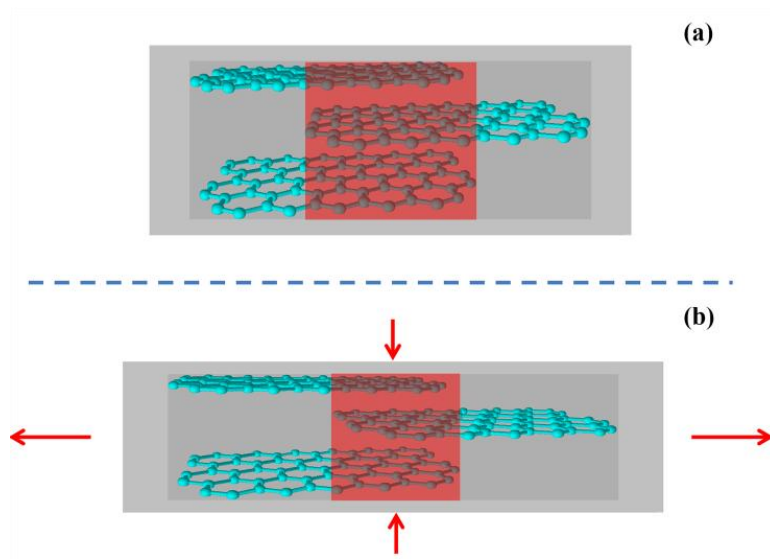


**Figure 7.8** The mechanism of PDMS/RGO/PDMS sandwiched structure strain sensor: (a) the strain sensor free of strain; (b) the strain sensor under the tensile strain.

## 7.4 Conclusion

This Chapter describes a new film transfer method used to deposit RGO film and fabricate strain sensors based on NIR polymerization method. The thickness of RGO film can be precise controlled by the concentration and the volume of the dispersion solution. Wafer size and uniform RGO film deposited by transfer method are also shown.

NIR photon-assisted polymerization method is successfully used to fabricate transparent and flexible sandwiched strain sensor made of the PDMS/RGO/PDMS laminar composite synthesized. High capability of polymerizing large scale flexible film is also demonstrated. While it has not been directly compared to conventional polymerization methods, it is expected from all our previous experiences that the gauge factor of the NIR polymerized samples should be significantly higher.

Photolithography and oxygen etching are used to successfully pattern the RGO film. Fine patterning and sharp edge of patterned RGO film is observed. Larger gauge factor of about 8.75 is achieved on the PDMS/RGO/PDMS strain sensor compared to conventional strain sensor. Large linear range between electrical resistance and tensile strain is shown. High repeatability and linear functional properties of PDMS/RGO/PDMS strain sensor are observed.

Looking forward, the applications of RGO will be explored in the field of nanotechnology in near future since RGO is a great substitute of graphene and CNT with great mechanical, thermal properties and low cost. And NIR photon-assisted polymerization can also be widely used to fabricate large scale nano-carbons' electronics and as a fundamental technique to enable large scale cross-linking and enhanced mechanical properties of nano-composite materials in general.

## CHAPTER 8 CONCLUSIONS AND FUTURE RESEARCH

### 8.1 Conclusions

This dissertation reports the novel NIR photon-assisted polymerization method for synergizing nano-carbon/polymer composites to improve load transfer and mechanical properties. Nano-carbons are first blended into the polymer matrix using either shear mixing or evaporation dispersion techniques. After spin casting the polymer composite mixtures onto glass substrates, a NIR light source is used to supply NIR photons to crosslink the composites and synergize flexible composites films.

First, NIR photon-assisted polymerization of CNT polymer composites was investigated. This study demonstrated photon-assisted heating of MWNTs inside a polymer matrix that resulted in better polymerization of the nanotube/polymer interface as compared to traditional convention heating methods. Using this new method, dramatic enhancements in load transfer from the matrix to the nanotubes and subsequent increases in Young's modulus was observed. Compared to traditional polymerization techniques, the NIR method yielded an increase in Young's modulus value of ~130% for just 1 wt. % MWNT in PDMS polymer, greater than most other methods reported to date. Raman spectroscopy revealed wavenumber shifts of  $\sim 20\text{ cm}^{-1}$  for ~80% strain, larger than most past reported values. These results suggest NIR light-induced heating of CNTs at the

nanoscale could potentially be used as a scalable nanomanufacturing technique for increased load transfer and higher mechanical strength for reinforced polymer composites

Following this initial investigation, NIR photon-assisted polymerization of graphene polymer composites were also studied. Two types of graphene were used: 2.5D GNPs and 2D RGO. The G bands of pure fillers and post fabrication of GNP or RGO/PDMS composites were found to be shifted, suggesting compressive loading on the filler lattice. Mixing RGO in polymers resulted in doping and functionalization that was characterized using shifts in  $I_{2D}/I_G$  ratio. Significant decrease in  $I_{2D}/I_G$  was observed for RGO fillers in polymer composites.

While investigating the two polymerization techniques, it was found that NIR-based polymerization resulted in higher load transfer and mechanical strength of GNP and RGO based composites. The load transfer was higher for RGO/PDMS based composites compared to GNP/PDMS based composites for both types of polymerization. The rigid stack-like morphology of the GNPs and lack of inter-plate interactions with the polymer using conventional oven-based polymerization played an important role in slippage during load transfer and lower mechanical strength. RGO sheets, on the other hand, were able to weave themselves within the polymer, thus creating a continuous polymeric composite that enabled higher load transfer and minimized slippage. For a 1 wt. % RGO/PDMS composite, NIR polymerization resulted in ~116% increase in Young's modulus, ~227% increase of toughness, ~1431% increase of damping capability, and ~233% increase in strain energy density.. For a 1 wt. % GNP/PDMS composite, NIR polymerization resulted in a ~55.56% increase in Young's modulus, ~181% increase in toughness, ~324% increase in damping capability, and ~184% increase in strain energy

density. The comparison between these two composites highlights the differences in mechanical strength achieved by just few atomic layers of carbon. Such excellent mechanical property improvement for small fraction of chemically derived RGO and GNP presents opportunities for developing advanced low-cost graphene-based composites.

By applying NIR photon-assisted polymerization, the synergistic effects of binary nano-carbon mixtures is achieved using Raman spectroscopy and polymer physics principles. Significant shifts in *G*-bands were observed both in tension and compression for both single as well binary nano-carbon mixtures in polymer composites. Addition of small amounts of MWNT (~0.1 wt. %) dispersed in RGO (0.9 wt. %)/PDMS samples reversed the sign of the Raman wavenumbers from positive to negative values demonstrating complete reversal of lattice stress. A wavenumber change from  $10\text{ cm}^{-1}$  in compression to  $10\text{ cm}^{-1}$  in tension was observed for MWNT<sub>0.1</sub>RGO<sub>0.9</sub>/PDMS with applied uniaxial tension. MWNTs limited the deformation of RGO in one direction by providing limited extensibility to the chains and thereby improving the Young's modulus by ~103% as compared to pristine polymer. Such impressive results suggest cooperative action of two nano-carbon fillers is better than single nano-carbon for better interfacial strength, mechanical properties, and load transfer. Synergy between two nano-carbons in polymer materials could be highly useful in development of sensors, actuators, and in general mixed dimensional systems based on carbon [216]. Higher photo-mechanical response under high strain and lower photo-mechanical response under low strain are also shown for mixture nano-carbons/polymer composites compared with pure nano-carbon/polymer composites under high tension strain.

XPS is used to analyze and compare the interface chemicals of nano-carbon polymer composites synergized by NIR photon-assisted and conventional baking polymerization. As found, the NIR treated composites contain more C–O, –O–, Si–O bonds than the conventionally baked composites when all three types of nanocarbons were used as the fillers. It indicates that more covalent bonds are formed between the nano-carbons and the polymer matrix in the NIR heating-assisted polymerization, which helps strengthen the interface. This result is also in agreement with earlier Raman measurements that showed under strain the smaller change of the FWHM for the Raman peaks and the larger shifts for the Raman peak positions were observed for the NIR treated composites. This type of interfacial strengthening is not achievable by conventional oven baking method because heat flows from the outside to the inside of the composite and thus strong depending on the thermal conductivities of the entire polymer matrix and the nanocarbon fillers.

As a demo application of the NIR photon-assisted polymerization, the flexible sandwiched strain sensor made of the PDMS/RGO/PDMS laminar composite synthesized by NIR photon-assisted polymerization was developed. High capability of polymerizing large-scale flexible film is demonstrated. Photolithography was used to pattern the RGO film. A large gauge factor of about 8.75 is achieved on the PDMS/RGO/PDMS strain sensor. High repeatability and linear functional properties of PDMS/RGO/PDMS strain sensor were observed.

## 8.2 Future research

A variety of types of future research can follow the work presented in this dissertation. With respect to the materials aspect, this dissertation introduces three types of nano-carbons (MWNT, RGO, and GNP) dispersed into PDMS composites and polymerized by NIR photo-assisted method. In the future, it could be valuable to study C<sub>60</sub>/PDMS, GO/PDMS and graphite/PDMS composites using NIR photon-assisted polymerization and compare the difference effects of different dimension fillers in the process of NIR photon-assisted polymerization. We only use one type of silicone polymer PDMS as a matrix polymer, other kinds of polymer are suggested to be studied as matrix materials. In this dissertation, halogen lamp with wide range of NIR photons is used to synergize nano-carbon/polymer composites, however specific wavelengths of NIR have not been studied.

In the physical aspect of NIR photon-assisted polymerization, we used Raman to analyze average signal on the sample surface with 1  $\mu\text{m}$   $\times$  1  $\mu\text{m}$ . Alternatively, a co-localized Raman-AFM system can be used to study the precise interface area which is on sub-micrometer scale, offering more precise results. Besides, this dissertation studied the mechanism by using XPS. Many other techniques can be used towards progress in the future. Nuclear magnetic resonance (NMR) can be a good try. Polymer oligomer, crosslinker and nano-carbons can be first functionalized with other groups including <sup>13</sup>C and then synergized by different polymerization methods. Following <sup>13</sup>C can be tested in NMR system to fully understand the bonds change during NIR photon-assisted polymerization.

In this dissertation, we report high Young's modulus and high load transfer in those NIR light treated nano-carbon/PDMS composites due to strong interface. It is possible that strong interface will also enhance the electrical and thermal properties of nano-carbon/polymer composites. Investigation of these properties will give more perspective angles of NIR photon-assisted polymerization.

In engineering aspects, plenty of potential applications can be developed. The RGO film transfer method shown in Chapter 7 can be used to transfer large RGO film or GNP films, and those films patterned into complex electrical circuits. NIR photon-assisted polymerization can be potentially used to develop nanocarbon/polymer composites MEMS device with high toughness. Since NIR photon-assisted polymerization does not need a conventional oven, which enables fast and large-scale film polymerization.

## REFERENCES

1. Bledzki, A.K. and O. Faruk, *Wood fibre reinforced polypropylene composites: Effect of fibre geometry and coupling agent on physico-mechanical properties*. Applied Composite Materials, 2003. **10**(6): p. 365-379.
2. Kim, Y.H., S.H. Yoon, S.H. Jang, Y.K. Lee, Y.T. Sung, H.S. Lee, and W.N. Kim, *Effects of Fiber Characteristics on the Rheological and Mechanical Properties of Polycarbonate/Carbon Fiber Composites*. Composite Interfaces, 2009. **16**(4-6): p. 477-491.
3. Fu, S.Y., Y.W. Mai, B. Lauke, and C.Y. Yue, *Synergistic effect on the fracture toughness of hybrid short glass fiber and short carbon fiber reinforced polypropylene composites*. Materials Science and Engineering a-Structural Materials Properties Microstructure and Processing, 2002. **323**(1-2): p. 326-335.
4. Sun, Z.Y., Y. Yang, W.H. Qin, S.T. Ren, and G. Wu, *Experimental study on flexural behavior of concrete beams reinforced by steel-fiber reinforced polymer composite bars*. Journal of Reinforced Plastics and Composites, 2012. **31**(24): p. 1737-1745.
5. Kita, K., N. Kondo, Y. Izutsu, and H. Kita, *Joining of alumina by using polymer blend method*. Journal of the Ceramic Society of Japan, 2012. **120**(1406): p. 408-412.
6. Schadler, L.S., S.K. Kumar, B.C. Benicewicz, S.L. Lewis, and S.E. Harton, *Linda S. Schadler, Sanat K. Kumar, Brian C. Benicewicz, Sarah L. Lewis and Shane E. Harton (2007). Designed Interfaces in Polymer Nanocomposites: A Fundamental Viewpoint. MRS Bulletin, 32, pp 335-340 doi:10.1557/mrs2007.232 MRS Bulletin, 2007. 32(04): p. 335-340.*
7. Cadek, M., J.N. Coleman, K.P. Ryan, V. Nicolosi, G. Bister, A. Fonseca, J.B. Nagy, K. Szostak, F. Béguin, and W.J. Blau, *Reinforcement of Polymers with Carbon Nanotubes: The Role of Nanotube Surface Area*. Nano Letters, 2004. **4**(2): p. 353-356.
8. Chang, T.E., A. Kisliuk, S.M. Rhodes, W.J. Brittain, and A.P. Sokolov, *Conductivity and mechanical properties of well-dispersed single-wall carbon nanotube/polystyrene composite*. Polymer, 2006. **47**(22): p. 7740-7746.
9. Coleman, J.N., U. Khan, W.J. Blau, and Y.K. Gun'ko, *Small but strong: A review of the mechanical properties of carbon nanotube-polymer composites*. Carbon, 2006. **44**(9): p. 1624-1652.
10. Iijima, S., *Helical microtubules of graphitic carbon*. Nature, 1991. **354**(6348): p. 56-58.
11. Novoselov, K.S., A.K. Geim, S.V. Morozov, D. Jiang, Y. Zhang, S.V. Dubonos, I.V. Grigorieva, and A.A. Firsov, *Electric Field Effect in Atomically Thin Carbon Films*. Science, 2004. **306**(5696): p. 666-669.
12. Njuguna, B. and K. Pielichowski, *Polymer nanocomposites for aerospace applications: Properties*. Advanced Engineering Materials, 2003. **5**(11): p. 769-778.
13. Garces, J.M., D.J. Moll, J. Bicerano, R. Fibiger, and D.G. McLeod, *Polymeric nanocomposites for automotive applications*. Advanced Materials, 2000. **12**(23): p. 1835-1839.

14. Bonavolonta, C., M. Valentino, C. Meola, and G.M. Carlomagno, *NDT of polymer nanocomposite for structural applications using electromagnetic techniques*. International Journal of Applied Electromagnetics and Mechanics, 2012. **39**(1-4): p. 363-368.
15. Majeed, K., M. Jawaid, A. Hassan, A. Abu Bakar, H. Khalil, A.A. Salema, and I. Inuwa, *Potential materials for food packaging from nanoclay/natural fibres filled hybrid composites*. Materials & Design, 2013. **46**: p. 391-410.
16. Burris, D.L., B. Boesl, G.R. Bourne, and W.G. Sawyer, *Polymeric nanocomposites for tribological applications*. Macromolecular Materials and Engineering, 2007. **292**(4): p. 387-402.
17. Hule, R.A. and D.J. Pochan, *Polymer Nanocomposites for Biomedical Applications*. MRS Bulletin, 2007. **32**(04): p. 354-358.
18. Huang, X., X. Qi, F. Boey, and H. Zhang, *Graphene-based composites*. Chemical Society Reviews, 2012. **41**(2): p. 666-686.
19. Schadler, L.S., S.C. Giannaris, and P.M. Ajayan, *Load transfer in carbon nanotube epoxy composites*. Applied Physics Letters, 1998. **73**(26): p. 3842-3844.
20. Zhu, J., J.D. Kim, H.Q. Peng, J.L. Margrave, V.N. Khabashesku, and E.V. Barrera, *Improving the dispersion and integration of single-walled carbon nanotubes in epoxy composites through functionalization*. Nano Letters, 2003. **3**(8): p. 1107-1113.
21. Mitchell, C.A., J.L. Bahr, S. Arepalli, J.M. Tour, and R. Krishnamoorti, *Dispersion of functionalized carbon nanotubes in polystyrene*. Macromolecules, 2002. **35**(23): p. 8825-8830.
22. Hagenmueller, R., F.M. Du, J.E. Fischer, and K.I. Winey, *Interfacial in situ polymerization of single wall carbon nanotube/nylon 6,6 nanocomposites*. Polymer, 2006. **47**(7): p. 2381-2388.
23. Satishkumar, B.C., A. Govindaraj, J. Mofokeng, G.N. Subbanna, and C.N.R. Rao, *Novel experiments with carbon nanotubes: Opening, filling, closing and functionalizing nanotubes*. Journal of Physics B-Atomic Molecular and Optical Physics, 1996. **29**(21): p. 4925-4934.
24. Kuznetsova, A., D.B. Mawhinney, V. Naumenko, J.T. Yates, J. Liu, and R.E. Smalley, *Enhancement of adsorption inside of single-walled nanotubes: opening the entry ports*. Chemical Physics Letters, 2000. **321**(3-4): p. 292-296.
25. Dyke, C.A. and J.M. Tour, *Covalent functionalization of single-walled carbon nanotubes for materials applications*. Journal of Physical Chemistry A, 2004. **108**(51): p. 11151-11159.
26. Du, F.M., J.E. Fischer, and K.I. Winey, *Effect of nanotube alignment on percolation conductivity in carbon nanotube/polymer composites*. Physical Review B, 2005. **72**(12).
27. Jia, Z. and C.L. Xu, J.; Wei, B.; Wu, D.; Zhu, C, Xinxing Tan Cailiao, 1999. **14**: p. 32-36.
28. Jia, Z.W., Z.; Xu, C.; and J.W. Liang, B.; Wu, D.; Zhang, Z., Qinghua Daxue Xuebao, Ziran Kexueban, 2000. **40**: p. 14-16.
29. Zhang, W.D., L. Shen, I.Y. Phang, and T.X. Liu, *Carbon nanotubes reinforced nylon-6 composite prepared by simple melt-compounding*. Macromolecules, 2004. **37**(2): p. 256-259.
30. Moniruzzaman, M., J. Chattopadhyay, W.E. Billups, and K.I. Winey, *Tuning the mechanical properties of SWNT/Nylon 6,10 composites with flexible spacers at the interface*. Nano Letters, 2007. **7**(5): p. 1178-1185.
31. Lee, C., X.D. Wei, J.W. Kysar, and J. Hone, *Measurement of the elastic properties and intrinsic strength of monolayer graphene*. Science, 2008. **321**(5887): p. 385-388.
32. Gong, L., I.A. Kinloch, R.J. Young, I. Riaz, R. Jalil, and K.S. Novoselov, *Interfacial Stress Transfer in a Graphene Monolayer Nanocomposite*. Advanced Materials, 2010. **22**(24): p. 2694-+.

33. Young, R.J., L. Gong, I.A. Kinloch, I. Riaz, R. Jalil, and K.S. Novoselov, *Strain Mapping in a Graphene Monolayer Nanocomposite*. *Acs Nano*, 2011. **5**(4): p. 3079-3084.
34. Srivastava, I., R.J. Mehta, Z.Z. Yu, L. Schadler, and N. Koratkar, *Raman study of interfacial load transfer in graphene nanocomposites*. *Applied Physics Letters*, 2011. **98**(6).
35. Rafiee, M.A., W. Lu, A.V. Thomas, A. Zandiatashbar, J. Rafiee, J.M. Tour, and N.A. Koratkar, *Graphene Nanoribbon Composites*. *Acs Nano*, 2010. **4**(12): p. 7415-7420.
36. Song, P.G., Z.H. Cao, Y.Z. Cai, L.P. Zhao, Z.P. Fang, and S.Y. Fu, *Fabrication of exfoliated graphene-based polypropylene nanocomposites with enhanced mechanical and thermal properties*. *Polymer*, 2011. **52**(18): p. 4001-4010.
37. El Achaby, M., F.E. Arrakhiz, S. Vaudreuil, A.E. Qaiss, M. Bousmina, and O. Fassi-Fehri, *Mechanical, thermal, and rheological properties of graphene-based polypropylene nanocomposites prepared by melt mixing*. *Polymer Composites*, 2012. **33**(5): p. 733-744.
38. Kalaitzidou, K., H. Fukushima, and L.T. Drzal, *Mechanical properties and morphological characterization of exfoliated graphite-polypropylene nanocomposites*. *Composites Part a-Applied Science and Manufacturing*, 2007. **38**(7): p. 1675-1682.
39. Wakabayashi, K., P.J. Brunner, J. Masuda, S.A. Hewlett, and J.M. Torkelson, *Polypropylene-graphite nanocomposites made by solid-state shear pulverization: Effects of significantly exfoliated, unmodified graphite content on physical, mechanical and electrical properties*. *Polymer*, 2010. **51**(23): p. 5525-5531.
40. Raghu, A.V., Y.R. Lee, H.M. Jeong, and C.M. Shin, *Preparation and Physical Properties of Waterborne Polyurethane/Functionalized Graphene Sheet Nanocomposites*. *Macromolecular Chemistry and Physics*, 2008. **209**(24): p. 2487-2493.
41. Nguyen, D.A., Y.R. Lee, A.V. Raghu, H.M. Jeong, C.M. Shin, and B.K. Kim, *Morphological and physical properties of a thermoplastic polyurethane reinforced with functionalized graphene sheet*. *Polymer International*, 2009. **58**(4): p. 412-417.
42. Kim, H., Y. Miura, and C.W. Macosko, *Graphene/Polyurethane Nanocomposites for Improved Gas Barrier and Electrical Conductivity*. *Chemistry of Materials*, 2010. **22**(11): p. 3441-3450.
43. Khan, U., P. May, A. O'Neill, and J.N. Coleman, *Development of stiff, strong, yet tough composites by the addition of solvent exfoliated graphene to polyurethane*. *Carbon*, 2010. **48**(14): p. 4035-4041.
44. Hernandez, Y., V. Nicolosi, M. Lotya, F.M. Blighe, Z.Y. Sun, S. De, I.T. McGovern, B. Holland, M. Byrne, Y.K. Gun'ko, J.J. Boland, P. Niraj, G. Duesberg, S. Krishnamurthy, R. Goodhue, J. Hutchison, V. Scardaci, A.C. Ferrari, and J.N. Coleman, *High-yield production of graphene by liquid-phase exfoliation of graphite*. *Nature Nanotechnology*, 2008. **3**(9): p. 563-568.
45. Gomez-Navarro, C., M. Burghard, and K. Kern, *Elastic properties of chemically derived single graphene sheets*. *Nano Letters*, 2008. **8**(7): p. 2045-2049.
46. Lerf, A., H.Y. He, M. Forster, and J. Klinowski, *Structure of graphite oxide revisited*. *Journal of Physical Chemistry B*, 1998. **102**(23): p. 4477-4482.
47. Kam, N.W.S., M. O'Connell, J.A. Wisdom, and H.J. Dai, *Carbon nanotubes as multifunctional biological transporters and near-infrared agents for selective cancer cell destruction*. *Proceedings of the National Academy of Sciences of the United States of America*, 2005. **102**(33): p. 11600-11605.
48. Iijima, S. and T. Ichihashi, *Single-shell carbon nanotubes of 1-nm diameter*. *Nature*, 1993. **363**(6430): p. 603-605.
49. Shao, N., S. Lu, E. Wickstrom, and B. Panchapakesan, *Integrated molecular targeting of IGF1R and HER2 surface receptors and destruction of breast cancer cells using single wall carbon nanotubes*. *Nanotechnology*, 2007. **18**(31).

50. Levi-Polyachenko, N.H., E.J. Merkel, B.T. Jones, D.L. Carroll, and J.H. Stewart, *Rapid Photothermal Intracellular Drug Delivery Using Multiwalled Carbon Nanotubes*. *Molecular Pharmaceutics*, 2009. **6**(4): p. 1092-1099.
51. Lu, S.X. and B. Panchapakesan, *Optically driven nanotube actuators*. *Nanotechnology*, 2005. **16**(11): p. 2548-2554.
52. Lu, Y., D.B. Shao, and S.C. Chen, *Laser-assisted photothermal imprinting of nanocomposite*. *Applied Physics Letters*, 2004. **85**(9): p. 1604-1606.
53. Boukai, A.I., Y. Bunimovich, J. Tahir-Kheli, J.K. Yu, W.A. Goddard, and J.R. Heath, *Silicon nanowires as efficient thermoelectric materials*. *Nature*, 2008. **451**(7175): p. 168-171.
54. Chan, C.K., H.L. Peng, G. Liu, K. McIlwrath, X.F. Zhang, R.A. Huggins, and Y. Cui, *High-performance lithium battery anodes using silicon nanowires*. *Nature Nanotechnology*, 2008. **3**(1): p. 31-35.
55. Law, M., J. Goldberger, and P.D. Yang, *Semiconductor nanowires and nanotubes*. *Annual Review of Materials Research*, 2004. **34**: p. 83-122.
56. Murphy, C.J., A.M. Gole, J.W. Stone, P.N. Sisco, A.M. Alkilany, E.C. Goldsmith, and S.C. Baxter, *Gold Nanoparticles in Biology: Beyond Toxicity to Cellular Imaging*. *Accounts of Chemical Research*, 2008. **41**(12): p. 1721-1730.
57. West, J.L. and N.J. Halas, *Engineered nanomaterials for biophotonics applications: Improving sensing, imaging, and therapeutics*. *Annual Review of Biomedical Engineering*, 2003. **5**: p. 285-292.
58. Geim, A.K. and K.S. Novoselov, *The rise of graphene*. *Nature Materials*, 2007. **6**(3): p. 183-191.
59. Geim, A.K., *Graphene: Status and Prospects*. *Science*, 2009. **324**(5934): p. 1530-1534.
60. Baughman, R.H., A.A. Zakhidov, and W.A. de Heer, *Carbon nanotubes - the route toward applications*. *Science*, 2002. **297**(5582): p. 787-792.
61. Deheer, W.A., A. Chatelain, and D. Ugarte, *A CARBON NANOTUBE FIELD-EMISSION ELECTRON SOURCE*. *Science*, 1995. **270**(5239): p. 1179-1180.
62. Tans, S.J., A.R.M. Verschueren, and C. Dekker, *Room-temperature transistor based on a single carbon nanotube*. *Nature*, 1998. **393**(6680): p. 49-52.
63. Cheung, C.L., A. Kurtz, H. Park, and C.M. Lieber, *Diameter-Controlled Synthesis of Carbon Nanotubes*. *The Journal of Physical Chemistry B*, 2002. **106**(10): p. 2429-2433.
64. Dresselhaus, M.S., G. Dresselhaus, and R. Saito, *Phys. Rev.*, 1992. **45**: p. 6234-6234.
65. Rinzler, A.G., J. Liu, H. Dai, P. Nikolaev, C.B. Huffman, F.J. Rodríguez-Macías, P.J. Boul, A.H. Lu, D. Heymann, D.T. Colbert, R.S. Lee, J.E. Fischer, A.M. Rao, P.C. Eklund, and R.E. Smalley, *Large-scale purification of single-wall carbon nanotubes: process, product, and characterization*. *Applied Physics A: Materials Science & Processing*, 1998. **67**(1): p. 29-37.
66. Nikolaev, P., M.J. Bronikowski, R.K. Bradley, F. Rohmund, D.T. Colbert, K.A. Smith, and R.E. Smalley, *Gas-phase catalytic growth of single-walled carbon nanotubes from carbon monoxide*. *Chemical Physics Letters*, 1999. **313**(1-2): p. 91-97.
67. Endo, M., K. Takeuchi, K. Kobori, K. Takahashi, H.W. Kroto, and A. Sarkar, *Pyrolytic carbon nanotubes from vapor-grown carbon fibers*. *Carbon*, 1995. **33**(7): p. 873-881.
68. Dresselhaus, M.S., G. Dresselhaus, and P. Avouris, *Carbon Nanotubes Synthesis, Structure, Properties, and Applications*. 1 ed. *Topics in Applied Physics*. Vol. 80. 2001, Berlin: Springer. 447.
69. White, C.T., D.H. Robertson, and J.W. Mintmire, *Helical and rotational symmetries of nanoscale graphitic tubules*. *Physical Review B*, 1993. **47**(9): p. 5485.
70. Liu, Y., A. Dobrinsky, and B.I. Yakobson, *Graphene Edge from Armchair to Zigzag: The Origins of Nanotube Chirality?* *Physical Review Letters*, 2010. **105**(23): p. 235502.
71. Wallace, P.R., *The Band Theory of Graphite*. *Physical Review*, 1947. **71**(9): p. 622-634.

72. Al-Temimy, A., C. Riedl, and U. Starke, *Low temperature growth of epitaxial graphene on SiC induced by carbon evaporation*. Applied Physics Letters, 2009. **95**(23): p. 231907-231907-3.
73. Zhan, N., M. Olmedo, G.P. Wang, and J.L. Liu, *Graphene based nickel nanocrystal flash memory*. Applied Physics Letters, 2011. **99**(11).
74. Kosynkin, D.V., A.L. Higginbotham, A. Sinitskii, J.R. Lomeda, A. Dimiev, B.K. Price, and J.M. Tour, *Longitudinal unzipping of carbon nanotubes to form graphene nanoribbons*. Nature, 2009. **458**(7240): p. 872-U5.
75. Choucair, M., P. Thordarson, and J.A. Stride, *Gram-scale production of graphene based on solvothermal synthesis and sonication*. Nature Nanotechnology, 2009. **4**(1): p. 30-33.
76. Bae, S., H. Kim, Y. Lee, X.F. Xu, J.S. Park, Y. Zheng, J. Balakrishnan, T. Lei, H.R. Kim, Y.I. Song, Y.J. Kim, K.S. Kim, B. Ozyilmaz, J.H. Ahn, B.H. Hong, and S. Iijima, *Roll-to-roll production of 30-inch graphene films for transparent electrodes*. Nature Nanotechnology, 2010. **5**(8): p. 574-578.
77. Moon, I.K., J. Lee, R.S. Ruoff, and H. Lee, *Reduced graphene oxide by chemical graphitization*. Nature Communications, 2010. **1**.
78. Pei, S. and H.-M. Cheng, *The reduction of graphene oxide*. Carbon, 2012. **50**(9): p. 3210-3228.
79. Loomis, J., B. King, and B. Panchapakesan, *Layer dependent mechanical responses of graphene composites to near-infrared light*. Applied Physics Letters, 2012. **100**(7).
80. Gómez-Navarro, C., J.C. Meyer, R.S. Sundaram, A. Chuvilin, S. Kurasch, M. Burghard, K. Kern, and U. Kaiser, *Atomic Structure of Reduced Graphene Oxide*. Nano Letters, 2010. **10**(4): p. 1144-1148.
81. Russo, S., M.F. Craciun, T. Khodlkov, M. Koshino, M. Yamamoto, and S. Tarucha, *Electronic Transport Properties of Few-Layer Graphene Materials, Graphene - Synthesis, Characterization, Properties and Applications*, 2011.
82. Partoens, B. and F.M. Peeters, *From graphene to graphite: Electronic structure around the K point*. Physical Review B, 2006. **74**(7): p. 075404.
83. Boehm, H.P., A. Clauss, G. Fischer, and U. Hofmann. *Surface properties of extremely thin graphite lamellae*. in *Proc. of the Fifth Conference on Carbon*. 1962. London: Pergamon Press.
84. Allen, M.J., V.C. Tung, and R.B. Kaner, *Honeycomb Carbon: A Review of Graphene*. Chemical Reviews, 2009. **110**(1): p. 132-145.
85. Robertson, D.H., D.W. Brenner, and J.W. Mintmire, *Energetics of nanoscale graphitic tubules*. Physical Review B, 1992. **45**: p. 12592-12595.
86. Yakobson, B.I., C.J. Brabec, and J. Bernholc, *Nanomechanics of Carbon Tubes: Instabilities beyond Linear Response*. Physical Review Letters, 1996. **76**: p. 2511.
87. Treacy, M.M.J., T.W. Ebbesen, and J.M. Gibson, *Exceptionally high Young's modulus observed for individual carbon nanotubes*. Nature, 1996. **381**(6584): p. 678-680.
88. Krishnan, A., E. Dujardin, T.W. Ebbesen, P.N. Yianilos, and M.M.J. Treacy, *Young's modulus of single-walled nanotubes*. Physical Review B, 1998. **58**(20): p. 14013-14019.
89. Yu, M.-F., B.S. Files, S. Arepalli, and R.S. Ruoff, *Tensile Loading of Ropes of Single Wall Carbon Nanotubes and their Mechanical Properties*. Physical Review Letters, 2000. **84**: p. 5552-5555.
90. Yu, M.-F., O. Lourie, M.J. Dyer, K. Moloni, T.F. Kelly, and R.S. Ruoff, *Strength and Breaking Mechanism of Multiwalled Carbon Nanotubes Under Tensile Load*. Science, 2000. **287**(5453): p. 637-640.
91. Ebbesen, T.W., H.J. Lezec, H. Hiura, J.W. Bennett, H.F. Ghaemi, and T. Thio, *Electrical conductivity of individual carbon nanotubes*. Nature, 1996. **382**(6586): p. 54-56.
92. Iijima, S., Nature, 1991. **354**: p. 56-56.

93. Fujii, M., X. Zhang, H. Xie, H. Ago, K. Takahashi, T. Ikuta, H. Abe, and T. Shimizu, *Measuring the Thermal Conductivity of a Single Carbon Nanotube*. Physical Review Letters, 2005. **95**(6): p. 065502.
94. Liu, X., T.H. Metcalf, J.T. Robinson, B.H. Houston, and F. Scarpa, *Shear Modulus of Monolayer Graphene Prepared by Chemical Vapor Deposition*. Nano Letters, 2012. **12**(2): p. 1013-1017.
95. Lee, C., X. Wei, J.W. Kysar, and J. Hone, *Measurement of the Elastic Properties and Intrinsic Strength of Monolayer Graphene*. Science, 2008. **321**(5887): p. 385-388.
96. Frank, I.W., D.M. Tanenbaum, A.M. Van der Zande, and P.L. McEuen, *Mechanical properties of suspended graphene sheets*. Journal of Vacuum Science & Technology B, 2007. **25**(6): p. 2558-2561.
97. Lee, H.-J., E. Kim, J.-G. Yook, and J. Jung, *Intrinsic characteristics of transmission line of graphenes at microwave frequencies*. Applied Physics Letters, 2012. **100**(22): p. 223102-3.
98. Balandin, A.A., S. Ghosh, W. Bao, I. Calizo, D. Teweldebrhan, F. Miao, and C.N. Lau, *Superior Thermal Conductivity of Single-Layer Graphene*. Nano Letters, 2008. **8**(3): p. 902-907.
99. Robinson, J.T., M. Zalalutdinov, J.W. Baldwin, E.S. Snow, Z. Wei, P. Sheehan, and B.H. Houston, *Wafer-scale Reduced Graphene Oxide Films for Nanomechanical Devices*. Nano Letters, 2008. **8**(10): p. 3441-3445.
100. Gómez-Navarro, C., R.T. Weitz, A.M. Bittner, M. Scolari, A. Mews, M. Burghard, and K. Kern, *Electronic Transport Properties of Individual Chemically Reduced Graphene Oxide Sheets*. Nano Letters, 2007. **7**(11): p. 3499-3503.
101. Timo, S., R.B. Brian, C.S. Niklas, and P. Dimos, *An electrical method for the measurement of the thermal and electrical conductivity of reduced graphene oxide nanostructures*. Nanotechnology, 2009. **20**(40): p. 405704.
102. López, V., R.S. Sundaram, C. Gómez-Navarro, D. Olea, M. Burghard, J. Gómez-Herrero, F. Zamora, and K. Kern, *Chemical Vapor Deposition Repair of Graphene Oxide: A Route to Highly-Conductive Graphene Monolayers*. Advanced Materials, 2009. **21**(46): p. 4683-4686.
103. Su, Q., S. Pang, V. Alijani, C. Li, X. Feng, and K. Müllen, *Composites of Graphene with Large Aromatic Molecules*. Advanced Materials, 2009. **21**(31): p. 3191-3195.
104. Shamsa, M., W.L. Liu, A.A. Balandin, C. Casiraghi, W.I. Milne, and A.C. Ferrari, *Thermal conductivity of diamond-like carbon films*. Applied Physics Letters, 2006. **89**(16).
105. Georgantzinou, S.K., G.I. Giannopoulos, and N.K. Anifantis, *Numerical investigation of elastic mechanical properties of graphene structures*. Materials & Design, 2010. **31**(10): p. 4646-4654.
106. Poot, M. and H.S.J. van der Zant, *Nanomechanical properties of few-layer graphene membranes*. Applied Physics Letters, 2008. **92**(6).
107. Ghosh, S., W. Bao, D.L. Nika, S. Subrina, E.P. Pokatilov, C.N. Lau, and A.A. Balandin, *Dimensional crossover of thermal transport in few-layer graphene*. Nature Materials, 2010. **9**(7): p. 555-558.
108. Sperling, L.H., *Introduction to physical polymer science*, 2001, Lehigh University, Bethlehem, Pennsylvania: John Wiley & Sons, Inc.
109. Allen, K.W., *Polymer interfaces: structure and strength*, Richard P. Wool. Carl Hanser Verlag, Munich, Vienna, New York, 1995. pp. xvii + 494, price DM 178.00, £72.00. ISBN 3-446-16140-6. Polymer International, 1995. **38**(3): p. 305-306.
110. McDonald, J.C. and G.M. Whitesides, *Poly(dimethylsiloxane) as a Material for Fabricating Microfluidic Devices*. Accounts of Chemical Research, 2002. **35**(7): p. 491-499.

111. Cai, D., A. Neyer, R. Kuckuk, and H.M. Heise, *Raman, mid-infrared, near-infrared and ultraviolet–visible spectroscopy of PDMS silicone rubber for characterization of polymer optical waveguide materials*. Journal of Molecular Structure, 2010. **976**(1–3): p. 274-281.
112. Xu, Y., W. Hong, H. Bai, C. Li, and G. Shi, *Strong and ductile poly(vinyl alcohol)/graphene oxide composite films with a layered structure*. Carbon, 2009. **47**(15): p. 3538-3543.
113. Ramanathan, T., S. Stankovich, D.A. Dikin, H. Liu, H. Shen, S.T. Nguyen, and L.C. Brinson, *Graphitic nanofillers in PMMA nanocomposites—An investigation of particle size and dispersion and their influence on nanocomposite properties*. Journal of Polymer Science Part B: Polymer Physics, 2007. **45**(15): p. 2097-2112.
114. Kim, I.-H. and Y.G. Jeong, *Polylactide/exfoliated graphite nanocomposites with enhanced thermal stability, mechanical modulus, and electrical conductivity*. Journal of Polymer Science Part B: Polymer Physics, 2010. **48**(8): p. 850-858.
115. Zhang, H.-B., W.-G. Zheng, Q. Yan, Y. Yang, J.-W. Wang, Z.-H. Lu, G.-Y. Ji, and Z.-Z. Yu, *Electrically conductive polyethylene terephthalate/graphene nanocomposites prepared by melt compounding*. Polymer, 2010. **51**(5): p. 1191-1196.
116. Cochet, M., W.K. Maser, A.M. Benito, M.A. Callejas, M.T. Martinez, J.-M. Benoit, J. Schreiber, and O. Chauvet, *Synthesis of a new polyaniline/nanotube composite: "" polymerisation and charge transfer through site-selective interaction*. Chemical Communications, 2001(16): p. 1450-1451.
117. Yu, A., P. Ramesh, M.E. Itkis, E. Bekyarova, and R.C. Haddon, *Graphite Nanoplatelet–Epoxy Composite Thermal Interface Materials*. The Journal of Physical Chemistry C, 2007. **111**(21): p. 7565-7569.
118. Wang, D.-W., F. Li, J. Zhao, W. Ren, Z.-G. Chen, J. Tan, Z.-S. Wu, I. Gentle, G.Q. Lu, and H.-M. Cheng, *Fabrication of Graphene/Polyaniline Composite Paper via In Situ Anodic Electropolymerization for High-Performance Flexible Electrode*. ACS Nano, 2009. **3**(7): p. 1745-1752.
119. Verdejo, R., F. Barroso-Bujans, M.A. Rodriguez-Perez, J. Antonio de Saja, and M.A. Lopez-Manchado, *Functionalized graphene sheet filled silicone foam nanocomposites*. Journal of Materials Chemistry, 2008. **18**(19): p. 2221-2226.
120. Hill, D.E., Y. Lin, A.M. Rao, L.F. Allard, and Y.P. Sun, *Functionalization of carbon nanotubes with polystyrene*. Macromolecules, 2002. **35**(25): p. 9466-9471.
121. Kim, K.S., D.J. Bae, J.R. Kim, K.A. Park, S.C. Lim, J.J. Kim, W.B. Choi, C.Y. Park, and Y.H. Lee, *Modification of Electronic Structures of a Carbon Nanotube by Hydrogen Functionalization*. Advanced Materials, 2002. **14**(24): p. 1818-1821.
122. Hirsch, A., *Functionalization of Single-Walled Carbon Nanotubes*. Angewandte Chemie International Edition, 2002. **41**(11): p. 1853-1859.
123. Gong, X., J. Liu, S. Baskaran, R.D. Voise, and J.S. Young, *Surfactant-Assisted Processing of Carbon Nanotube/Polymer Composites*. Chemistry of Materials, 2000. **12**(4): p. 1049-1052.
124. Shaffer, M.S.P. and A.H. Windle, *Fabrication and Characterization of Carbon Nanotube/Poly(vinyl alcohol) Composites*. Advanced Materials, 1999. **11**(11): p. 937-941.
125. Cadek, M., J.N. Coleman, V. Barron, K. Hedicke, and W.J. Blau, *Morphological and mechanical properties of carbon-nanotube-reinforced semicrystalline and amorphous polymer composites*. Applied Physics Letters, 2002. **81**(27): p. 5123-5125.
126. Andrews, R., D. Jacques, D.L. Qian, and T. Rantell, *Multiwalled carbon nanotubes: Synthesis and application*. Accounts of Chemical Research, 2002. **35**(12): p. 1008-1017.
127. Qian, D., E.C. Dickey, R. Andrews, and T. Rantell, *Load transfer and deformation mechanisms in carbon nanotube-polystyrene composites*. Applied Physics Letters, 2000. **76**(20): p. 2868-2870.

128. Xu, X.J., M.M. Thwe, C. Shearwood, and K. Liao, *Mechanical properties and interfacial characteristics of carbon-nanotube-reinforced epoxy thin films*. Applied Physics Letters, 2002. **81**(15): p. 2833-2835.
129. Biercuk, M.J., M.C. Llaguno, M. Radosavljevic, J.K. Hyun, A.T. Johnson, and J.E. Fischer, *Carbon nanotube composites for thermal management*. Applied Physics Letters, 2002. **80**(15): p. 2767-2769.
130. Sandler, J., M.S.P. Shaffer, T. Prasse, W. Bauhofer, K. Schulte, and A.H. Windle, *Development of a dispersion process for carbon nanotubes in an epoxy matrix and the resulting electrical properties*. Polymer, 1999. **40**(21): p. 5967-5971.
131. Lozano, K., J. Bonilla-Rios, and E.V. Barrera, *A study on nanofiber-reinforced thermoplastic composites (II): Investigation of the mixing rheology and conduction properties*. Journal of Applied Polymer Science, 2001. **80**(8): p. 1162-1172.
132. Blanchet, G.B., C.R. Fincher, and F. Gao, *Polyaniline nanotube composites: A high-resolution printable conductor*. Applied Physics Letters, 2003. **82**(8): p. 1290-1292.
133. Curran, S.A., P.M. Ajayan, W.J. Blau, D.L. Carroll, J.N. Coleman, A.B. Dalton, A.P. Davey, A. Drury, B. McCarthy, S. Maier, and A. Strevens, *A composite from poly(m-phenylenevinylene-co-2,5-dioctoxy-p-phenylenevinylene) and carbon nanotubes: A novel material for molecular optoelectronics*. Advanced Materials, 1998. **10**(14): p. 1091-+.
134. Romero, D.B., M. Carrard, W. DeHeer, and L. Zuppiroli, *A carbon nanotube organic semiconducting polymer heterojunction*. Advanced Materials, 1996. **8**(11): p. 899-&.
135. Ago, H., K. Petritsch, M.S.P. Shaffer, A.H. Windle, and R.H. Friend, *Composites of carbon nanotubes and conjugated polymers for photovoltaic devices*. Advanced Materials, 1999. **11**(15): p. 1281-+.
136. Kymakis, E. and G.A.J. Amaratunga, *Single-wall carbon nanotube/conjugated polymer photovoltaic devices*. Applied Physics Letters, 2002. **80**(1): p. 112-114.
137. Chen, Y.C., N.R. Raravikar, L.S. Schadler, P.M. Ajayan, Y.P. Zhao, T.M. Lu, G.C. Wang, and X.C. Zhang, *Ultrafast optical switching properties of single-wall carbon nanotube polymer composites at 1.55  $\mu$  m*. Applied Physics Letters, 2002. **81**(6): p. 975-977.
138. Stankovich, S., D.A. Dikin, R.D. Piner, K.A. Kohlhaas, A. Kleinhammes, Y. Jia, Y. Wu, S.T. Nguyen, and R.S. Ruoff, *Synthesis of graphene-based nanosheets via chemical reduction of exfoliated graphite oxide*. Carbon, 2007. **45**(7): p. 1558-1565.
139. Yu, A., P. Ramesh, M.E. Itkis, E. Bekyarova, and R.C. Haddon, *Graphite nanoplatelet-epoxy composite thermal interface materials*. Journal of Physical Chemistry C, 2007. **111**(21): p. 7565-7569.
140. Du, J. and H.-M. Cheng, *The Fabrication, Properties, and Uses of Graphene/Polymer Composites*. Macromolecular Chemistry and Physics, 2012. **213**(10-11): p. 1060-1077.
141. Vadukumpully, S., J. Paul, N. Mahanta, and S. Valiyaveetil, *Flexible conductive graphene/poly(vinyl chloride) composite thin films with high mechanical strength and thermal stability*. Carbon, 2011. **49**(1): p. 198-205.
142. Bao, C., Y. Guo, L. Song, and Y. Hu, *Poly(vinyl alcohol) nanocomposites based on graphene and graphite oxide: a comparative investigation of property and mechanism*. Journal of Materials Chemistry, 2011. **21**(36): p. 13942-13950.
143. Wang, J., H. Hu, X. Wang, C. Xu, M. Zhang, and X. Shang, *Preparation and mechanical and electrical properties of graphene nanosheets-poly(methyl methacrylate) nanocomposites via in situ suspension polymerization*. Journal of Applied Polymer Science, 2011. **122**(3): p. 1866-1871.
144. Xie, S.H., Y.Y. Liu, and J.Y. Li, *Comparison of the effective conductivity between composites reinforced by graphene nanosheets and carbon nanotubes*. Applied Physics Letters, 2008. **92**(24): p. 243121-3.

145. Chen, Z., W. Ren, L. Gao, B. Liu, S. Pei, and H.-M. Cheng, *Three-dimensional flexible and conductive interconnected graphene networks grown by chemical vapour deposition*. *Nature Materials*, 2011. **10**(6): p. 424-428.
146. Fang, M., K. Wang, H. Lu, Y. Yang, and S. Nutt, *Covalent polymer functionalization of graphene nanosheets and mechanical properties of composites*. *Journal of Materials Chemistry*, 2009. **19**(38): p. 7098-7105.
147. Huang, C., H. Bai, C. Li, and G. Shi, *A graphene oxide/hemoglobin composite hydrogel for enzymatic catalysis in organic solvents*. *Chemical Communications*, 2011. **47**(17): p. 4962-4964.
148. Jorio, A., *Raman Spectroscopy in Graphene-Based Systems: Prototypes for Nanoscience and Nanometrology*. ISRN Nanotechnology, 2012. **2012**: p. 16.
149. Ferraro, J.R., K. Nakamoto, and C.W. Brown, *Introductory Raman Spectroscopy* 2003: Elsevier.
150. Gouadec, G. and P. Colomban, *Raman Spectroscopy of nanomaterials: How spectra relate to disorder, particle size and mechanical properties*. *Progress in Crystal Growth and Characterization of Materials*, 2007. **53**(1): p. 1-56.
151. Malard, L.M., M.A. Pimenta, G. Dresselhaus, and M.S. Dresselhaus, *Raman spectroscopy in graphene*. *Physics Reports*, 2009. **473**(5-6): p. 51-87.
152. Siegbahn, K. and U. Kungl. Vetenskaps-societeten i, *ESCA; atomic, molecular and solid state structure studied by means of electron spectroscopy* 1967, Uppsala: Almqvist & Wiksells.
153. Lee, Y.S., T.H. Cho, B.K. Lee, J.S. Rho, K.H. An, and Y.H. Lee, *Surface properties of fluorinated single-walled carbon nanotubes*. *Journal of Fluorine Chemistry*, 2003. **120**(2): p. 99-104.
154. Chen, P., X. Wu, X. Sun, J. Lin, W. Ji, and K.L. Tan, *Electronic Structure and Optical Limiting Behavior of Carbon Nanotubes*. *Physical Review Letters*, 1999. **82**(12): p. 2548-2551.
155. Droppa Jr, R., P. Hammer, A.C.M. Carvalho, M.C. dos Santos, and F. Alvarez, *Incorporation of nitrogen in carbon nanotubes*. *Journal of Non-Crystalline Solids*, 2002. **299-302, Part 2**(0): p. 874-879.
156. Levita, G., A. Marchetti, and A. Lazzeri, *Fracture of ultrafine calcium carbonate/polypropylene composites*. *Polymer Composites*, 1989. **10**(1): p. 39-43.
157. Cooper, C.A. and R.J. Young, *Investigation of structure/property relationships in particulate composites through the use of Raman spectroscopy*. *Journal of Raman Spectroscopy*, 1999. **30**(10): p. 929-938.
158. Bollet, F., C. Galiotis, and M.J. Reece, *Measurement of strain distribution in fibre reinforced ceramic matrix composites*. *Composites Part A: Applied Science and Manufacturing*, 1996. **27**(9): p. 729-735.
159. Frank, O., G. Tsoukleri, J. Parthenios, K. Papagelis, I. Riaz, R. Jalil, K.S. Novoselov, and C. Galiotis, *Compression Behavior of Single-Layer Graphenes*. *ACS Nano*, 2010. **4**(6): p. 3131-3138.
160. Wagner, H.D., O. Lourie, Y. Feldman, and R. Tenne, *Stress-induced fragmentation of multiwall carbon nanotubes in a polymer matrix*. *Applied Physics Letters*, 1998. **72**(2): p. 188-190.
161. Gao, Y., L.Y. Li, P.H. Tan, L.Q. Liu, and Z. Zhang, *Application of Raman spectroscopy in carbon nanotube-based polymer composites*. *Chinese Science Bulletin*, 2010. **55**(35): p. 3978-3988.
162. Vigolo, B., B. Vincent, J. Eschbach, P. Bourson, J.F. Mareche, E. Mcrae, A. Muller, A. Soldatov, J.M. Hiver, A. Dahoun, and D. Rouxel, *Multiscale Characterization of Single-Walled Carbon Nanotube/Polymer Composites by Coupling Raman and Brillouin Spectroscopy*. *Journal of Physical Chemistry C*, 2009. **113**(41): p. 17648-17654.

163. de la Vega, A., J.Z. Kovacs, W. Bauhofer, and K. Schulte, *Combined Raman and dielectric spectroscopy on the curing behaviour and stress build up of carbon nanotube-epoxy composites*. Composites Science and Technology, 2009. **69**(10): p. 1540-1546.
164. Bult, J., R. Duncan, P.M. Ajayan, and L.S. Schadler, *Evaluation of interfacial load transfer in carbon nanotube composites using polarized Raman spectroscopy*. Abstracts of Papers of the American Chemical Society, 2009. **237**.
165. Lefrant, S., M. Baibarac, and I. Baltog, *Raman and FTIR spectroscopy as valuable tools for the characterization of polymer and carbon nanotube based composites*. Journal of Materials Chemistry, 2009. **19**(32): p. 5690-5704.
166. Singamaneni, S., V. Shevchenko, and V. Bliznyuk, *Unusual ignition behavior of polyurethane/carbon nanotube composites with a He-Ne laser excitation (632.8 nm) during micro-Raman spectroscopy*. Carbon, 2006. **44**(11): p. 2191-2195.
167. Kuzmany, H., R. Pfeiffer, M. Hulman, and C. Kramberger, *Raman spectroscopy of fullerenes and fullerene-nanotube composites*. Philosophical Transactions of the Royal Society of London Series a-Mathematical Physical and Engineering Sciences, 2004. **362**(1824): p. 2375-2406.
168. Zhao, Q. and H.D. Wagner, *Raman spectroscopy of carbon-nanotube-based composites*. Philosophical Transactions of the Royal Society of London Series a-Mathematical Physical and Engineering Sciences, 2004. **362**(1824): p. 2407-2424.
169. Ruan, S.L., P. Gao, X.G. Yang, and T.X. Yu, *Toughening high performance ultrahigh molecular weight polyethylene using multiwalled carbon nanotubes*. Polymer, 2003. **44**(19): p. 5643-5654.
170. Loomis, J., B. King, and B. Panchapakesan, *Layer dependent mechanical responses of graphene composites to near infrared light*. Applied Physics Letters, 2012. **100**(073108).
171. Lachman, N., C. Bartholome, P. Miaudet, M. Maugey, P. Poulin, and H.D. Wagner, *Raman Response of Carbon Nanotube/PVA Fibers under Strain*. Journal of Physical Chemistry C, 2009. **113**(12): p. 4751-4754.
172. Mu, M.F., S. Osswald, Y. Gogotsi, and K.I. Winey, *An in situ Raman spectroscopy study of stress transfer between carbon nanotubes and polymer*. Nanotechnology, 2009. **20**(33).
173. Xu, P., J. Loomis, and B. Panchapakesan, *Photo-thermal polymerization of nanotube/polymer composites: Effects of load transfer and mechanical strength*. Applied Physics Letters, 2012. **100**(13).
174. Yadav, S.K. and J.W. Cho, *Functionalized graphene nanoplatelets for enhanced mechanical and thermal properties of polyurethane nanocomposites*. Applied Surface Science, 2013. **266**(0): p. 360-367.
175. Goncalves, G., P.A.A.P. Marques, A. Barros-Timmons, I. Bdkin, M.K. Singh, N. Emami, and J. Gracio, *Graphene oxide modified with PMMA via ATRP as a reinforcement filler*. Journal of Materials Chemistry, 2010. **20**(44): p. 9927-9934.
176. Pramoda, K.P., H. Hussain, H.M. Koh, H.R. Tan, and C.B. He, *Covalent bonded polymer-graphene nanocomposites*. Journal of Polymer Science Part A: Polymer Chemistry, 2010. **48**(19): p. 4262-4267.
177. Cao, Y., J. Feng, and P. Wu, *Preparation of organically dispersible graphene nanosheet powders through a lyophilization method and their poly(lactic acid) composites*. Carbon, 2010. **48**(13): p. 3834-3839.
178. Wang, Y., Z. Shi, J. Fang, H. Xu, and J. Yin, *Graphene oxide/polybenzimidazole composites fabricated by a solvent-exchange method*. Carbon, 2011. **49**(4): p. 1199-1207.
179. Wang, X., H. Yang, L. Song, Y. Hu, W. Xing, and H. Lu, *Morphology, mechanical and thermal properties of graphene-reinforced poly(butylene succinate) nanocomposites*. Composites Science and Technology, 2011. **72**(1): p. 1-6.

180. Liang, J., Y. Huang, L. Zhang, Y. Wang, Y. Ma, T. Guo, and Y. Chen, *Molecular-Level Dispersion of Graphene into Poly(vinyl alcohol) and Effective Reinforcement of their Nanocomposites*. *Advanced Functional Materials*, 2009. **19**(14): p. 2297-2302.
181. Xu, Z. and C. Gao, *In situ Polymerization Approach to Graphene-Reinforced Nylon-6 Composites*. *Macromolecules*, 2010. **43**(16): p. 6716-6723.
182. Lee, Y.R., A.V. Raghunathan, H.M. Jeong, and B.K. Kim, *Properties of Waterborne Polyurethane/Functionalized Graphene Sheet Nanocomposites Prepared by an in situ Method*. *Macromolecular Chemistry and Physics*, 2009. **210**(15): p. 1247-1254.
183. Polschikov, S.V., P.M. Nedorezova, A.N. Klyamkina, A.A. Kovalchuk, A.M. Aladyshev, A.N. Shchegolikhin, V.G. Shevchenko, and V.E. Muradyan, *Composite materials of graphene nanoplatelets and polypropylene, prepared by in situ polymerization*. *Journal of Applied Polymer Science*, 2013. **127**(2): p. 904-911.
184. Wang, X., Y. Hu, L. Song, H. Yang, W. Xing, and H. Lu, *In situ polymerization of graphene nanosheets and polyurethane with enhanced mechanical and thermal properties*. *Journal of Materials Chemistry*, 2011. **21**(12): p. 4222-4227.
185. Luong, N.D., U. Hippi, J.T. Korhonen, A.J. Soininen, J. Ruokolainen, L.-S. Johansson, J.-D. Nam, L.H. Sinh, and J. Seppälä, *Enhanced mechanical and electrical properties of polyimide film by graphene sheets via in situ polymerization*. *Polymer*, 2011. **52**(23): p. 5237-5242.
186. El Achaby, M., F.Z. Arrakhiz, S. Vaudreuil, E.M. Essassi, A. Qaiss, and M. Bousmina, *Preparation and characterization of melt-blended graphene nanosheets-poly(vinylidene fluoride) nanocomposites with enhanced properties*. *Journal of Applied Polymer Science*, 2013. **127**(6): p. 4697-4707.
187. Kalaitzidou, K., H. Fukushima, and L.T. Drzal, *Mechanical properties and morphological characterization of exfoliated graphite-polypropylene nanocomposites*. *Composites Part A: Applied Science and Manufacturing*, 2007. **38**(7): p. 1675-1682.
188. Potts, J.R., S. Murali, Y. Zhu, X. Zhao, and R.S. Ruoff, *Microwave-Exfoliated Graphite Oxide/Polycarbonate Composites*. *Macromolecules*, 2011. **44**(16): p. 6488-6495.
189. El Achaby, M., F.-E. Arrakhiz, S. Vaudreuil, A. el Kacem Qaiss, M. Bousmina, and O. Fassi-Fehri, *Mechanical, thermal, and rheological properties of graphene-based polypropylene nanocomposites prepared by melt mixing*. *Polymer Composites*, 2012. **33**(5): p. 733-744.
190. Zhang, J. and Z. Qiu, *Morphology, Crystallization Behavior, and Dynamic Mechanical Properties of Biodegradable Poly( $\epsilon$ -caprolactone)/Thermally Reduced Graphene Nanocomposites*. *Industrial & Engineering Chemistry Research*, 2011. **50**(24): p. 13885-13891.
191. Ajayan, P.M., L.S. Schadler, C. Giannaris, and A. Rubio, *Single-walled carbon nanotube-polymer composites: Strength and weakness*. *Advanced Materials*, 2000. **12**(10): p. 750-+.
192. Ferrari, A.C., *Raman spectroscopy of graphene and graphite: Disorder, electron-phonon coupling, doping and nonadiabatic effects*. *Solid State Communications*, 2007. **143**(1-2): p. 47-57.
193. Rao, C.N.R., K. Biswas, K.S. Subrahmanyam, and A. Govindaraj, *Graphene, the new nanocarbon*. *Journal of Materials Chemistry*, 2009. **19**(17): p. 2457-2469.
194. Englert, J.M., C. Dotzer, G.A. Yang, M. Schmid, C. Papp, J.M. Gottfried, H.P. Steinrück, E. Spiecker, F. Hauke, and A. Hirsch, *Covalent bulk functionalization of graphene*. *Nature Chemistry*, 2011. **3**(4): p. 279-286.
195. Nicolle, J., D. Machon, P. Poncharal, O. Pierre-Louis, and A. San-Miguel, *Pressure-Mediated Doping in Graphene*. *Nano Letters*, 2011. **11**(9): p. 3564-3568.

196. Gupta, A.K., C. Nisoli, P.E. Lammert, V.H. Crespi, and P.C. Eklund, *Curvature-induced D-band Raman scattering in folded graphene*. Journal of Physics-Condensed Matter, 2010. **22**(33).
197. Lee, J.S., S. Ryu, K. Yoo, I.S. Choi, W.S. Yun, and J. Kim, *Origin of gate hysteresis in carbon nanotube field-effect transistors*. Journal of Physical Chemistry C, 2007. **111**(34): p. 12504-12507.
198. Ci, L., J. Suhr, V. Pushparaj, X. Zhang, and P.M. Ajayan, *Continuous carbon nanotube reinforced composites*. Nano Letters, 2008. **8**(9): p. 2762-2766.
199. El-Lawindy, A.M.Y. and S.B. El-Guiziri, *Strain energy density of carbon-black-loaded rubber vulcanizates*. Journal of Physics D-Applied Physics, 2000. **33**(15): p. 1894-1901.
200. Hwang, G.L., Y.T. Shieh, and K.C. Hwang, *Efficient load transfer to polymer-grafted multiwalled carbon nanotubes in polymer composites*. Advanced Functional Materials, 2004. **14**(5): p. 487-491.
201. Shen, G.A., S. Namilae, and N. Chandra, *Load transfer issues in the tensile and compressive behavior of multiwall carbon nanotubes*. Materials Science and Engineering a-Structural Materials Properties Microstructure and Processing, 2006. **429**(1-2): p. 66-73.
202. Leeuw, T.K., D.A. Tsyboulski, P.N. Nikolaev, S.M. Bachilo, S. Arepalli, and R.B. Weisman, *Strain measurements on individual single-walled carbon nanotubes in a polymer host: Structure-dependent spectral shifts and load transfer*. Nano Letters, 2008. **8**(3): p. 826-831.
203. Wang, S.R., R. Liang, B. Wang, and C. Zhang, *Load-transfer in functionalized carbon nanotubes/polymer composites*. Chemical Physics Letters, 2008. **457**(4-6): p. 371-375.
204. Chakoli, A.N., W. Cai, S. Jiehe, and J.T. Feng, *Efficient Load Transfer to Functionalized Carbon Nanotubes as Reinforcement in Polymer Nanocomposites*. International Journal of Modern Physics B, 2009. **23**(6-7): p. 1401-1406.
205. Tsai, J.L. and T.C. Lu, *Investigating the load transfer efficiency in carbon nanotubes reinforced nanocomposites*. Composite Structures, 2009. **90**(2): p. 172-179.
206. Ray, M.C., R.G. de Villoria, and B.L. Wardle, *Load Transfer Analysis in Short Carbon Fibers with Radially-Aligned Carbon Nanotubes Embedded in a Polymer Matrix*. Journal of Advanced Materials, 2009. **41**(4): p. 82-94.
207. Pietro, D.S., C. Tang, and C.F. Chen, *Enhancing interwall load transfer by vacancy defects in carbon nanotubes*. Applied Physics Letters, 2012. **100**(3).
208. Viet, N.V. and W.S. Kuo, *Load transfer in fractured carbon nanotubes under tension*. Composites Part B-Engineering, 2012. **43**(2): p. 332-339.
209. Lourie, O. and H.D. Wagner, *Evidence of stress transfer and formation of fracture clusters in carbon nanotube-based composites*. Composites Science and Technology, 1999. **59**(6): p. 975-977.
210. Prasad, K.E., B. Das, U. Maitra, U. Ramamurty, and C.N.R. Rao, *Extraordinary synergy in the mechanical properties of polymer matrix composites reinforced with 2 nanocarbons*. Proceedings of the National Academy of Sciences of the United States of America, 2009. **106**(32): p. 13186-13189.
211. Shin, M.K., B. Lee, S.H. Kim, J.A. Lee, G.M. Spinks, S. Gambhir, G.G. Wallace, M.E. Kozlov, R.H. Baughman, and S.J. Kim, *Synergistic toughening of composite fibres by self-alignment of reduced graphene oxide and carbon nanotubes*. Nature Communications, 2012. **3**.
212. Yu, A.P., P. Ramesh, X.B. Sun, E. Bekyarova, M.E. Itkis, and R.C. Haddon, *Enhanced Thermal Conductivity in a Hybrid Graphite Nanoplatelet - Carbon Nanotube Filler for Epoxy Composites*. Advanced Materials, 2008. **20**(24): p. 4740-+.
213. Wang, R.R., J. Sun, L. Gao, C.H. Xu, and J. Zhang, *Fibrous nanocomposites of carbon nanotubes and graphene-oxide with synergetic mechanical and actuative performance*. Chemical Communications, 2011. **47**(30): p. 8650-8652.

214. Zhao, Q., M.D. Frogley, and H.D. Wagner, *Direction-sensitive strain-mapping with carbon nanotube sensors*. Composites Science and Technology, 2002. **62**(1): p. 147-150.
215. Zhao, Q. and H.D. Wagner, *Two-dimensional strain mapping in model fiber-polymer composites using nanotube Raman sensing*. Composites Part a-Applied Science and Manufacturing, 2003. **34**(11): p. 1219-1225.
216. Loomis, J. and B. Panchapakesan, *Dimensional dependence of photomechanical response in carbon nanostructure composites: a case for carbon-based mixed-dimensional systems*. Nanotechnology, 2012. **23**(21).
217. Loomis, J., B. King, T. Burkhead, P. Xu, N. Bessler, E. Terentjev, and B. Panchapakesan, *Graphene-nanoplatelet-based photomechanical actuators*. Nanotechnology, 2012. **23**(4).
218. Lu, S.X. and B. Panchapakesan, *Photomechanical responses of carbon nanotube/polymer actuators*. Nanotechnology, 2007. **18**(30).
219. Lu, S.X., S.V. Ahir, E.M. Terentjev, and B. Panchapakesan, *Alignment dependent mechanical responses of carbon nanotubes to light*. Applied Physics Letters, 2007. **91**(10).
220. Lu, S.X., Y. Liu, N. Shao, and B. Panchapakesan, *Nanotube micro-opto-mechanical systems*. Nanotechnology, 2007. **18**(6).
221. Lu, S.X. and B. Panchapakesan, *Nanotube micro-optomechanical actuators*. Applied Physics Letters, 2006. **88**(25).
222. Lu, S. and B. Panchapakesan, *All-optical micromirrors from nanotube MOMS with wavelength selectivity*. Journal of Microelectromechanical Systems, 2007. **16**(6): p. 1515-1523.
223. Wang, Y.Y., Z.H. Ni, T. Yu, Z.X. Shen, H.M. Wang, Y.H. Wu, W. Chen, and A.T.S. Wee, *Raman studies of monolayer graphene: The substrate effect*. Journal of Physical Chemistry C, 2008. **112**(29): p. 10637-10640.
224. Ferrari, A.C., J.C. Meyer, V. Scardaci, C. Casiraghi, M. Lazzeri, F. Mauri, S. Piscanec, D. Jiang, K.S. Novoselov, S. Roth, and A.K. Geim, *Raman spectrum of graphene and graphene layers*. Physical Review Letters, 2006. **97**(18).
225. Xu, P., J. Loomis, and B. Panchapakesan, *Photo-thermal polymerization of nanotube/polymer composites: Effects of load transfer and mechanical strength*. Applied Physics Letters, 2012. **100**: p. 131907.
226. James E. Mark, B.E., *Rubberlike Elasticity, A Molecular Primer* 2007: Cambridge University Press.
227. Coleman, J.N., U. Khan, W.J. Blau, and Y.K. Gun'ko, *Small but strong: A review of the mechanical properties of carbon nanotube-polymer composites*. Carbon, 2006. **44**(9): p. 1624-1652.
228. Li, C.Y. and T.W. Chou, *Elastic moduli of multi-walled carbon nanotubes and the effect of van der Waals forces*. Composites Science and Technology, 2003. **63**(11): p. 1517-1524.
229. Gupta, S.S. and R.C. Batra, *Elastic Properties and Frequencies of Free Vibrations of Single-Layer Graphene Sheets*. Journal of Computational and Theoretical Nanoscience, 2010. **7**(10): p. 2151-2164.
230. Ahir, S.V., E.M. Terentjev, S.X. Lu, and B. Panchapakesan, *Thermal fluctuations, stress relaxation, and actuation in carbon nanotube networks*. Physical Review B, 2007. **76**(16).
231. Loomis, J., P. Xu, X. Fan, R.W. Cohn, and B. Panchapakesan, *Two Axis Photomechanical nanopositioners based on graphene elastomer composites*. Scientific Reports (in review), 2013.
232. Peng, X., L. James, K. Ben, and P. Balaji, *Synergy among binary (MWNT, SLG) nano-carbons in polymer nano-composites: a Raman study*. Nanotechnology, 2012. **23**(31): p. 315706.

233. Hu, S.H., Y.W. Chen, W.T. Hung, I.W. Chen, and S.Y. Chen, *Quantum-Dot-Tagged Reduced Graphene Oxide Nanocomposites for Bright Fluorescence Bioimaging and Photothermal Therapy Monitored In Situ*. *Advanced Materials*, 2012. **24**(13): p. 1748-1754.
234. Markovic, Z.M., L.M. Harhaji-Trajkovic, B.M. Todorovic-Markovic, D.P. Kepic, K.M. Arskin, S.P. Jovanovic, A.C. Pantovic, M.D. Dramicanin, and V.S. Trajkovic, *In vitro comparison of the photothermal anticancer activity of graphene nanoparticles and carbon nanotubes*. *Biomaterials*, 2011. **32**(4): p. 1121-1129.
235. Robinson, J.T., S.M. Tabakman, Y.Y. Liang, H.L. Wang, H.S. Casalongue, D. Vinh, and H.J. Dai, *Ultrasmall Reduced Graphene Oxide with High Near-Infrared Absorbance for Photothermal Therapy*. *Journal of the American Chemical Society*, 2011. **133**(17): p. 6825-6831.
236. Carpin, L.B., L.R. Bickford, G. Agollah, T.K. Yu, R. Schiff, Y. Li, and R.A. Drezek, *Immunoconjugated gold nanoshell-mediated photothermal ablation of trastuzumab-resistant breast cancer cells*. *Breast Cancer Research and Treatment*, 2011. **125**(1): p. 27-34.
237. Kessentini, S. and D. Barchiesi, *Quantitative comparison of optimized nanorods, nanoshells and hollow nanospheres for photothermal therapy*. *Biomedical Optics Express*, 2012. **3**(3): p. 590-604.
238. Madsen, S.J., S.K. Baek, A.R. Makkouk, T. Krasieva, and H. Hirschberg, *Macrophages as Cell-Based Delivery Systems for Nanoshells in Photothermal Therapy*. *Annals of Biomedical Engineering*, 2012. **40**(2): p. 507-515.
239. Zedan, A.F., S. Moussa, J. Ternner, G. Atkinson, and M.S. El-Shall, *Ultrasmall Gold Nanoparticles Anchored to Graphene and Enhanced Photothermal Effects by Laser Irradiation of Gold Nanostructures in Graphene Oxide Solutions*. *Acs Nano*, 2013. **7**(1): p. 627-636.
240. Chen, C.L., L.R. Kuo, S.Y. Lee, Y.K. Hwu, S.W. Chou, C.C. Chen, F.H. Chang, K.H. Lin, D.H. Tsai, and Y.Y. Chen, *Photothermal cancer therapy via femtosecond-laser-excited FePt nanoparticles*. *Biomaterials*, 2013. **34**(4): p. 1128-1134.
241. Cote, L.J., R. Cruz-Silva, and J.X. Huang, *Flash Reduction and Patterning of Graphite Oxide and Its Polymer Composite*. *Journal of the American Chemical Society*, 2009. **131**(31): p. 11027-11032.
242. Sherlock, S.P., S.M. Tabakman, L.M. Xie, and H.J. Dai, *Photothermally Enhanced Drug Delivery by Ultrasmall Multifunctional FeCo/Graphitic Shell Nanocrystals*. *Acs Nano*, 2011. **5**(2): p. 1505-1512.
243. Tian, B., C. Wang, S. Zhang, L.Z. Feng, and Z. Liu, *Photothermally Enhanced Photodynamic Therapy Delivered by Nano-Graphene Oxide*. *Acs Nano*, 2011. **5**(9): p. 7000-7009.
244. Bagri, A., C. Mattevi, M. Acik, Y.J. Chabal, M. Chhowalla, and V.B. Shenoy, *Structural evolution during the reduction of chemically derived graphene oxide*. *Nature Chemistry*, 2010. **2**(7): p. 581-587.
245. Sharma, V., M. Dhayal, Govind, S.M. Shivaprasad, and S.C. Jain, *Surface characterization of plasma-treated and PEG-grafted PDMS for micro fluidic applications*. *Vacuum*, 2007. **81**(9): p. 1094-1100.
246. Andrey, S. and Z. Margit, *Gibbs free energy and equilibrium states in the Si/Si oxide systems*. *Journal of Physics: Condensed Matter*, 2012. **24**(38): p. 385403.
247. Okada, K., Y. Kameshima, and A. Yasumori, *Chemical Shifts of Silicon X-ray Photoelectron Spectra by Polymerization Structures of Silicates*. *Journal of the American Ceramic Society*, 1998. **81**(7): p. 1970-1972.

248. Hamilton, D.S. and D.A. Nicewicz, *Direct Catalytic Anti-Markovnikov Hydroetherification of Alkenols*. Journal of the American Chemical Society, 2012. **134**(45): p. 18577-18580.
249. Gadek, A., A. Kochel, and T. Szymanska-Buzar, *Activation of the Si-H bond of Et<sub>2</sub>SiH<sub>2</sub> in photochemical reaction with W(CO)<sub>6</sub>: Spectroscopic characterization of intermediate W-Si compounds and the revisited crystal structure of the bis {(μ-η(2)-hydridodiethylsilyl)tetracarbonyltungsten(I)} complex {W(μ-η(2)-H-SiEt<sub>2</sub>)(CO)<sub>4</sub>}(<sub>2</sub>)*. Journal of Organometallic Chemistry, 2007. **692**(17): p. 3765-3777.
250. Mattes, S.L. and S. Farid, *PHOTOCHEMICAL ELECTRON-TRANSFER REACTIONS OF 1,1-DIARYLETHYLENES*. Journal of the American Chemical Society, 1986. **108**(23): p. 7356-7361.
251. Dobie, W.B. and C.G. Isaac Peter, Electric Resistance Strain Gauges, 1948.
252. Thomson, W., *On the electro-dynamic qualities of metals: Effects of magnetization on the electric conductivity of nickel and of iron*. Proc. R. Soc. London, 1856. **8**: p. 546-550.
253. EE, S., METHOD APPARATUS MAK, 1944.
254. Bardeen, J. and W. Shockley, *Deformation Potentials and Mobilities in Non-Polar Crystals*. Physical Review, 1950. **80**(1): p. 72-80.
255. Mason, W. and R. Thurston, *USE OF PIEZORESISTIVE MATERIALS IN THE MEASUREMENT OF DISPLACEMENT, FORCE, AND TORQUE*. Journal of the Acoustical society of america, 1957. **29**(10): p. 1096-1101.
256. Yamada, T., Y. Hayamizu, Y. Yamamoto, Y. Yomogida, A. Izadi-Najafabadi, D.N. Futaba, and K. Hata, *A stretchable carbon nanotube strain sensor for human-motion detection*. Nature Nanotechnology, 2011. **6**(5): p. 296-301.
257. Obitayo, W. and T. Liu, *A Review: Carbon Nanotube-Based Piezoresistive Strain Sensors*. Journal of Sensors, 2012. **2012**: p. 15.
258. Tombler, T.W., C.W. Zhou, L. Alexseyev, J. Kong, H.J. Dai, L. Lei, C.S. Jayanthi, M.J. Tang, and S.Y. Wu, *Reversible electromechanical characteristics of carbon nanotubes under local-probe manipulation*. Nature, 2000. **405**(6788): p. 769-772.
259. Pereira, V.M. and A.H. Castro Neto, *Strain Engineering of Graphene's Electronic Structure*. Physical Review Letters, 2009. **103**(4): p. 046801.
260. Cao, J., Q. Wang, and H.J. Dai, *Electromechanical properties of metallic, quasimetallic, and semiconducting carbon nanotubes under stretching*. Physical Review Letters, 2003. **90**(15).
261. Mattmann, C., F. Clemens, and G. Troester, *Sensor for measuring strain in textile*. Sensors, 2008. **8**(6): p. 3719-3732.
262. Hu, N., Y. Karube, M. Arai, T. Watanabe, C. Yan, Y. Li, Y.L. Liu, and H. Fukunaga, *Investigation on sensitivity of a polymer/carbon nanotube composite strain sensor*. Carbon, 2010. **48**(3): p. 680-687.
263. Pham, G.T., Y.-B. Park, Z. Liang, C. Zhang, and B. Wang, *Processing and modeling of conductive thermoplastic/carbon nanotube films for strain sensing*. Composites Part B: Engineering, 2008. **39**(1): p. 209-216.
264. Chao-Xuan, L. and C. Jin-Woo, *Strain-Dependent Resistance of PDMS and Carbon Nanotubes Composite Microstructures*. Nanotechnology, IEEE Transactions on, 2010. **9**(5): p. 590-595.
265. Lee, Y., S. Bae, H. Jang, S. Jang, S.-E. Zhu, S.H. Sim, Y.I. Song, B.H. Hong, and J.-H. Ahn, *Wafer-Scale Synthesis and Transfer of Graphene Films*. Nano Letters, 2010. **10**(2): p. 490-493.
266. Bae, S.-H., Y. Lee, B.K. Sharma, H.-J. Lee, J.-H. Kim, and J.-H. Ahn, *Graphene-based transparent strain sensor*. Carbon, 2013. **51**(0): p. 236-242.
267. Wang, Y., R. Yang, Z. Shi, L. Zhang, D. Shi, E. Wang, and G. Zhang, *Super-Elastic Graphene Ripples for Flexible Strain Sensors*. ACS Nano, 2011. **5**(5): p. 3645-3650.

268. Fu, X.-W., Z.-M. Liao, J.-X. Zhou, Y.-B. Zhou, H.-C. Wu, R. Zhang, G. Jing, J. Xu, X. Wu, W. Guo, and D. Yu, *Strain dependent resistance in chemical vapor deposition grown graphene*. Applied Physics Letters, 2011. **99**(21): p. 213107.
269. Shaoxin, L., L. Ye, S. Ning, and P. Balaji, *Nanotube micro-opto-mechanical systems*. Nanotechnology, 2007. **18**(6): p. 065501.
270. Lu, S. and B. Panchapakesan, *Nanotube micro-optomechanical actuators*. Applied Physics Letters, 2006. **88**(25): p. 253107-3.
271. Hanson, D.E., M. Hawley, R. Houlton, K. Chitanvis, P. Rae, E.B. Orler, and D.A. Wroblewski, *Stress softening experiments in silica-filled polydimethylsiloxane provide insight into a mechanism for the Mullins effect*. Polymer, 2005. **46**(24): p. 10989-10995.
272. Wu, J.-T., X.-H. Shi, and Y.-J. Wei, *Tunable band structures of polycrystalline graphene by external and mismatch strains*. Acta Mechanica Sinica, 2012. **28**(6): p. 1539-1544.
273. Yang, L., M.P. Anantram, J. Han, and J.P. Lu, *Band-gap change of carbon nanotubes: effect of small uniaxial and torsional strain*. Physical Review B, 1999. **60**.

## APPENDICES

### Appendix A

#### Sample preparation and test of MWNT/PDMS composites

Samples were comprised of small amounts (0.01-1 wt. %) of MWNTs (98.4% carbon, Applied Nanotechnologies) dispersed within PDMS (Sylgard 184), a widely available commercial polymer. Homogenous dispersions of MWNTs in PDMS were prepared using a recently developed evaporative mixing fabrication process which involved sonicating an MWNT and isopropyl alcohol (IPA) solution for 4 h, evaporative mixing of PDMS base compound with the MWNT-IPA suspension for 24 h at 65 °C, addition of crosslinker (base compound: curing agent ratio is 10:1) and subsequent degas, crosslinking and polymerization, spin coating and baking, and finally post-bake relaxation for ~12 h [170]. In conventional curing, samples are heated in a vacuum oven at 125 °C for 30 m following addition of crosslinker and degasing (Figure 3.1(a)). At this time duration and temperature, the Young's modulus values become saturated indicating of the end of the crosslinking process. For the NIR light treatment, samples were exposed to varying levels of NIR radiation following crosslinker addition and degasing (Figure 3.1(b)).

The processing time and the NIR power level were optimized to achieve saturation in the Young's modulus values of pure PDMS. Following sample preparation, scanning electron microscopy (SEM) was used to investigate sample cross-sections and the nanotube/polymer interface.

In order to compare the load transfer values between conventional baked polymerization and NIR light treated polymerization, Raman spectroscopy was used to ascertain shift in the wavenumbers with increasing strains. The 632.8 nm line beam of a helium-neon laser in an inVia RENISHAW micro-Raman spectrometer was focused onto the sample surface through a  $\times 50$  objective lens, forming a laser spot  $\sim 3 \mu\text{m}$  in diameter. Strains were applied to the sample under the micro-Raman spectrometer by stretching the sample to a pre-determined length using a linear actuator. Raman measurements were conducted in at least 4 - 5 different locations in each sample for statistically confident values.

Finally, samples containing various fractions (0.01-1 wt. %) of MWNTs in PDMS were prepared and tested for their elastic moduli using both oven-baked and NIR photon irradiated samples. The specimen was prepared with 150  $\mu\text{m}$  in thickness, 3 mm in width, and 8 cm in length. The initial test length for the specimen is 4 cm. The Young's moduli of the samples were determined by calculating the stress-strain data within initial 0.5%. The strain rate for Young's modulus is 0.1 mm/s. For each composite, 3 specimens are tested. The effect of improvement in Young's modulus for different weight fractions of MWNTs and different levels of NIR radiation were studied. The change in Young's modulus was calculated based on the Young's modulus of the pure PDMS for both the

methods, and the percentage change was calculated based on increasing weight fractions of MWNTs for the same time and NIR power.

## Appendix B

### Sample preparation and test of RGO/PDMS and GNP/PDMS composites

Commercially obtained RGO (92% carbon, <8% oxygen) produced via thermal exfoliation reduction and hydrogen reduction of single layer graphene oxide) was purchased from ACS Materials. The RGO was used in its original form and not surface modified at any time. GNPs were purchased from Cheap tubes Inc. and were prepared by plasma exfoliation with >99% purity and ~3-5 layers. The number of layers were verified using SEM and was characterized in the past using layer dependent shifts in Raman spectroscopy [79]. Sylgard 184 silicone elastomer (Fisher Scientific) was chosen as the matrix because it is commonly used in industrial/scientific research and biocompatible.

Homogenous dispersion of graphene (1 wt. % of RGO and GNP for comparison) in PDMS was prepared using a shear mixing process. Steps included mixing known weight percentages of graphene fillers in PDMS base compound using a laboratory shear mixer at 300 rpm for 7 days at 25 C, addition of cross linkers (10:1 base compound: curing agent ratio), degas procedures, cross-linking and polymerization, spin coating and NIR photon-assisted polymerization.

SEM imaging was conducted on a Zeiss SUPRA 35VP field emission scanning electron microscope. The ~632.8 nm line beam of a helium-neon laser in an inVia RENISHAW micro-Raman spectrometer was focused onto the sample surface through a  $\times 50$  objective lens, forming a laser spot approximately 3  $\mu\text{m}$  in diameter. Tension trains were applied to the sample under the micro-Raman spectrometer by using a linear actuator that was able to precisely stretch the sample to predetermined length. For

compression strain, the composites films are bonded with PDMS bulk by plasma and compressed by linear actuator. A Gaussian profile was used to fit the Raman peaks. Raman measurements were conducted in at least 4-5 different locations in each sample for statistically confident values.

Samples containing 1 wt. % RGO or GNP in PDMS were prepared and tested for their Young's modulus until failure. Stress-strain curves and cyclic stress-strain curves were measured using a Rheometric Mechanical Analyzer (RMA, TA instruments-Waters LLC) for both RGO and GNP composites. The specimen was prepared with 150  $\mu\text{m}$  in thickness, 3 mm in width, and 8 cm in length. The initial test length for the specimen is 4 cm. The Young's moduli of the samples were determined by calculating the stress-strain data within initial 0.5% and the strain rate is 0.1 mm/s. For the cyclic mechanical test, three steps are provided: Step 1 is with 0.1 mm/s strain rate during 200 s; Step 2 is without strain change and keep for 130 s; Step 3 is with  $-0.1$  mm/s during 200 s. Cyclic mechanical testing was conducted on 10 samples for each RGO/PDMS sample to investigate stress-strain curves, toughness and strain energy density of the composites.

## Appendix C

### Sample preparation and test of MWNT<sub>x</sub>RGO<sub>1-x</sub>/PDMS composites

In our work, different binary mixtures of RGO and MWNTs were dispersed in the PDMS (Sylgard) matrix and these samples were used to study the synergistic effect on the load transfer and the mechanical strength. Because one can be viewed as 2D plates and the other are quasi-1D tubes, RGO (2D ACS Materiel) and MWNTs (98.4% carbon, Applied Nanotechnologies) were chosen for our study. It should be quite interesting to how the load transfer is changed when changing the relative weight ratio between the two nano-carbons in the binary nano-carbons/polymer composites. Specifically, a series of composites were prepared and investigated, including the composite with 1 wt. % of MWNTs as the reinforcement, the composite with 1 wt. % of RGO, and the composites with 1 wt. % of binary RGO/MWNT nano-carbons but with different relative ratios between RGO and MWNT.

To homogenously disperse the nano-carbons in PDMS, the above-mentioned evaporative mixing method was used, through sonication of the nano-carbon fillers in isopropyl alcohol (IPA) solution for 4 h, evaporative mixing of PDMS base compound with the nano-carbon-IPA suspension for 24 h at 65 °C, addition of cross-linker (base compound: curing agent ratio of 10:1) and subsequent degas, cross-linking and polymerization using NIR light for 240 min, and finally post-bake relaxation for 12 h. The process times and the NIR dose were optimized to achieve saturation of the Young's modulus values for pure PDMS. NIR cross-linking and polymerization of those samples through optical absorption and subsequent heating of the fillers to cross-link is a

paradigm that has been shown recently to improve both mechanical properties and interfacial shear strength without causing degradation to the nano-fillers [173]. Unlike the conventional crosslinking processes where samples are heated in a vacuum oven between ~90-120 °C for 30 min, the NIR polymerization enables heating of nanotubes inside the polymer matrix by illumination with NIR light (700-1100 nm). As discussed above, this has been reported to significantly strengthen the nanotube/polymer interface and enable higher load transfer [173]. The samples were prepared in batches using evaporative mixing and cross-linking. Each batch yielded five different samples both for characterization and measuring the mechanical property.

The prepared samples were first investigated by using SEM to examine the sample cross-sections and the nano-carbon/polymer interface. Raman spectroscopy was used to ascertain the Raman peak shift with increasing strains to compare the load transfer between adding single nano-carbon filler or binary mixtures of nano-carbon fillers in polymer matrix. The ~632.8 nm line beam of helium-neon laser in the inVia RENISHAW micro-Raman spectrometer was focused on the sample surface with the 50× objective lens, thus forming a laser spot of ~3 μm in diameter. Under the micro-Raman spectrometer, the tensile strain was applied to the samples by stretching the samples to the pre-determined length using a linear actuator. The compressive strain was applied to the sample by anchoring one end of the sample while using a linear actuator to push the other end to the pre-determined length. Raman measurements were conducted in at least 4-5 different locations in each sample for statistically confident values. Gaussian fittings were performed on all the interested Raman bands.

The elastic moduli ( $E$ ) were measured for the series of samples. . The specimen was prepared with 150  $\mu\text{m}$  in thickness, 3 mm in width, and 8 cm in length. The initial test length for the specimen is 4 cm. The synergistic effects in the Young's modulus were extracted by comparing the change in the  $E$  values of the pure PDMS, MWNT<sub>1.0</sub>/PDMS, RGO<sub>1.0</sub>/PDMS, and the composites with binary MWNT/RGO mixtures. The Young's moduli of the samples were determined by calculating the stress-strain data within initial 0.5%. The strain rate for Young's modulus test is 0.1 mm/s. The change in the Young's modulus was calculated with respect to the original Young's modulus of the pure PDMS. The percentage change was calculated for each sample.

For the photo-mechanical response study, the actuator samples of PDMS composites were mounted vertically between two clamps. The bottom clamp was attached to a weighted (70 g) base and placed on a high accuracy balance (Acculab ALC-80.4). The upper clamp was attached to an automated linear actuator that was in turn mounted to a high accuracy manual positioning stage. The laser diode was placed 75 mm from the middle of the test strip such that the illumination impacted perpendicularly to the PDMS surface. The deformation in the composite strips as a result of the NIR illumination caused a change in the weight reading on the balance. The stress test on each sample was conducted with the pre-strain value ranging from 3% to 25%. The timing sequence for each pre-strain value was 1 min relaxation wait followed by five cycles of NIR illumination: on for 60 s and then off for 30 s. The photo-mechanical stress was calculated by dividing the change of the induced force between the illumination-on state and the illumination-off state by the cross-sectional area of the samples.

## CURRICULUM VITAE

### PENG XU

#### EDUCATION:

08/2009 - Present            University of Louisville, Louisville, KY  
**Doctor of Philosophy** in Mechanical Engineering: GPA: 3.96/4.00  
Thesis Title “Near infrared photon-assisted polymerization: a paradigm in development of advanced polymer composites”

08/2009 – 04/2011        University of Louisville, Louisville, KY  
**Master of Science** in Mechanical Engineering: GPA: 4.00/4.00  
Thesis Title “Integration of Ag<sub>2</sub>Ga Nanoneedles on Batch Fabricated Micro-gripper for Material Property Measurement”

09/2005 - 07/2009        Hefei University of Technology, Hefei, China  
**Bachelor of Science** in Applied Physics: Rank: 10/99  
Thesis Title “Q-switched Er:YAG Laser System Design with Pockels Cell”

#### PROFESSIONAL EXPERIENCE:

08/2009—Present        University of Louisville, Louisville, USA  
Research Assistant, Small Systems Lab

09/2007—04/2008        Hefei University of Technology, Hefei, China  
Research Assistant, Micro-electronic Laboratory

06/2007—10/2007        Institute of Plasma Physics Chinese Academy of Sciences,  
Hefei, China

## LEADERSHIP:

- 10/2007-10/2008      Vice-President  
Student Union of Anhui Province
- President  
Student Union of Hefei University of Technology
- 10/2006-10/2007      Vice-President  
Student Union of Hefei University of Technology
- President  
Student Union of Feicui Campus of HFUT
- 09/2006-09/2007      Editor-in-chief  
The Book "Director of Freshmen"

## JOURNAL PUBLICATIONS:

- ◆ **P. Xu**, X. Fan, and B. Panchapakesan, "Near infra-red photon-assisted polymerization of graphene/polymer composites," manuscript in preparation to *Advanced Functional Materials*, expected date of submission, 2013
- ◆ J. Loomis, **P. Xu**, X. Fan, M. Fletcher, R. Cohn, and B. Panchapakesan, "Graphene/elastomer composite-based photo-thermal nanopositioners," *Scientific Reports*, under review.
- ◆ J. Loomis, **P. Xu**, and B. Panchapakesan, "Stimuli-responsive transformation in carbon nanotube/expanding microsphere-polymer composites," *Nanotechnology*, under review.
- ◆ **P. Xu**, J. Loomis, and B. Panchapakesan, "Load transfer and mechanical properties of chemically derived single layer graphene reinforcements in polymer composites," *Nanotechnology*, vol 23, p. 505713, 2012
- ◆ **P. Xu**, J. Loomis, B. King and B. Panchapakesan, "Synergy among Binary (MWNT, SLG) Nano-Carbons in Polymer Nano-Composites: A Raman Study," *Nanotechnology*, vol 23, p. 315706, 2012
- ◆ **P. Xu**, J. Loomis, and B. Panchapakesan, "Photo-thermal polymerization of nanotube/polymer composites: Effects of load transfer and mechanical strength," *Applied Physics Letters*, vol. 100, pp. 131907-5, 2012
- ◆ J. Loomis, B. King, T. Burkhead, **P. Xu**, N. Bessler, E.M. Terentjev, and B. Panchapakesan, "Graphene-nanoplatelet-based photomechanical actuators," *Nanotechnology*, vol. 23, p. 045501, 2012.
- ◆ B. Panchapakesan, R. Caprara, V. Velasco, J. Loomis, B. King, **P. Xu**, T. Burkhead, P. Sethu, L. Stallons, W. McGregor, S. Rai, G. Kloecker, and E. Wickstrom, "Micro- and nanotechnology approaches for capturing circulating tumor cells," *Cancer Nanotechnology*, vol. 1, pp. 3-11, 2010

- ◆ S. Lu, S. Ahir, V. Velasco, B. King, **P. Xu**, E.M. Terentjev, and B. Panchapakesan, “Photo-mechanical actuation of carbon nanotubes: mechanisms and applications in micro and nano-devices, “ *Journal of MicroNano Mechatronics* 5, 29-41, 2009

## CONFERENCE PUBLICATIONS:

- ◆ **P. Xu**, B. Panchapakesan, “Mechanical Properties of Reduced Graphene Polymer Composites,” *TechConnect World Conference and Expo 2013 Proceedings*, accepted, 2013
- ◆ **P. Xu**, J. Loomis, B. King and B. Panchapakesan, “Synergism in Binary (MWNT, SLG) Nano-carbons in Polymer Nano-composites: A Raman Study,” *in the proceedings of 2012 Fall MRS conference*, accepted, 2012
- ◆ J. Loomis, B. King, B. Burkhead, **P. Xu**, M. Terentjev E and B. Panchapakesan, “Photomechanical Response in Graphene Nanoplatelet Composites,” in *Tech Connect World 2012 Proceedings*, 2012
- ◆ B. Panchapakesan, **P. Xu** and J. Loomis, "Carbon based micro- and nano-opto-mechanical systems (C-MOMS/NOMS)", *Proc. SPIE 8107*, 810708, 2011
- ◆ **P. Xu**, M. Yazdanpanah and B. Panchapakesan, “Integration of Ag<sub>2</sub>Ga nanoneedles on batch fabricated micro-grippers for material property measurement,” oral presentation, The fourth Annual Nanotechnology Symposium, Sullivan University College of Pharmacy, Louisville, KY, 2011

## BOOK CHAPTERS

- ◆ B. Panchapakesan, T. Burkhead, B. King, **P. Xu**, J. Loomis, and E. Wickstrom, “Diagnostic and Therapeutic Applications of Carbon Nanotubes”, book chapter in “Biomedical Nanosensors”, Pan Stanford Publishing Pte. Ltd, 2012

## HONORS & AWARDS:

- ◆ University Research Tuition Award (2012)
- ◆ E-Expo Student Research Competition Award, first place in Mechanical Engineering (2010)
- ◆ Graduate assistantship (2009-2013)
- ◆ Provincial Triple-A Student (2008)
- ◆ "Wang Zhenghu" Business Management Scholarship (2007)
- ◆ Excellent League Member (2007)
- ◆ Excellent Member of Student Union (2007)
- ◆ “Social Activity” Scholarship (2007)
- ◆ University First-class Scholarship (2006)
- ◆ Outstanding Student-Cadre of University (2006)
- ◆ Excellent Member of Summer Service Team (2006)